

DESIGN AND DEVELOPMENT OF A STORM
RESEARCH UAS

By

ALYSSA SHEARON AVERY

Bachelor of Science in Mechanical and Aerospace

Engineering

Oklahoma State University

Stillwater, OK

2013

Submitted to the Faculty of the
Graduate College of the
Oklahoma State University
in partial fulfillment of
the requirements for
the Degree of
MASTER OF SCIENCE
May, 2015

DESIGN AND DEVELOPMENT OF A STORM
RESEARCH UAS

Thesis Approved:

Dr. Jamey Jacob

Thesis Adviser

Dr. Andrew Arena

Dr. James Kidd

.

ACKNOWLEDGEMENTS

I would to acknowledge helpful discussions with the following experts in the field: Dr. Steve Koch, Director of the NOAA National Severe Storms Laboratory; Steven Piltz, Meteorologist in Charge of the Tulsa Weather Forecast Office; Gary England, Meteorologist-in-Residence at the University of Oklahoma; Prof. Brian Argrow of the University of Colorado at Boulder; Dr. Phil Chilson of the University of Oklahoma; and Emily Sutton, Meteorologist at KFOR. I would like also to thank Dr. Jamey Jacob for integral direction and assistance throughout the project. For assisting in the build of the aircraft I would like to thank Calvin Brown, Jake Hathaway, Shea Fehrenbach, Zach Barbeau, and Nathan Avery.

I would also like to acknowledge the generous support of Ray and Linda Booker.

Name: Alyssa Shearon Avery

Date of Degree: MAY 2015

Title of Study: DESIGN AND DEVELOPMENT OF A STORM RESEARCH UAS

Major Field: MECHANICAL AND AEROSPACE ENGINEERING

ABSTRACT:

A small unmanned aircraft system (SUAS) was designed and developed to be utilized for meteorological data collection, specifically information useful for severe storm and tornado prediction. The system will operate prior to and during severe weather in order to minimize current knowledge gaps with respect to severe storms. This aircraft was developed to maximize the useful data collection while retaining the operational simplicity required of a tool used in an unpredictable environment. The aircraft design is capable of collecting in-situ atmospheric and IR thermodynamic data continuously in flight and deploying sensor packages, dropsondes, at vital locations. The airframe was built, has undergone initial testing, and will be integrated into an operational system in future work.

TABLE OF CONTENTS

Chapter	Page
LIST OF TABLES	vii
LIST OF FIGURES	ix
Acknowledgements.....	Error! Bookmark not defined.
INTRODUCTION	1
1.0 Motivation.....	1
1.1 Background.....	2
1.3 Goals and Objectives	3
1.4 Thesis Outline	4
LITERATURE REVIEW	6
2.1 Weather Sensor Systems.....	6
2.2 Weather Platforms	7
METHODOLOGY	13
3.1 Mission Development	13
3.2 Payload Design	20
3.3 Sizing and Configuration	25
DETAILED DESIGN	29
4.1 Aerodynamics	29
4.1.1 Sizing	29
4.1.2 Stability	37
4.2 Propulsion System	42
4.2.1 Reciprocating Engines	45
4.2.2 Electric Motors.....	48
4.3 Structure.....	51
4.3.1 Loads.....	51
4.3.2 Materials	53

4.3.3 Analysis.....	54
AIRFRAME BUILD.....	61
5.1 Manufacturing Process, MARIA I Build	61
5.2 MARIA II Build.....	65
TESTING AND RESULTS.....	70
6.1 X-Plane Simulation.....	70
6.2 Ground Tests.....	74
6.2.1 Taxi Testing	74
6.2.2 Motor Testing.....	76
6.3 Structural Testing.....	78
CONCLUSION.....	82
REFERENCES	84
APPENDICES	86
Airfoil Data	86
Stability Analysis	88
Structural Analysis.....	96
Drag Analysis.....	100
Solidworks FEA.....	101
X-Plane Model Characteristics	103

LIST OF TABLES

Table	Page
Table 1: Reference UAS and parameter sample	12
Table 2: Requirements for a storm research UAS	18
Table 3: Initial performance goals	19
Table 4: Mission plans for supercell research ²³	20
Table 5: Sensor Details	23
Table 6: Weight estimation method	26
Table 7: Configurations	27
Table 8: Final Sizing.....	34
Table 9: Parameters for Static Stability	38
Table 10: Summary of the predicted parasite drag from the aircraft	44
Table 11 Performance Predictions, Operational System.....	47
Table 12: Resultant gust loads	53
Table 13: Cost of materials and sample of advantages ²⁸	54
Table 14: Shear flow inboard wing.....	56
Table 15: Fuselage stress analysis by idealization.....	58
Table 16: Structure weight breakdown	64
Table 17: Gust response evaluation with X-Plane	73
Table 18: Load cell results.....	78
Table 19: Static Stability.....	88
Table 20: Tail and Elevator Sizing	88
Table 21: Elevator Hinge Calculations	89
Table 22: Vertical tail and rudder sizing.....	89
Table 23: Dihedral calculations	90
Table 24: Aileron Sizing.....	90
Table 25: Moment resultant of propulsion system.....	91
Table 26: Moment resultant of fuselage	91
Table 27: Aerodynamic Characteristics and Stability Derivatives	92
Table 28: Benchmarked Stability Characteristics	95
Table 29: Load Estimations	96
Table 30: Gust load calculations	96
Table 31: Aerodynamic surface moments	96
Table 32: Wing structure idealization.....	97
Table 33: Structure material characteristics.....	97
Table 34: Wing structure torsion results	97
Table 35: Spar bending calculations	98
Table 36: Fuselage torsion and bending calculations	99

Table 37: Drag Build-Up	100
Table 38: Inboard wing Solidworks FEA settings	101
Table 39: Tabulated resultant forces for FEA analysis, Inboard wing.....	102
Table 40: Fuselage Solidworks FEA settings	102
Table 41: Tabulated resultant forces for FEA analysis, fuselage.....	103

LIST OF FIGURES

Figure	Page
Figure 1: Tornado prediction statistics ²	2
Figure 2: Supercell form and nomenclature.....	3
Figure 3: Example mission concept of operation.....	4
Figure 4: Oklahoma Mesonet station locations and county lines ⁵	6
Figure 5: Tempest UA from University of Colorado at Boulder ¹¹	8
Figure 6: NexSTAR airframe used my CoCoNUE ¹²	8
Figure 7: SUMO UAS using the FunJet airframe my Multiplex ¹⁴	9
Figure 8: M2AV from Technishe Uniersitat Braunschweig ¹⁵	10
Figure 9: Silver Fox UAS ¹⁶	10
Figure 10: Mantra UAS ¹⁶	11
Figure 11: Data from smartsonde sounding shows increasing instability in the atmosphere ²¹	14
Figure 12: Dropsonde Deployment.....	15
Figure 13: Possible mission path for severe weather research, background figure4	16
Figure 14: Flight Profile.....	21
Figure 15: Tamarisk IR camera ²³	21
Figure 16: IR camera mounted in fuselage under IR transparent dome.....	22
Figure 17: TAMDAR-U Sensor ²⁴	22
Figure 18: Early iteration of dropsonde sensor setup	24
Figure 19: Dropsonde dispenser and fuselage cutaway	25
Figure 20: Reference UAS: Payload Weight vs. GTOW.....	25
Figure 21: Reference UAS Wing Loading vs. GTOW	28
Figure 22: Airfoil lift coefficient vs. angle of attack, XFOIL.....	30
Figure 23; Airfoil drag polar, Cd vs. Cl.....	30
Figure 24: Airfoil endurance parameter, $Cl^{3/2}/Cd$	31
Figure 25: Blended airfoil chosen for MARIA	32
Figure 26: Lift Curve, Blended airfoil "new4" Cl vs Alpha	32
Figure 27: Drag polar, Blended airfoil "new4" CL vs. CD.....	33
Figure 28: Moment Curve, Blended airfoil "new4" Cm vs. Alpha.....	33
Figure 29: One altered airfoil for analysis, a 25% percent area 20 degree deflection flap	35
Figure 30: Wing modeled in XFLR5 with inboard flaps	35
Figure 31: Flap predictions for wing using XFLR5 in inviscid setting.	36
Figure 32: Stall speed with 25 % 25 degree flap airfoil alteration, a range of Reynolds numbers.....	37
Figure 33: Aircraft's moment coefficient vs. angle of attack at a range of elevator input.	39
Figure 34: Center of gravity travel plot, Configuration 1	39
Figure 35: Fuel and dropsonde location, Configuration 1	40
Figure 36: CG travel plot, Configuration 2.....	41
Figure 37. Aircraft layout, Configuration 2.	41

Figure 38: Aircraft layout, electric propulsion,.....	42
Figure 39: Flight envelope for both gas and electric propulsion options.....	43
Figure 40: Power Required GAS AT SL	44
Figure 41: DLE-20 ²⁶	45
Figure 42: Payload versus endurance, 1000ft.	47
Figure 43: DLE-20 Engine as will be installed on the wing	48
Figure 44: Rimfire electric motor ²⁷	Error! Bookmark not defined.
Figure 45 Endurance with respect to horsepower	49
Figure 46: Endurance with respect to velocity.....	49
Figure 47: Electric Motor Cowling.....	50
Figure 48: Areas for special structural attention	51
Figure 49: Flight envelope and V-n diagram	52
Figure 50: Internal structure.....	55
Figure 51: Shear flow idealization format, three cell section	55
Figure 52: Fuselage cross-section idealization format.....	57
Figure 53: Fuselage stress analysis starboard-side load.....	59
Figure 54: Inboard Wing, loading case and deformation/strain plot	60
Figure 55: Inboard wing section plug, top part.....	61
Figure 56: Fuselage plugs	62
Figure 57: Fuselage mold and an outboard wing section mold.	62
Figure 58: Inboard wing skin.....	63
Figure 59: Assembled MARIA I airframe	64
Figure 60: Landing gear.....	65
Figure 61: MARIA I	65
Figure 62: Outboard to inboard joint connection; MARIA II left, MARIA I right	66
Figure 63: C-channel mold, for inboard spar.....	67
Figure 64: C-channel.....	67
Figure 65: Internal Structure in the inboard wing section.	68
Figure 66: Outboard ribs with cutouts for carbon tube.	69
Figure 67: Inboard wing MARIA II.....	69
Figure 68: X-Plane model of MARIA aircraft.....	70
Figure 69: Aircraft phugoid response after perturbation.....	71
Figure 70: Short period response of MARIA aircraft	72
Figure 71: Nose gear steering mechanism	74
Figure 72: MARIA I while taxiing	75
Figure 73: Landing gear installation dimensions	76
Figure 74: Sensor force accuracy check	77
Figure 75: MARIA I set up for static thrust tests.....	77
Figure 76: Testing setup for inboard wing.....	78
Figure 77: Inboard wing setup for loading.....	79
Figure 78: Inboard wing loaded with 112lb of weight.....	80
Figure 79: Inboard wing loaded with 200lb of weight.....	80
Figure 1: Torsion calculation subroutine, wing	98
Figure 2: Inboard wing model for Solidworks FEA	101

Figure 3: Fuselage model for Solidworks FEA	102
Figure 4: XPLANE Engine Specs.....	103
Figure 5: XPLANE Engine Specs.....	104
Figure 6: XPLANE Engine power transmission.....	104
Figure 7: XPLANE Engine SFC information.....	105
Figure 8: XPLANE propeller geometry.....	105
Figure 9: XPLANE wing specifications	106
Figure 10: XPLANE outboard wing specifications	106
Figure 11: XPLANE horizontal tail specifications	107
Figure 12: XPLANE vertical tail specifications	107
Figure 13: XPLANE wing flex parameter	108
Figure 14: XPLANE fuselage details	108
Figure 15: Engine nacelle characteristics.....	109
Figure 16: XPLANE control geometry specifications	110
Figure 17: XPLANE weight and balance information.....	111
Figure 18: XPLANE fuel weight and balance	111
Figure 19: XPLANE propeller airfoils.....	111
Figure 20: XPLANE wing and tail airfoils	112
Figure 21: XPLANE Airfoil Maker, airfoil design.....	113
Figure 22: XPLANE Airfoil Maker, airfoil rough shape.....	113

CHAPTER I

INTRODUCTION

1.0 Motivation

The need for increased severe storm warning times is evident every year when lives and property are lost due to tornados. According to the U.S. National Hazard Statistics, 55 people were killed by tornados in 2013.¹ The rate of false alarms for tornado warnings is between 70 to 80 percent, while Doppler radar systems have significantly improved tornado and severe storm knowledge.² However, the measurable characteristics that create tornados within severe storms are largely undetermined. The probability of detection has reached a plateau in the last ten years after its initial improvement with the integration of Doppler radar. Similarly, warning lead time has leveled off at a still short 12-14 minutes. The trends discussed for tornado predictions are shown in Figure 1 and includes lead times, probability of detection (PoD) and false alarm rate (FAR.)

Wide-spread in situ data is required for significant progress in tornado prediction.³ Atmospheric behavior profiles in the form of in-situ thermodynamic data, thermal images, and flow characteristics at the surface of the storm, data prior to circulation and during tornado genesis could significantly improve weather models

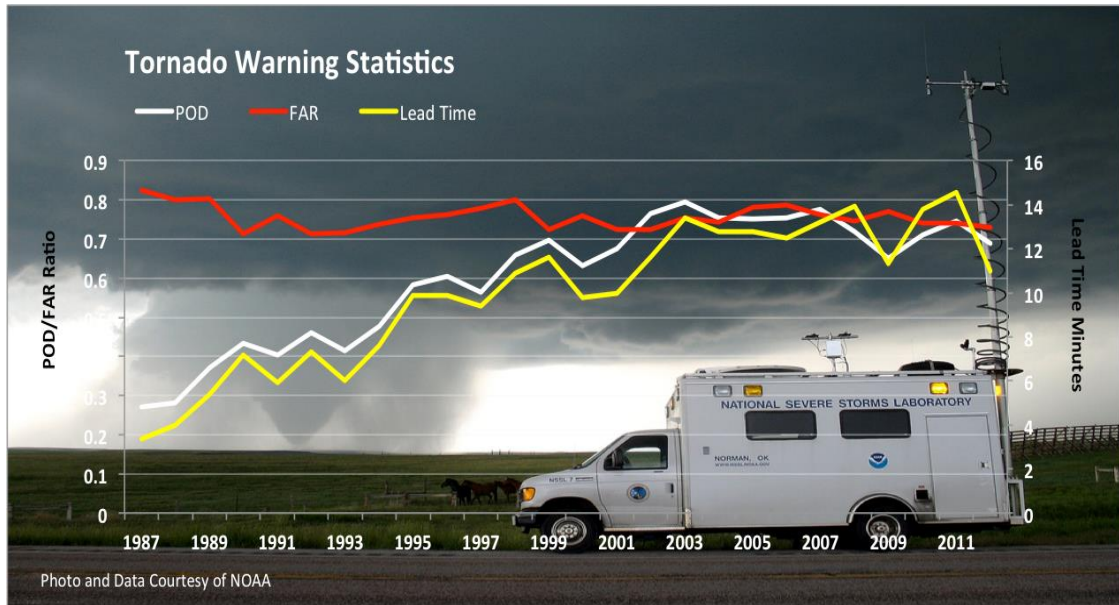


Figure 1: Tornado prediction statistics; the increase in PoD and lead time is due to Doppler radar.²

1.1 Background

The current technologies currently in place are incapable of gathering this information. Mesonet towers range from 10 to 20 meters tall and are stationary. Unmanned weather balloons are too influenced by the significant winds, thus are unable to be controlled in severe weather. Manned aircraft have also been used for storm tracking and qualitative data, but conditions are too dangerous for flight within severe storms. Unmanned Aerial Systems (UAS) provide a solution for gathering information in an environment unsafe for piloted aircraft. When compared with other in-situ measurement systems UAS provide a more flexible, safer solution for real-time data acquisition. Small unmanned aerial systems or sUAS are more operationally flexible when compared with manned aircraft or larger unmanned systems. A small system in the hands of storm chasers or a small research team may be utilized on the day of the storm with a relatively small amount of preparation.

1.3 Goals and Objectives

This project aims to design and develop an aircraft with maximum data acquisition capability which is able to be operated in a storm chasing scenario. Figure 2 displays a diagram of a supercell thunderstorm; all tornados come from supercells so these are especially important for mission planning.

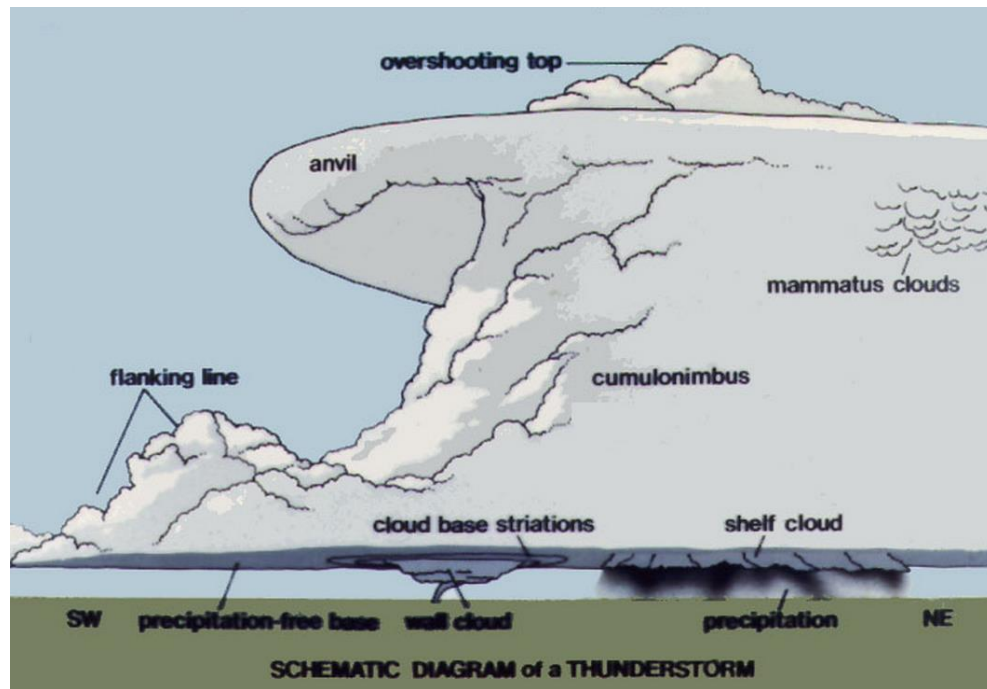


Figure 2: Supercell form and nomenclature.³

There are many potential missions for atmospheric sampling in severe weather. Figure 3 gives an example of a type of mission to be flown by the aircraft. The aircraft would be launched from a safe but convenient location, fly at the altitude of interest, and drop sensor packages in areas likely to be pulled into circulation. It will fly near the severe storm collecting information on board and with dropsonde sensor packages deployed during flight.

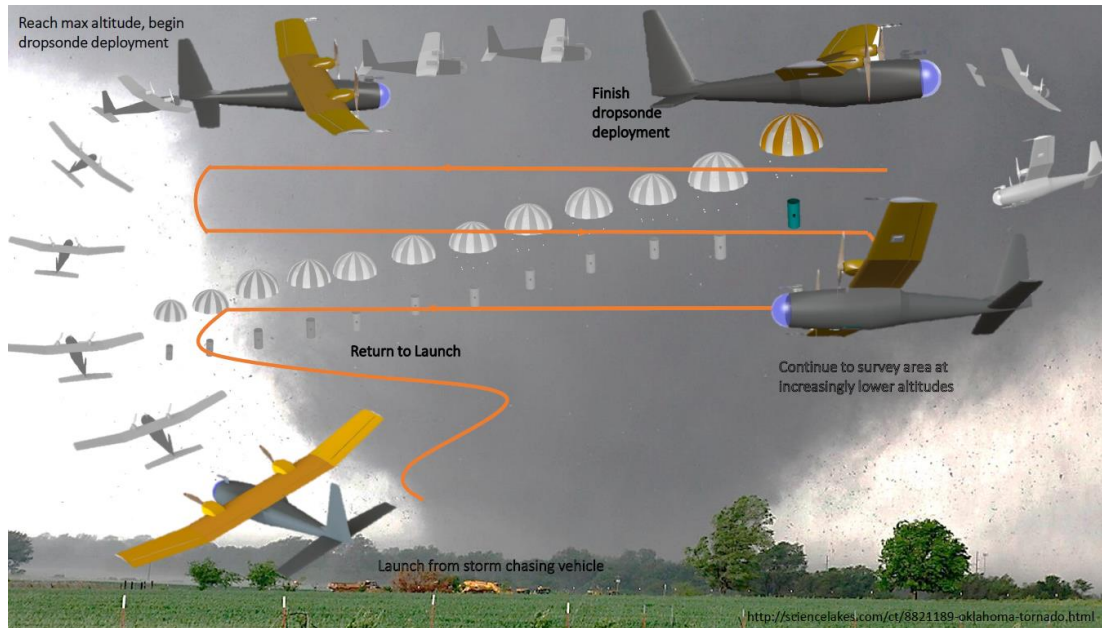


Figure 3: Example mission concept of operation.

The design constraints are developed specifically for storm sampling missions. The design allows the aircraft to be deployed by a small team in the field and to operate throughout the development of severe weather within a certain distance of a storm. It also allows the onboard sensors to operate successfully and deploy a number of small sensor packages. The aircraft is built and has undergone initial testing to its design conditions. Structural tests verify the survivability in the projected mission. Flight tests are undertaken to demonstrate airworthiness in some conditions, and computer models are used to test the design at the corners of its flight envelope. The testing should prove that the aircraft is robust structurally, stable in high gusts, and capable of reaching performance goals.

1.4 Thesis Outline

Past and current weather research systems are discussed, with greater detail on meteorological profiling UAS. The operational expectations and goals for a relevant severe storm are outlined and reviewed. The payload design for optimizing data acquisition and the requirements therein are considered and finalized. The initial aircraft design is covered and

discussed including benchmarking, sizing, performance goals, and initial configuration. The detailed design methods and decisions are covered. This includes the aerodynamic design with, XFOIL and XFLR5 airfoil analysis, sizing of aerodynamic surfaces, and hand calculated and xflr5 stability analysis. The propulsion system requirements and selection is presented. Structural design and analysis is examined, including loads estimation, material selection, excel analysis, Solidworks qualitative FEA, and manufacturing methods. The aircraft design verification and testing are presented. The paper finishes with final thoughts and plans for future work.

CHAPTER II

LITERATURE REVIEW

2.1 Weather Sensor Systems

A variety of systems are used to monitor weather and sample the atmosphere; these measurements build prediction models and atmospheric knowledge. Balloons both tethered and untethered, stationary towers, and radar are utilized for weather sensing, as well as aircraft. The Oklahoma Mesonet consists of 108 stations distributed across the state⁵, as shown in Figure 4. These are 10 meter towers thoroughly equipped with sensors. The standard sensor suite in each station includes equipment to collect wind, air temperature, humidity, solar radiation, pressure, and rain level data.



Figure 4: Oklahoma Mesonet station locations and county lines.⁵

Radiosondes carried by untethered balloons are another important and widely utilized in-situ weather sensing tool. Generally, these travel up to 30 km and measure pressure, humidity, temperature, and wind vectors.⁶ These soundings provide atmospheric profiling information in addition to daily weather data. Tethered balloon soundings are of a similar mission but with an extended operational time, some up to 20 hours.⁷ Remote sensing has become an integral part of weather prediction methods, especially radar and Doppler radar. As discussed earlier, remote sensing has not provided the full spectrum of data required to improve weather models. In order to provide the in-situ information needed, reliable weather aircraft platforms are required.

2.2 Weather Platforms

Manned aircraft have been used in many programs for quantitative and qualitative weather research. The Tropical Cyclone Structure program in 2008 used NP-3 and WC-130J aircraft in the Western Pacific.⁸ The P-3 was fitted to use a Doppler wind LIDAR and the ELDORA radar; it collected data on the outer part of a typhoon. The WC-130s are able to penetrate the eyewall and studied the inner typhoon core; its instruments collected wind speed and direction, humidity, and temperature. Both aircraft used dropsonde systems. The WC-130 dropsonde deployments were able to generate vertical atmospheric profiles, transmitted back to the aircraft over high frequency radio. The program validated typhoon prediction techniques. The A-10 is a structurally imposing aircraft that will be used for severe storm research.⁹ It was built to sustain projectile hits and to carry substantial weapons. For weather research, the payload will be transferred to meteorological sensors and the structure will be further fortified to withstand flight loads in severe storms, in spite of its already robust structural design.

More recently, UAS have been used for weather research in a few different capacities. The University of Colorado at Boulder has characterized the guidance for a storm penetrating UAS. They used grids of storm data and created guidance profiles and mission profiles to create safe routes for significant data acquisition.¹⁰ The group also has used unmanned aircraft for

collecting meteorological data in multiple programs, which includes their Tempest Tornado Chaser aircraft. The Tempest UA is a small, highly portable, low cost aircraft flown semi-autonomously with the Piccolo SL autopilot¹¹ and is shown in Figure 5.



Figure 5: Tempest UA from University of Colorado at Boulder.¹¹

The Collaborative Colorado-Nebraska Unmanned Aircraft System Experiment (CoCoNUE) used an off-the-shelf airframe to collect atmospheric data.¹² The NexSTAR airframe from Hobbico is a small electric airplane made of balsa, plywood and Monokote. It is capable of rapid deployment with an aluminum rail, but relatively low endurance. The plane, shown in Figure 6, was semi-autonomous with overall control through a virtual cockpit.



Figure 6: NexSTAR airframe used my CoCoNUE.¹²

Both the Tempest system and the CoCoNUE project's designs incorporated a mobile ground station to control, monitor, and collect data from the aircraft. These mobile units allowed for line of sight regulations to be followed while allowing the UAS to gather the data required.

The University of Bergen in Norway used an UAS for atmospheric boundary research.¹⁴ This project aimed to profile the Atmospheric Boundary Layer with basic meteorological sensors and autonomous flight missions. An off-the-shelf hobby airframe, the FunJet, and a Paparazzi autopilot were chosen for the project; the airframe is shown in Figure 7.



Figure 7: SUMO UAS using the FunJet airframe my Multiplex.¹⁴

In Braunschweig, Germany a team developed UAS was to especially sample the troposphere and was the first UAS to be operated in Antarctica.¹⁵ The aircraft, Meteorological Mini Aerial Vehicles (M²AV), was self-constructed by the university and is hand or bungee launched (Figure 8). It operated autonomously with way-points set prior to take-off.



Figure 8: M2AV from Technische Universität Braunschweig.¹⁵

The Silver Fox, developed by NOAA and the Office of Naval Research and manufactured by ARC, is a UAS capable of being launched at sea.¹⁶ It can be used for atmospheric and small vessel surveillance. It carries a CCD camera and an infrared sensor. The aircraft is shown in Figure 9.



Figure 9: Silver Fox UAS.¹⁶



Figure 10: Mantra UAS.¹⁶

They developed the Mantra UAS with the same mission intention; it is shown in Figure 10. With its larger payload capacity, it carries its camera system in a 360 degree gimbaled turret. These two UAS were low altitude low endurance systems suited for surveillance and are still being developed for greater utilization.

The University of Oklahoma developed a micro-air vehicle, dubbed Smartsonde, for in-situ support of radar research.¹³ Like the CoCoNUE program, a NexSTAR FunJet airframe was chosen though a paparazzi autopilot was used for in the Smartsonde.

These systems demonstrated capability of measuring important meteorological parameters for severe storms. The design goal for this project aims to develop a system to provide detailed atmospheric profiles over long periods of time leading up to severe storm formation. This is enabled though a vehicle design with larger payload capability and endurance than the above systems. Table 1 compares the UAS discussed above.

Table 1: Reference UAS and parameter sample.

	GTOW [lb]	Span [in]	Endurance [hrs]	Payload [lb]	Vmax
Silver Fox	27	94 in	8-10	5	110 kts
Manta	52		6 +	15	110 kts
Tempest	15	125	0.75	Vaisala RS-92	68
NexSTAR	11	67	0.75	1.1	
M²AV	13	79	0.83	3.3	
SUMO	1.3	32	0.5		68

It has been demonstrated that UAVs are capable of atmospheric profiling, providing temperature, humidity and wind measurements important for characterizing the vertical structure of the lower troposphere. For instance, the behavior with height of the virtual potential temperature can be used to identify the regions of thermal stratification and the degree of atmospheric stability.¹⁷ The vertical gradient of the wind vector leads to wind shear, which can produce turbulence and thus turbulent fluxes in the atmospheric boundary layer.¹⁸ There is currently a gap between tower-based measurements and airborne (manned) systems and this gap occurs at critical levels in the boundary layer. Remote sensing systems, such as radar, sodar, and LiDAR fill part of this gap, but still do not provide the detailed information required for modeling and a complete understanding of the formation of complex weather systems such as tornados.¹⁹

CHAPTER III

METHODOLOGY

3.1 Mission Development

The design constraints for the aircraft were developed from discussions with meteorologists, storm data, and realistic airframe capabilities. In order that MARIA be useful to the meteorological community, the system needs to provide information not provided by Doppler radar, the Mesonet or other systems. The aircraft should provide continuous in-situ thermodynamic data at the maximum interesting number of data points. The system should also be easily transported, operated with little preparation, and by a small crew.

The system will attempt to create a profile of the boundary layer as it progresses into a severe storm or tornado. The lifting condensation level ranges from 800ft to 2000ft above ground level. Doppler radar can suggest possible severe weather formation 2-3 days before it occurs.²⁰ The system should begin sampling the air before it begins to display significant instability. This can occur hours before tornadogenesis.

Figure 11 shows the unstable heating that would be visible in in-situ data prior to severe weather. This is collected from the University of Oklahoma's Smartsonde MAV taking vertical profile measurements.

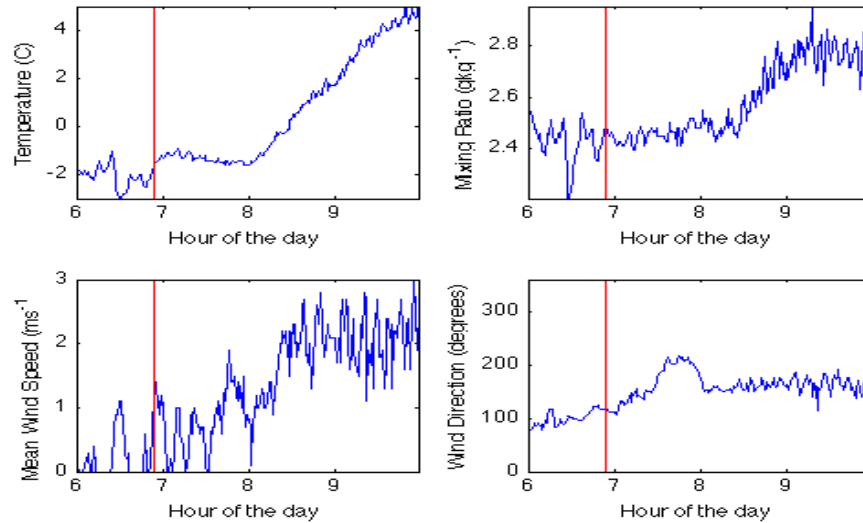


Figure 11: Data from smartsonde sounding shows increasing instability in the atmosphere.²¹

Thus, the aircraft will fly from six to eight hours from 500 ft. to 5000 ft. AGL to gather a well populated meteorological grid from the start of storm formation. In order to provide the necessary atmospheric data, MARIA will carry an onboard sensor suite and a number of dropsondes, small sensor packages. **Error! Reference source not found.** displays an example of he type of mission MARIA is expected to fly.

The main tool for atmospheric data acquisition will be the TAMDAR(Troposphere Airborne Meteorological Data Reporting) system from Panasonic. This system collects an expansive array of atmospheric information. The TAMDAR sensor requires clean airflow, therefore cannot be placed aft of the propellers. Thermal imaging and visible cameras will be used to gather qualitative and quantitative data and should be capable of two axis rotation within

the protection of the aircraft. Deployable sensor packages, i.e., mini-MES, will be deployed from the aircraft to increase the data population, as shown in Figure 12.

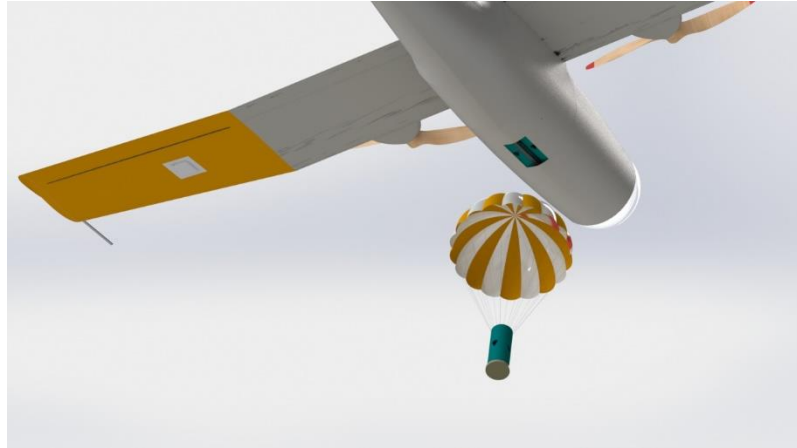


Figure 12: Dropsonde deployment.

The dropsondes will also provide information in regions too unstable and dangerous for the aircraft. The meteorological sampling in these locations may prove extremely valuable. The altitudes, ranges and dropsonde deployment locations will be determined by the specific storm system being investigated. A possible mission for data collection is shown in Figure 13.

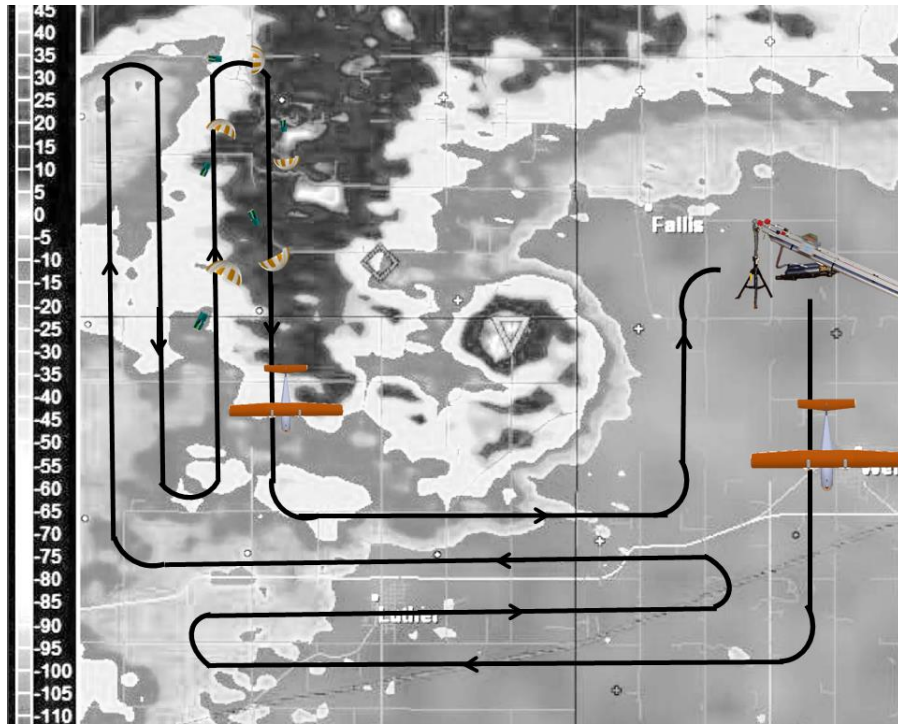


Figure 13: Possible mission path for severe weather research, background figure.²²

A small system is best used in the hands of a storm chaser or research team for deployment close to storm development. The operational constraints for this mission are designed for a storm chasing team in the field. The system should fit in a van or truck and be able to deploy without a runway, allowing MARIA to be used at a location within optimal proximity to a storm system. The aircraft will be deployed with a launcher to eliminate runway requirements and provide consistent takeoffs. The aircraft will belly land after mission completion in a field or road. Table 2 details the requirements needed for an unmanned aircraft to complete survivable severe weather research.

The surface winds in severe weather are usually 40-50 mph²⁰ and yearly maximum gusts in the area rarely exceed 90 mph. The extreme winds that tornados can produce would not be a feasible design goal, nor be representative of a realistic operational mission. For the MARIA aircraft, a 300 mph gust, such as seen in the El Reno 2013 tornado, would produce a 50g load. An 80 mph design consideration allows the aircraft to survey within proximity of a severe storm

without requiring an unreasonable structural expectation. The requirements in this list are only those determined to be achievable within the scope of the project. Other less likely dangers possible in severe weather are not incorporated into the design at this stage, such as electrical charge build up and carburetor icing.

Table 2: Requirements for a storm research UAS

	Requirements	System
1	Takeoff, land, fly between waypoints, and loiter at the target waypoint autonomously.	Avionics
2	Provide real-time forward-facing video data (VIS/IR) to the GCU.	Airframe, Sensors
3	Launch from an unimproved runway or a launcher.	Airframe, Launcher
4	UAV and the GCU shall be transported in a standard cargo van.	Airframe, Avionics
5	Provide real-time GPS position and magnetic heading data to the GCU for wind estimates.	Sensors
6	Airframe should allow clean airflow into TAMDAR or similar DAQ.	Airframe
7	Provide real-time storm data via TAMDAR.	Sensors
8	Provide implementation capability for additional sensors, such as hot-wire and multi-hole probes.	Airframe, Sensors
9	Loiter at the target waypoint with 6 hours Endurance.	Airframe
10	Cruise speed sufficient to track moving storm. (Ave. translational speed 30 mph)	Airframe
11	Demonstrate stable flight in 80 mph wind gusts (headwind, tailwind, and direct crosswinds).	Airframe
12	Gust limits of 80 mph with no significant structural damage.	Airframe
13	Carry multiple dropsondes.	Airframe, Sensors
14	Rain and hail resistant; ability to withstand impact from quarter sized hail and land safely.	Airframe
15	Belly land recovery on runway or improved road.	Airframe
16	Adaptable to standard autopilot and ground control systems.	Avionics

The New Mexico Institute of Mining and Technology has investigated electric charge accumulation resultant from aircraft flight through clouds. A sailplane, powered sailplane, and a twin turboprop were used for testing. They were outfitted with instrumentation to provide the electric fields in the clouds and the net charge on the aircraft. A noticeable charge was acquired in each case, most commonly by induction from water particles in clouds. In both powered airplanes, engine exhaust served to dissipate charge on the aircraft. The charge decay with the

engines on was significantly accelerated in comparison to the rate of charge decay with no exhaust. With MARIA, much of the skin is not capable of conducting electricity. The only conductive materials used is carbon fiber, only present in internal structure of the wing and some fuselage skin. Thus, the accumulation and decay characteristics are chiefly unknown.

Preliminary performance goals for the aircraft are listed below in Table 3. These were deemed necessary to have effective, survivable flights in storm conditions. The goal stall speed is low enough to allow successful deployment off of the launcher and the goal maximum speed is high enough to retain control in the design 80 mph wind consideration. As discussed in the introduction, it is important that the aircraft's endurance allow data to be collected prior to atmospheric instability. The grid being sampled will fall below radar altitude and will likely follow the lifted condensation level(LCL.) This is usually below 2,000ft AGL and can fall to about 800ft AGL. The service ceiling in the table indicates the maximum operational expectation; the aircraft's service ceiling will far exceed that. Table 4 describes the operational plans for research with MARIA.

Table 3: Initial performance goals.

Parameter	Objective	Threshold
Stall speed	32 knots	40 knots
Maximum Speed	100 knots	80 knots
Endurance	8 hours	6 hours
Service Ceiling	6,000 ft.	6,000 ft.
Survivable Gust	80 mph	70 mph

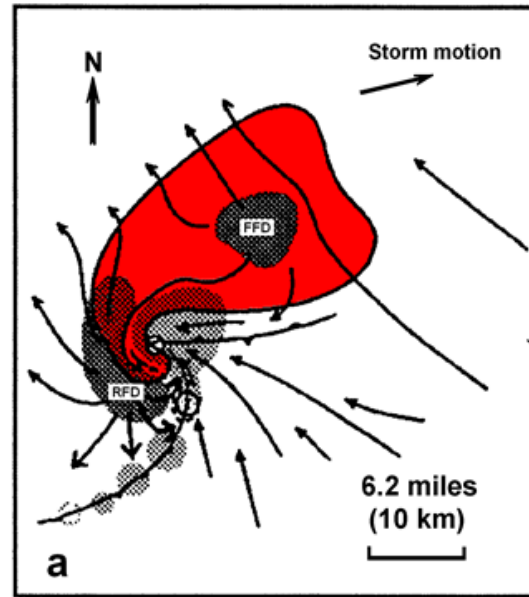
Table 4: Mission plans for supercell research.²³

Mission Scenarios

1. -Initiate flight hours prior to storm formation
-Survey stationary grid prescribed by radar prediction, specifically around LCL
- Land upon tornado formation of supercell dissipation
2. - Initiate flight hours prior to storm formation
- Survey mobile boundary layer
- Follow supercell or tornado outside downdraft sections
- Land upon tornado or supercell dissipation
3. -Initiate flight upon supercell formation
- Circle storm outside downdraft sections surveying at variable altitudes
- Continue to survey after storm ends
- Land when necessary

Range 500 miles:

Supercell average size and structure



Allows for approx. 6 laps around

3.2 Payload Design

In order to retain control in a dynamic environment, MARIA will fly with a stabilizing autopilot. The team will be testing the aircraft with various off the shelf autopilots to determine the one best suited to a changeable mission, under high gusts. The autopilots considered include several low cost options the APM, Blackswift, Stabilis, and Pixhawk. In addition to reliability, the autopilot should have an open architecture to allow the operators to allow to modify the autopilot algorithms to optimize performance in severe storm environments. The autopilot that will transmit GPS location as well as IMU data. The autopilot onboard will be capable of stabilizing and controlling the aircraft after its launch, through the meteorological reconnaissance up until the descent. Figure 14 outlines MARIA's intended flight profile.

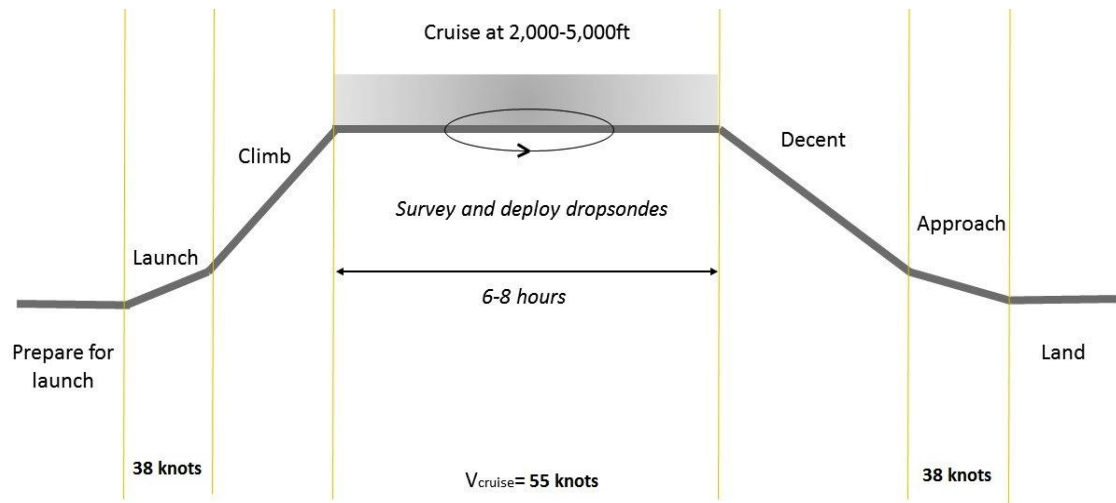


Figure 14: Generalized flight profile.

MARIA will be equipped with a variety of sensors to observe the storm. There will be an IR camera providing footage to the ground. The camera to be used is the Tamarisk long wave IR camera from DRS (Figure 15).



Figure 15: Tamarisk IR camera.

The IR camera serves as a thermal imaging camera in order to visualize temperature changes in the mesocyclone. Thermal imaging can also be used to monitor traffic and locate victims in debris in post-disaster use. The infrared camera will be contained inside the fuselage on a gimbal, as shown in Figure 16.

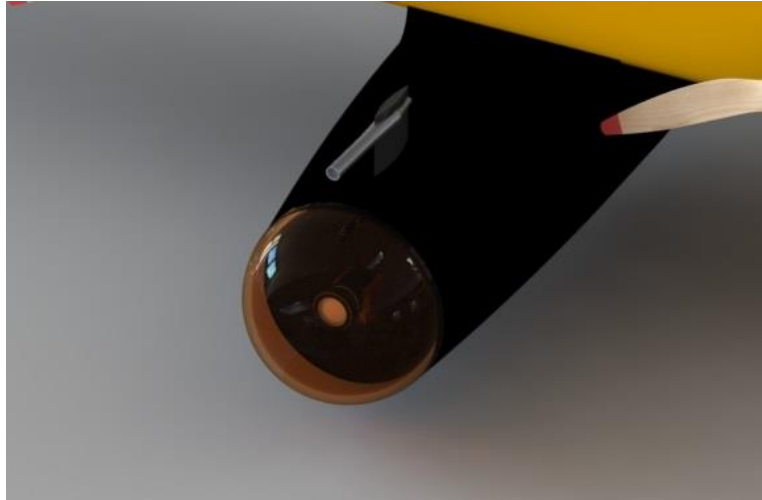


Figure 16: IR camera mounted in fuselage under IR transparent dome.

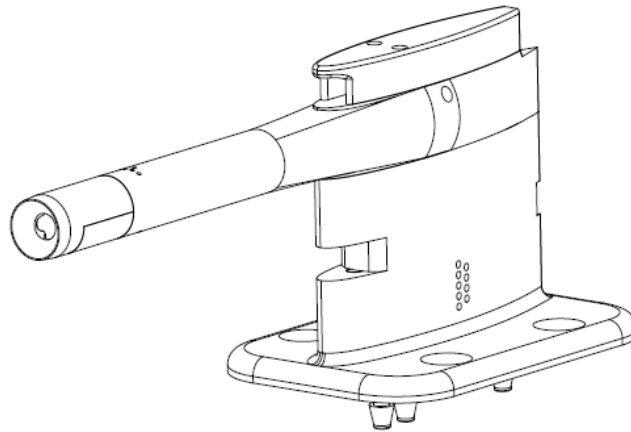


Figure 17. TAMDAR-Edge Sensor.

In addition to the qualitative data, there will be a number of quantitative meteorological sensors. The sensors are a part of the Panasonic TAMDAR system. Figure 17 shows a sketch of Panasonic's sensor modified from unmanned systems, a TAMDAR-Edge. TAMDAR (Troposphere Airborne Meteorological Data Reporting) is an atmospheric data collection and relay system. Recorded atmospheric data include temperature, pressure, winds aloft, relative humidity, icing and air turbulence. The system also has onboard GPS with both latitude/longitude and altitude coordinates. This system will be mounted to the forward fuselage

of MARIA so that the cleanest airflow is provided. Implementation of TAMDAR-U will allow MARIA to provide real time atmospheric and position data.

Additional outboard sensors will consist of a 5-hole probe, and hot wire sensors. The hot wire sensors will be mounted on the wing tips to measure wind velocity and turbulence. Table 5 contains the basic information concerning the sensors to be used onboard the aircraft.

Table 5: Sensor Details.

Sensor	Data Gathered	Est. Weight [oz.]	Est. Req.	Power
TAMDAR-Edge	Temperature, Pressure, Winds aloft, humidity, icing, turbulence	16		
5-hole probe	Air speed, heading, alpha, beta	10	9 V	
Hot wire sensor	Wind Speed, high resolution	< 6	5 V	
IR Camera	Thermal imaging	1.8	5 V	
Autopilot	Inertial measurements, Barometric pressure, Heading	1.4	6.6 V	
Dropsondes	Pressure, temperature, humidity, GPS	12	8 V	
Pitot probe	Air speed	1.5	3.3 V	
GPS	Location	1.1	5 V	

The dropsonde weather sensor packages will consist of pressure, temperature, humidity and GPS. The sensors are small inexpensive breakout boards that will send data through an Arduino board or similar microcontroller. Figure 18 shows the initial dropsonde development; the operational dropsonde will use a smaller microcontroller and a more compact setup.

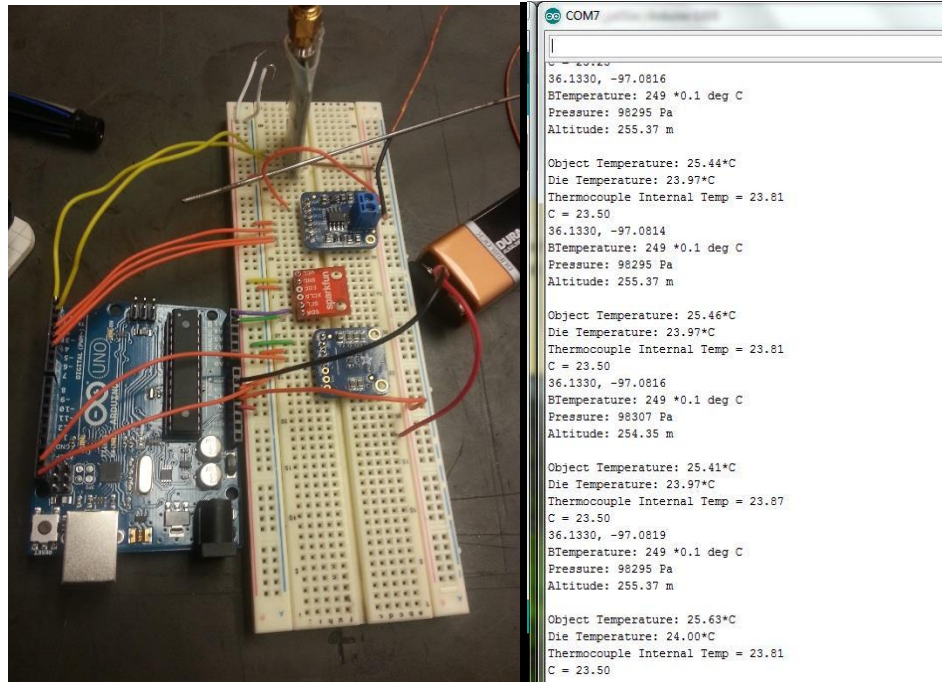


Figure 18: Early iteration of dropsonde sensor setup.

Dependent on ground station development in the future, the information will be either transmitted to the ground station, or relayed to MARIA, recorded onboard on the breakout board. The dropsondes are stored in a dispenser that will drop them one at a time. The cutaway shown in Figure 19 shows the system that will store and deploy the dropsondes. The dropsonde holder will be rotated by a servo, allowing the dropsondes to deploy from the aircraft on command. The sensor packages will be attached to small parachutes in order to allow drafts in severe weather to pull the dropsondes into areas too dangerous for the aircraft.

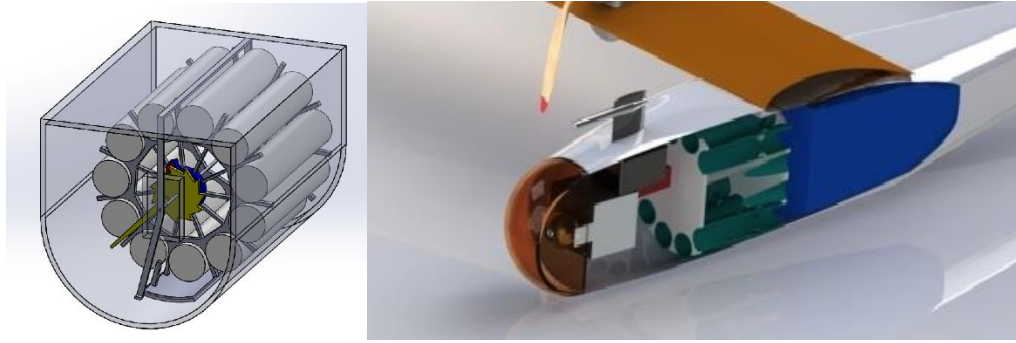


Figure 19: Dropsonde dispenser and fuselage cutaway.

3.3 Sizing and Configuration

Since the number of mission-similar UAS is scant, a wide range of small and mid-sized unmanned aircraft were documented for realistic reference, including those discussed earlier, Figure 20. The level of correlation for important parameters is low, but a realistic range of weights was gauged. From the sensor selection, the required payload weight was estimated to be 10lb not including fuel weight.

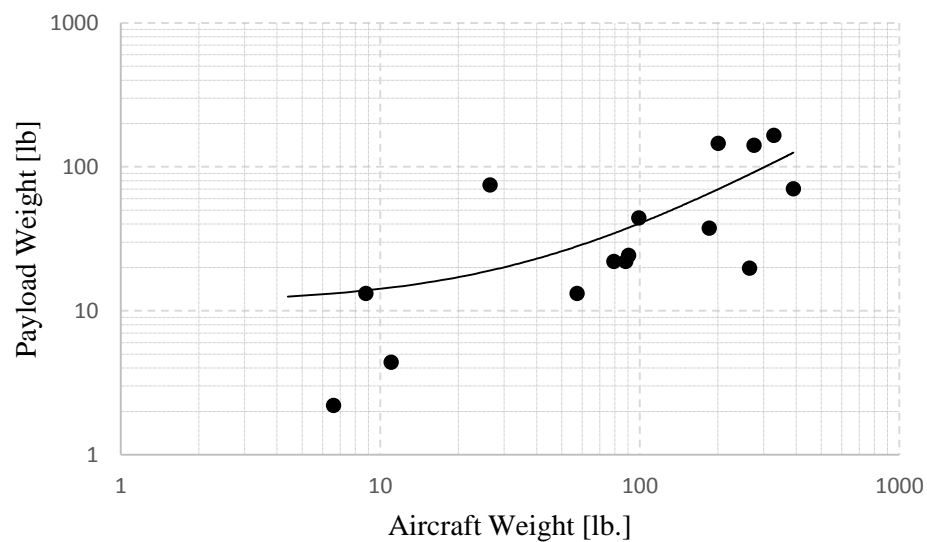


Figure 20: Reference UAS: Payload Weight vs. GTOW.

Based on these aircraft, a weight range of 20-80lb was fabricated. A weight estimate was also produced from sizing methods in Gundlach's textbook, Table 6.²⁴ The propulsion weight was

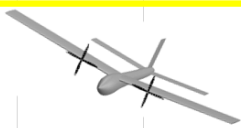
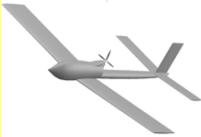
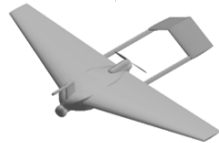

estimated with the decision to use a gas propulsion system; this choice will be discussed in section 4.2. The weight fraction for structural weight in the upper range because of the significant loads expected. The rough estimate from weight fractions was 40lb.

Table 6: Weight estimation method.

Payload	Weight [lb]			Propulsion		
TAMDAR	1.5			P/W _{TO}	0.12	[Sheet1]
RD94 Dropsonde	0.5 x 12			Max Power[hp]	9	[Benchmarking]
IR Gimbal	0.75			Endurance[hr]	8	
IR Camera	0.10625			P/W _{powerplant}	1	[UAS Des. Book]
Sensors	8.356			BSFC [lb/ hp-hr]	0.8	[UAS Des. Book]
Avionics	0.25			f _{install}	1.3	
	WeightFraction					
Fuel	0.0854		[UAS 3.27]			
AV					1000	3000
Propulsion	0.156		[UAS 3.6]	Density[slug/ft^3]	0.002308	0.002175
Structures	0.3		[Est.]	Visc. [slug/ft s]	3.727E-07	3.7E-07
Total Weight	18.8				16	
				Fuel Weight	18.56	
				Propulsion	5.37	
				Total Weight	37.5	

A major limiting factor with respect to configuration is the propulsion placement. The onboard equipment require the motor or motors to be aft of the sensors; the tractor configuration common to UAS is not suitable for the aircraft. Additionally, a tailless design is not feasible because of the high level of stability required; the design requirements aim for an aircraft stable in 80 mph gusts. Four main configurations were considered in depth. These are summarized in Table 7.

Table 7: Configurations.

*Basic Configurations only, specific planforms and cross-sections not considered									
									
	1		2		3		4		
	Complexity	Efficiency	Complexity	Efficiency	Complexity	Efficiency	Complexity	Efficiency	
Structures	0	1	0	0	0	-1	0	0	
Aerodynamic	0	1	0	-1	0	0	0	0	
Propulsion	-1	1	1	0	1	0	0	0	
Controls									
Launch and Recovery	0	0	1	0	1	0	-1	0	
Optics	0	0	0	0	0	0	0	0	
Dropping payload	0	0	-1	0	0	0	0	0	

The boxed aircraft configuration was chosen for the detailed design. A continuous fuselage was more structurally efficient than the split tail under the expected gust loads. The twin engine design will provide blown flaps and propulsive redundancy. Other considerations for this configuration include its high wing for increased roll stability and motor safety, and a conventional tail for maximum yaw authority in case of an engine-out scenario. Figure 21 shows the configuration chosen for the initial design. The TAMDAR sensor will be placed at the front of the aircraft with dropsondes in the belly of the aircraft. The camera will be placed in the nose of the aircraft and fuel will be in the fuselage close to the center of gravity.

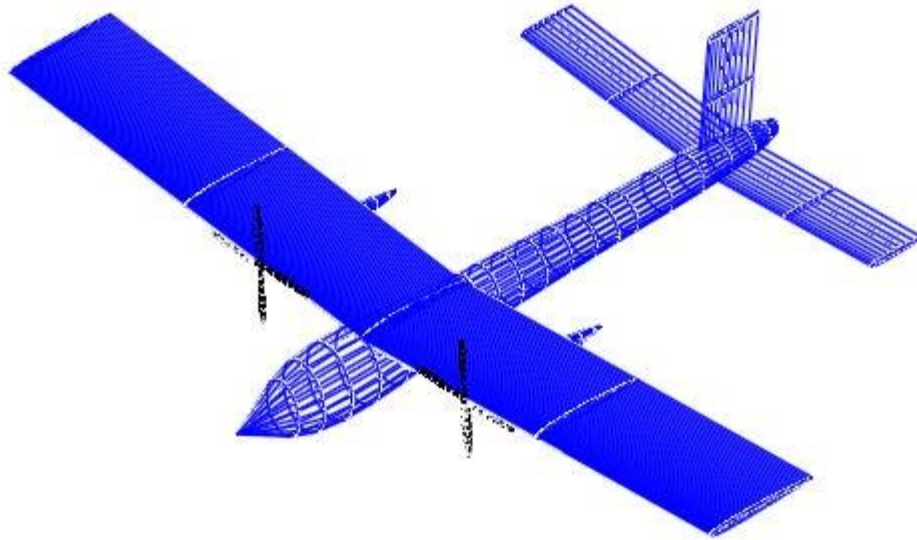


Figure 21: Initial concept sketch.

The wing loading for a high-gust aircraft should be low. MARIA however, must also meet strict stall speed and endurance requirements. The wing loadings for the respective reference aircraft are presented in Figure 22. As can be seen by the figure, this process was vaguely unhelpful. Thus, the iterative design process began with a large range.

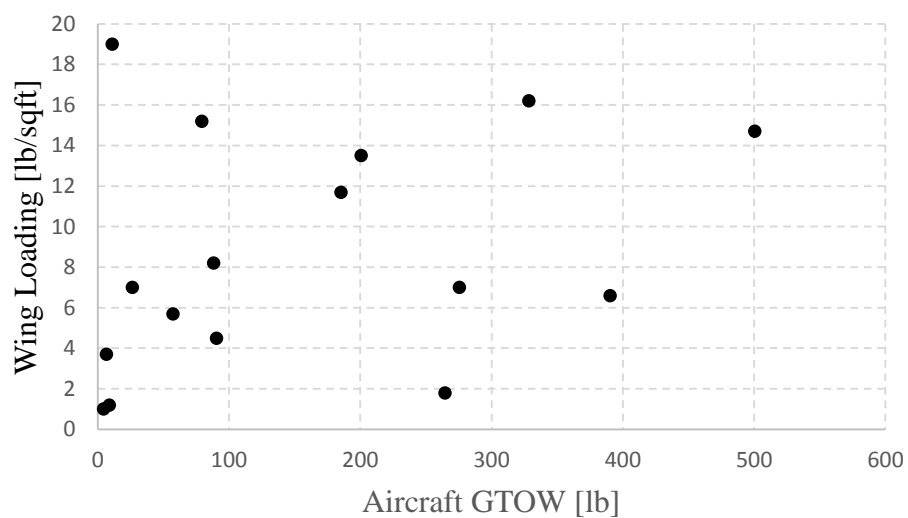


Figure 22: Reference UAS Wing Loading vs. GTOW.

CHAPTER IV

DETAILED DESIGN

4.1 Aerodynamics

4.1.1 Sizing

Since gust loading is a major structural concern, the wing loading is limited to be in the high to medium range. Small aircraft with mid to high wing loading, within the expected velocities, has the aircraft flying with low Reynolds numbers from 250,000-500,000 with an estimated cruise Re of 340,000. The performance goals seek an airfoil with a high maximum lift coefficient, high $C_L^{3/2}/C_D$, and a large thickness. In order to reach the stall speed threshold, the most ambitious of these parameters is the maximum lift coefficient.

A variety of airfoils were tested at a Reynolds number of 400,000, a sample of which as shown below. Figure 23, Figure 24, and Figure 25 show the lift slope, drag polar, and endurance parameter of the airfoils tested, respectively.

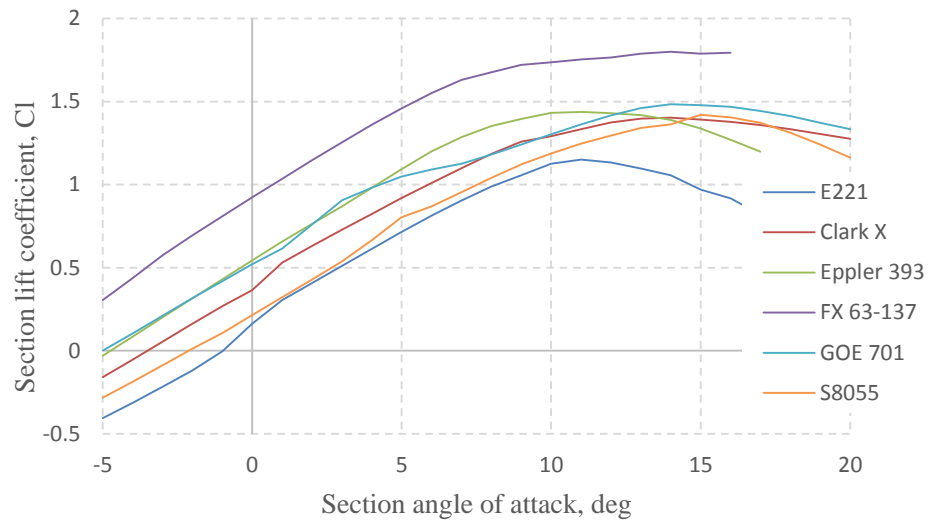


Figure 23: Airfoil lift coefficient vs. angle of attack, XFOIL.

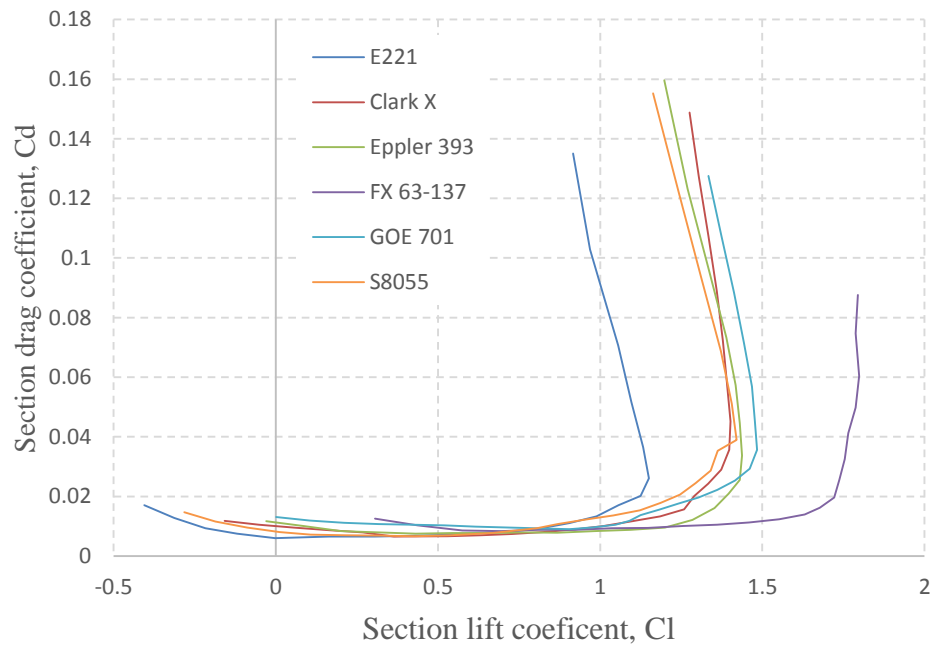


Figure 24; Airfoil drag polar, C_d vs. C_l .

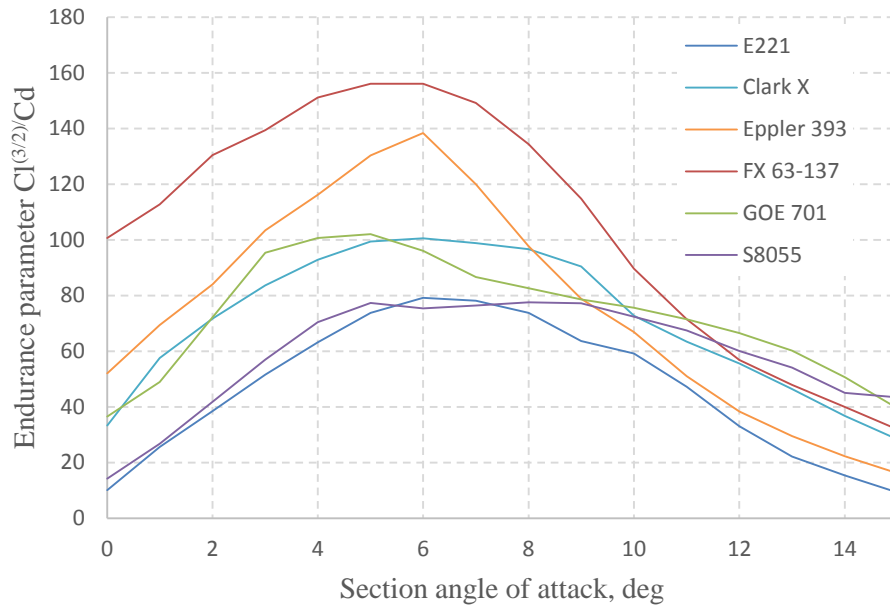


Figure 25: Airfoil endurance parameter, $Cl^{3/2}/Cd$.

Only airfoils with thicknesses of 11% or greater were considered because of structural constraints. For most parameters the FX 63-137 airfoil performed the best. However, the extreme camber causes the airfoil to have a thin trailing edge. The GOE 701 airfoil performed acceptably and has a more structurally feasible shape.

In addition to the number of common airfoils, ten different blended airfoils were tested. The airfoils selected are the FX 63-120 and GOE 701 to keep an acceptable thickness for structural considerations while providing good airfoil performance at lower Reynolds numbers. The blended airfoil that exceeded the performance of the other airfoil considered is shown in Figure 26.

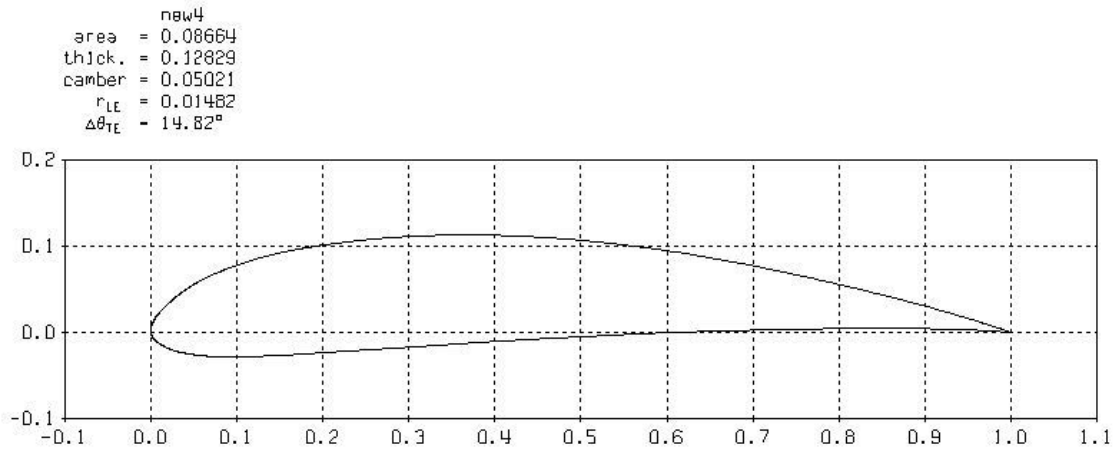


Figure 26: Blended airfoil chosen for MARIA.

Figure 27, Figure 28, and Figure 29 show the lift curve, drag polar, and airfoil moment, respectively, of the blended airfoil across the range of Reynolds numbers expected. The airfoil coordinates and performance results from XFOIL are included in the Appendix.

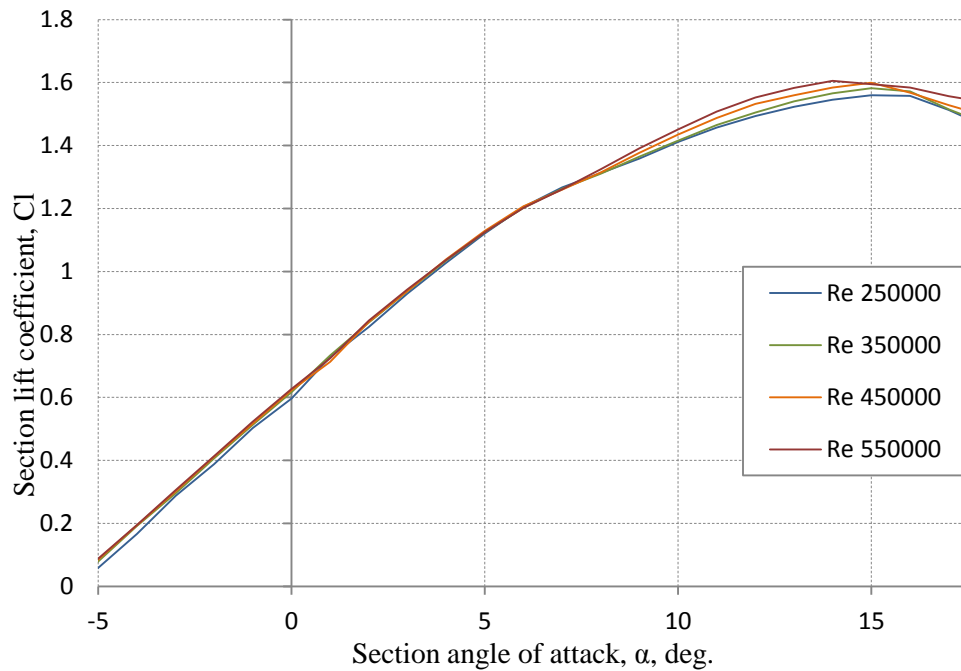


Figure 27: Lift Curve, Blended airfoil "new4" C_l vs Alpha.

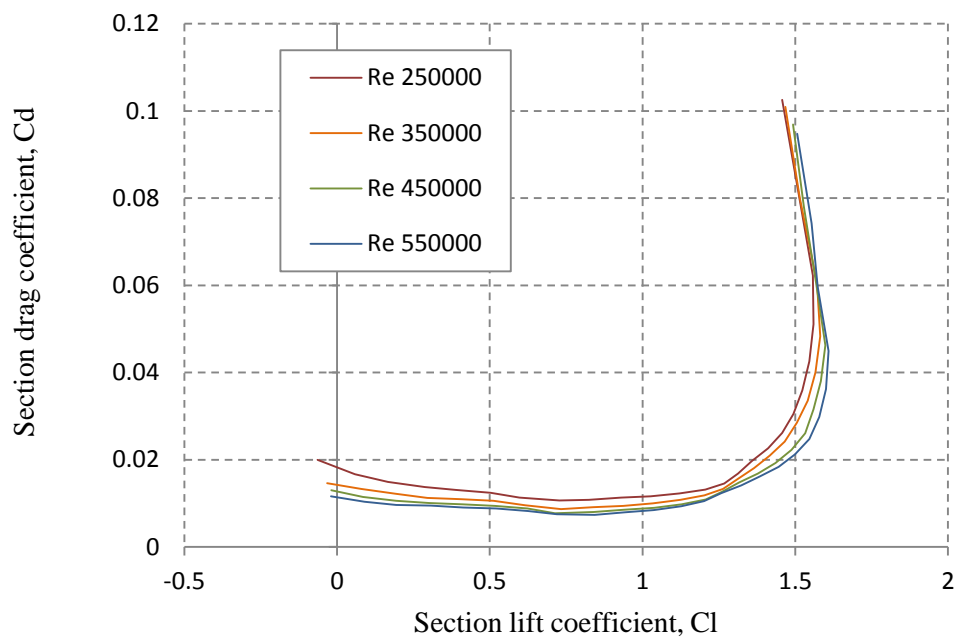


Figure 28: Drag polar, Blended airfoil "new4" C_L vs. C_D .

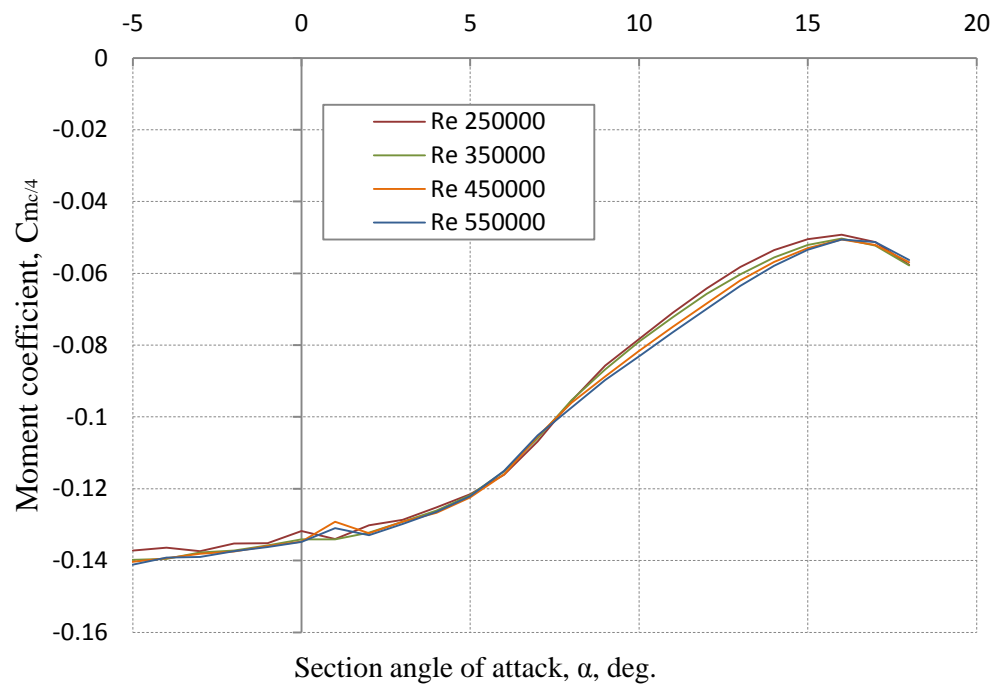


Figure 29: Moment Curve, Blended airfoil "new4" C_m vs. α .

The airfoil chosen was used in extensive iterations to decide the acceptable planform for the desired flight envelope. Basic aerodynamic equations were used changing wing area and aspect ratio independently within the range of Reynolds numbers and velocities expected. The final sizing is detailed in Table 8.

<i>Table 8: Final Sizing</i>	
GTOW	35 lb.
Wing Area	6.125 ft ²
Span	7 ft
AR	8
V_{stall} (no flaps)	36 knots
V_{cruise}	55 knots

In order to reach desired stall speed at GTOW, flaps are desirable. Additionally, the aircraft needs removable outboard wing sections in order to fit into a truck or van. The inboard section was sized to provide enough flap area for the stall requirements and to support the bulk of the flight loads since removable sections are less structurally efficient. The flaps considered are simple flaps with the hinge on the bottom skin, such as is common in composite SUAS. The flaps were modeled by altering the airfoil in XFOIL (Figure 30), and saved as a DAT file for further XFOIL²³ and XFLR5 analysis.

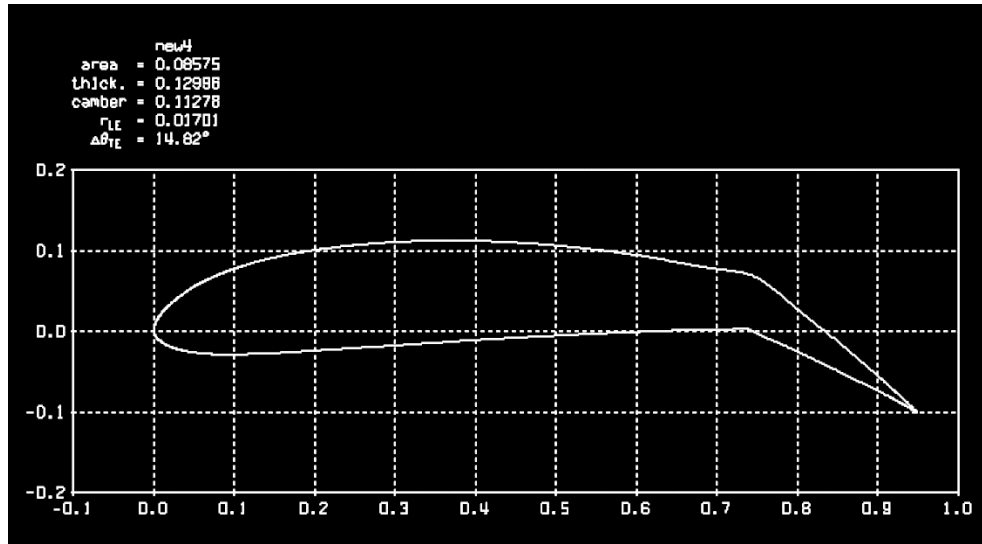


Figure 30: Altered airfoil for analysis, a 25% percent area 20 degree deflection flap.

The flaps considered for MARIA are within a reasonable range with the flap percentage not exceeding 30% of the airfoil and the deflection not exceeding 30 degrees. Five flap settings were analyzed within this range. With XFLR5, the inboard section of the wing was set with the DAT file generated in XFOIL with the specific flap. One of the flap settings in XFRL5 is shown in Figure 31. Figure 32 gives the wing performance for different flap settings.

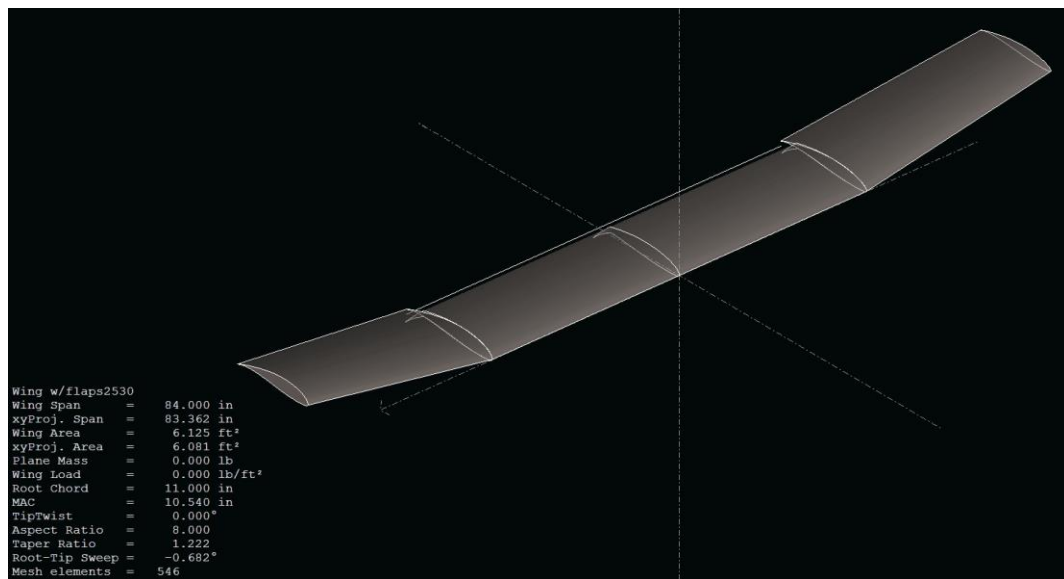


Figure 31: Wing modeled in XFLR5 with inboard flaps.

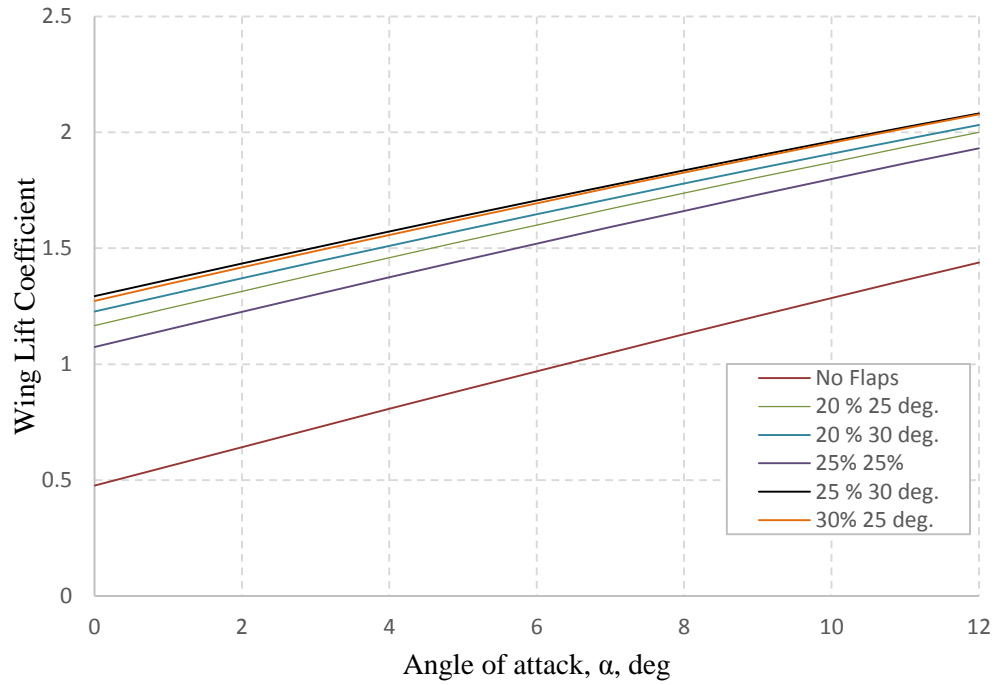


Figure 32: Flap predictions for wing using XFLR5 in inviscid setting.

The best performing altered airfoils were also run within the range of Reynolds numbers in XFOIL. The airfoils were run at the lower end of the range since the flaps will only be deployed at low velocities. The results from the 25% flap at 25 degree deflection is shown in Figure 33.

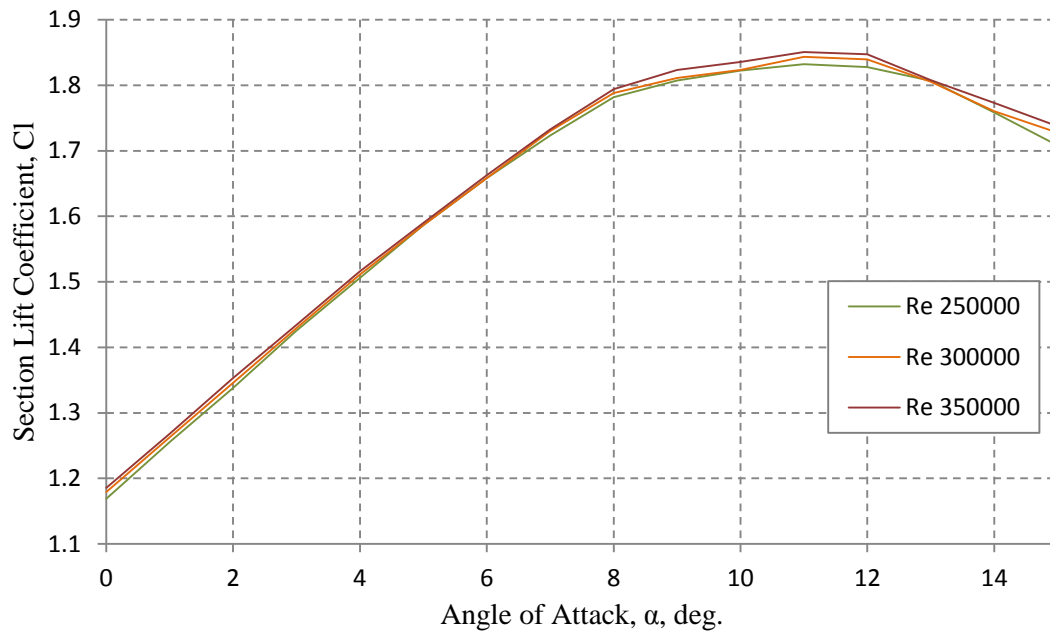


Figure 33: Stall speed with 25 % 25 degree flap airfoil alteration, a range of Reynolds numbers.

The design flap configuration for minimum stall speed is 25 % at 30 degrees. This brings the stall speed to an acceptable 29 knots. The inboard section of the wing is half the span with a constant 11 inch chord; the outboard sections have a slight taper with a tip chord of 9 inches.

4.1.2 Stability

Since MARIA will be flying in a highly dynamic environment, it is necessary that it be largely stable. Even with a stabilizing autopilot, the gusts will create a difficult flight environment. This is especially true at the low speeds required by some onboard sensors. The tail sizing process consisted of benchmarking, stability calculations, structural considerations, and optimization until the stabilizer specifications were finalized. The process was begun with aerodynamic surface sizing close to benchmarking, then adjusted to ensure that the aircraft trims at the desired α , achieves stability coefficients within the higher range of benchmarked aircraft, and retains a reasonable level of controllability. The horizontal volume ratio is 0.56. Static stability was computed using basic stability equations in Nelson's Flight Stability and Automatic Control textbook.²⁶ The parameters used are in Table 9. The vertical tail was sized to

allow a survivable one engine out scenario and has a volume ratio of 0.23. At the minimum thrust requirement, one engine will create a 1.83 lb*ft moment. The rudder requirements are 30% of the vertical with 45 degree deflection. The aircraft was designed to have stability coefficients and control authority on par with aircraft proven to have high levels of static and dynamic stability. The static and dynamic stability coefficients for MARIA as well as the benchmarked values are detailed in the Appendix.

Table 9: Parameters for Static Stability.

<u><i>Aircraft Characteristics</i></u>					
Xcg/c	0.23	W [lb]	35	lf [ft]	5
AR_w	8	η	0.8	Df [ft]	1.25
AR_t	6	V_H	0.57	S[ft ²]	6.125
		λ	0.818182	c[ft]	0.875
<u><i>Wing Airfoil Characteristics</i></u>					
Xac/c	0.25		<u><i>Tail Airfoil Characteristics</i></u>		
CL_{0w}	0.486		<i>(NACA 0012)</i>		
α_{0L}	-5	deg	CL_{at}	0.1	per deg
Cl_{αw}	0.102	per deg.	Cm_{act}	0	
Cm_{acw}	-0.13		i_t	0	deg
i_w	2				

The above characteristics give a static margin of 0.29 and moment behavior as shown in Figure 34. It shows a stable aircraft with trim at an aircraft angle attack of zero. At this point, the wing is at a 2 degree incidence which has the airfoil at its maximum $C_L^{3/2}/C_D$, the value is approximately 18.7.

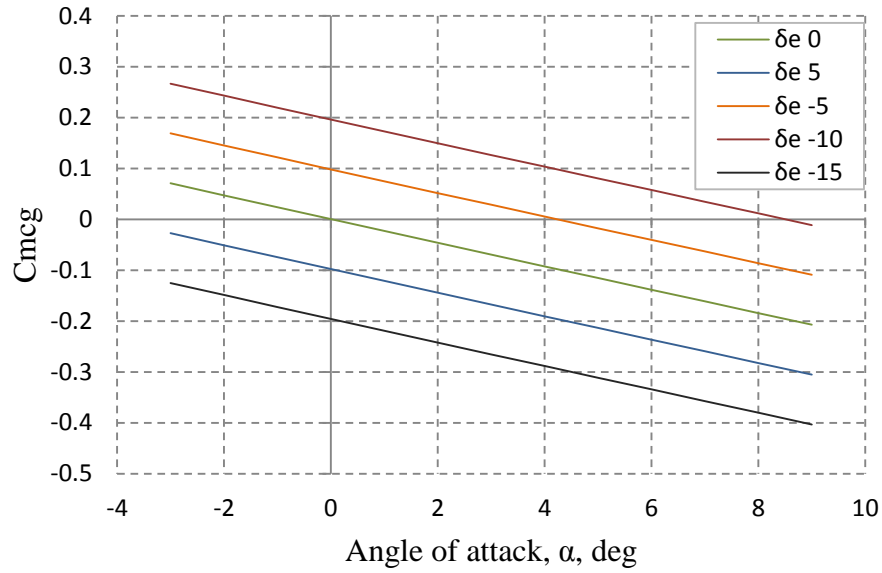


Figure 34: Aircraft's moment coefficient vs. angle of attack at a range of elevator input.

Because of dropsonde deployment, as well as fuel storage, CG travel was an important consideration in the aircraft layout and stability analysis. Within the mission development, the aircraft payload is variant. Figure 35 shows the change in center of gravity location with respect to the aircraft weight, Configuration 1.

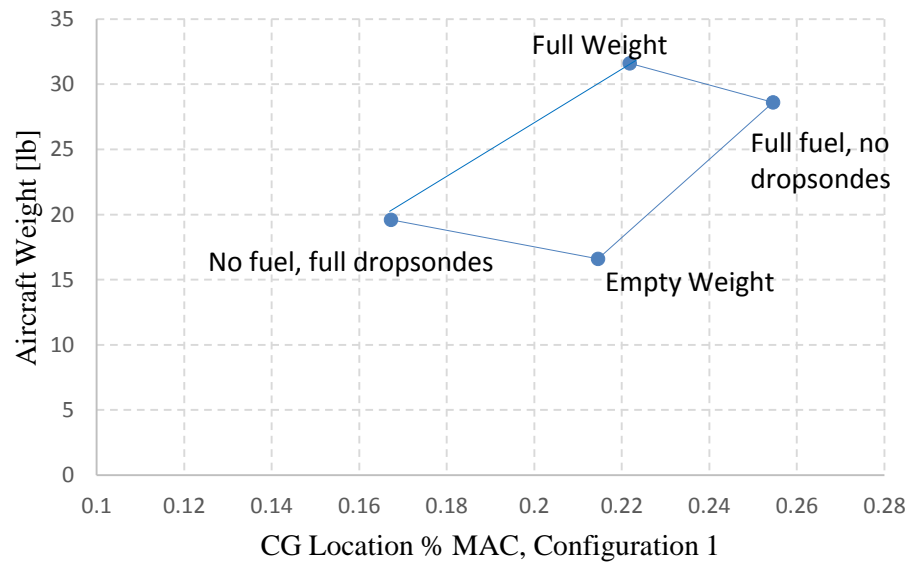


Figure 35: Center of gravity travel plot, Configuration 1.

There is a significant drop in weight from the GTOW and the empty fuel, no dropsonde weight. In order to keep the cg travel in an acceptable range, the fuel is stored on either side of the sensor packages. This is shown in Figure 36; the blue areas indicate fuel storage and the dropsondes are stored in their dispenser between them. Each fuel section has a volume of 200 in³ (0.875 gal).

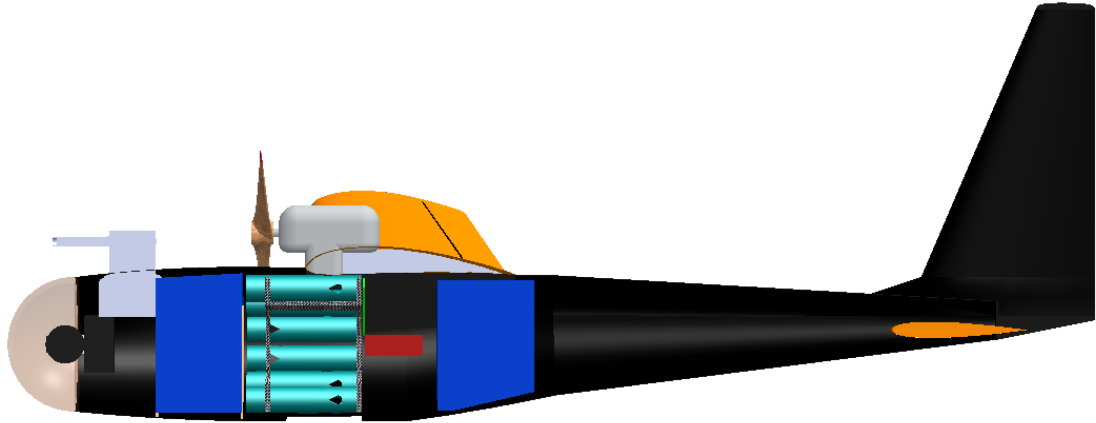


Figure 36: Fuel and dropsonde location, Configuration 1.

. It may prove overly difficult to integrate two fuel tanks into the aircraft. A more simplistic configuration is possible with a single fuel tank, though it extends the cg travel. The cg travel for the fuel tank is shown in Figure 37. The configuration for the single fuel tank is Figure 38. The fuel tank is the size of the small tanks combined.

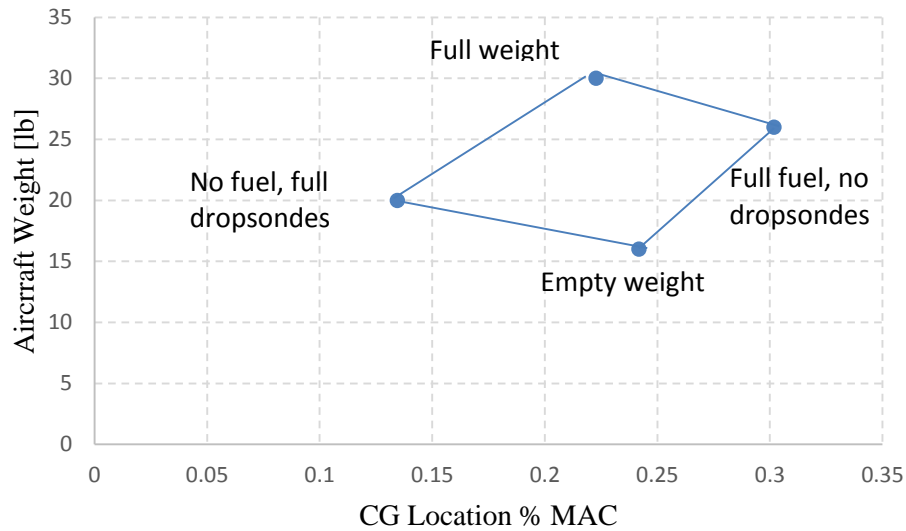


Figure 37: CG travel plot, Configuration 2.

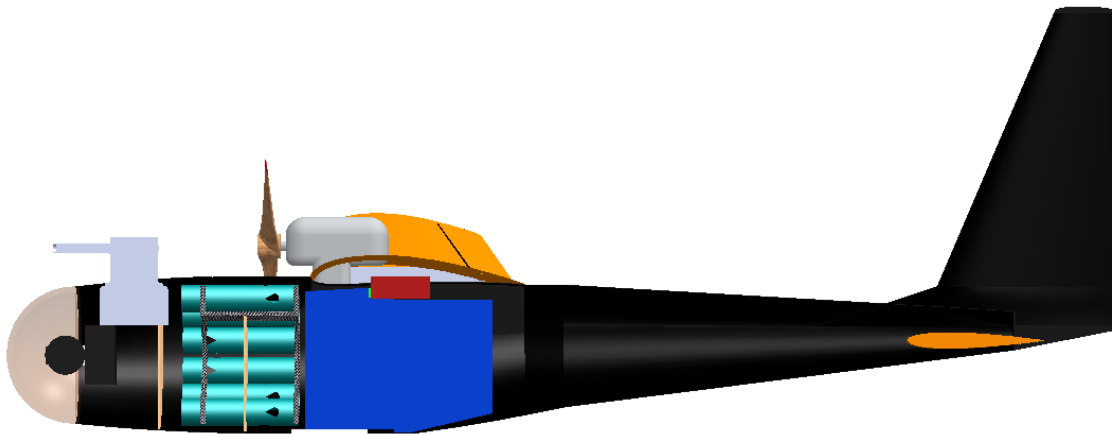


Figure 38. Aircraft layout, Configuration 2.

The electric configuration has the most narrow cg travel since there is no fuel consumption. Full weight is 31lb with the CG at 0.22 of the chord and zero dropsonde state is at 27lb and 0.23 of the chord. The electric internal layout is shown in Figure 39. The weight is higher for the electric set-up because of the high density batteries. This configuration uses eight 5000 mAh LiPo batteries. The performance differences will be discussed in the next section.

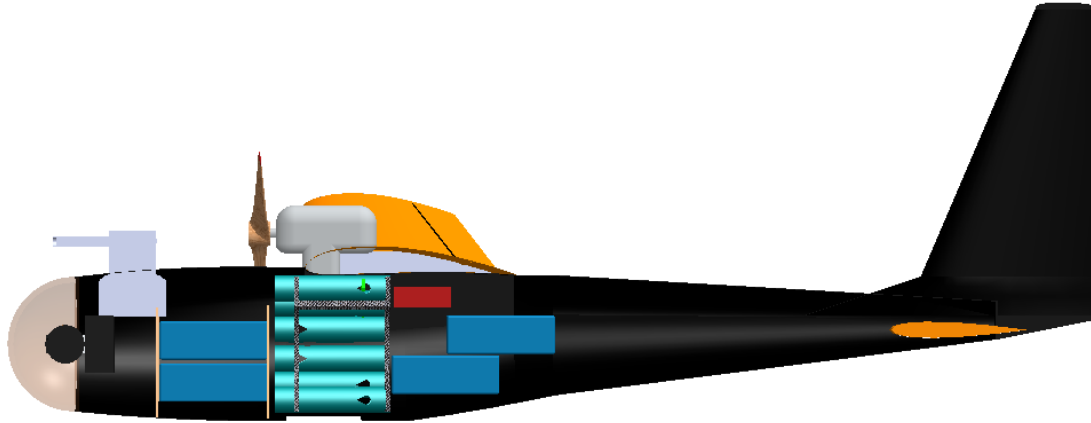


Figure 39: Aircraft layout, electric propulsion.

4.2 Propulsion System

The sensors being carried onboard require clean airflow. This precludes a tractor configuration, as discussed previously. A pusher configuration with a split tail and a twin wing mounted engine configuration were the two considered for final design. The twin-engine design was desirable for propulsive redundancy and increased maximum velocity. Additionally, the continuous fuselage was also more structurally efficient than the split tail configuration, as will be discussed in Section 4.3. Thus, the configuration chosen was the twin engine tube fuselage design.

Both gas and electric engines were considered for MARIA. With an endurance goal of over six hours, the most feasible propulsion system is gas. However, an electric propulsion is an attractive solution for its ease of use. The flight envelope for MARIA comparing the electric propulsion system option and two-stroke engines option is presented in Figure 40. As shown, the gas propulsion system allows for a significantly larger flight envelope.

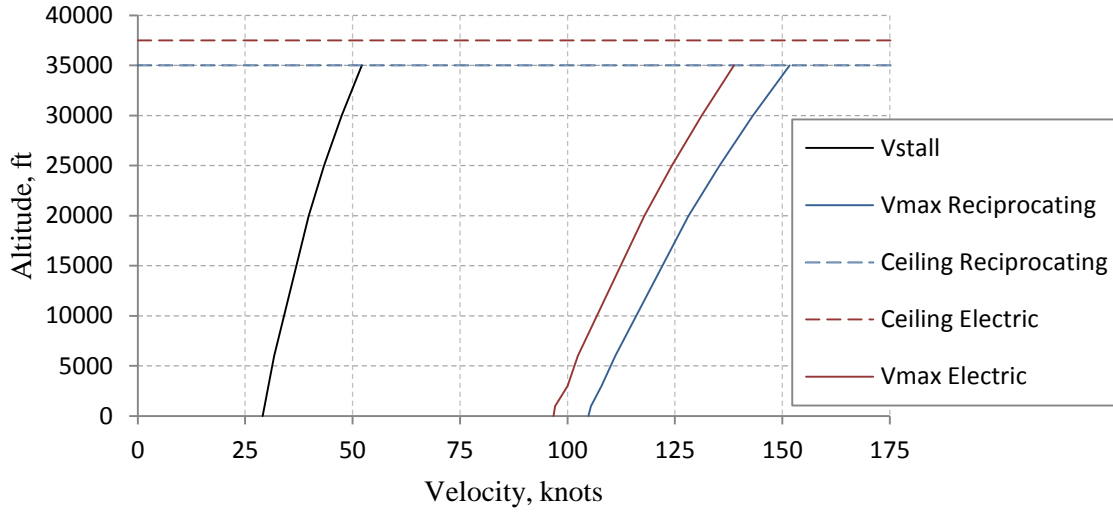


Figure 40: Flight envelope for both gas and electric propulsion options.

The electric propulsion system would require sixteen six cell 5000 mAh batteries to achieve the eight hour endurance objective. This would weigh over twice the fuel weight with the reciprocating engines. Thus for the operational system a gas propulsion system is preferable. However, it was decided that an electric system will also be chosen to mimic the operational gas system, for the MARIA demonstrator system. This allows the test aircraft to be flown more easily until basic flight worthiness is demonstrated.

A drag build up was developed using the method in the Gundlach's book.²⁵ The parasitic drag uses a summation method for the various aircraft components.

$$(C_{D0})_{\text{subsonic}} = \frac{\Sigma(C_{fc}FF_cQ_cS_{wet_c})}{S_{\text{ref}}} + C_{D_{\text{misc}}} + C_{D_{\text{L\&P}}} \quad (12.24)$$

This considers skin friction with estimated laminar percentages, all external sensors, engines, interference drag and induced drag. The friction factors for the various components were determined from the equations in the textbook. The parasite drag is summarized in Table 10.

Table 10: Summary of the predicted parasite drag from the aircraft.

<u>Parasite drag</u>	
Component	Drag Coeff.
Skin Friction	0.0086
TAMDAR	0.0051
Flap	0.0173
L&P	0.0031
Engines	0.003
Cd0	0.0371

The total drag build up spreadsheet is in the Appendix. It was determined that MARIA needs at least 2.8 total HP to encompass the entire flight envelope for steady and level flight (Figure 41). Therefore, each one of MARIA's engines must be capable of producing at least 1.4 HP. Due to the known hazards and extreme flight conditions associated with supercells, a minimum of 4.0 total HP was selected as a requirement in order to give MARIA enough excess power to help combat some of the extreme flight conditions.

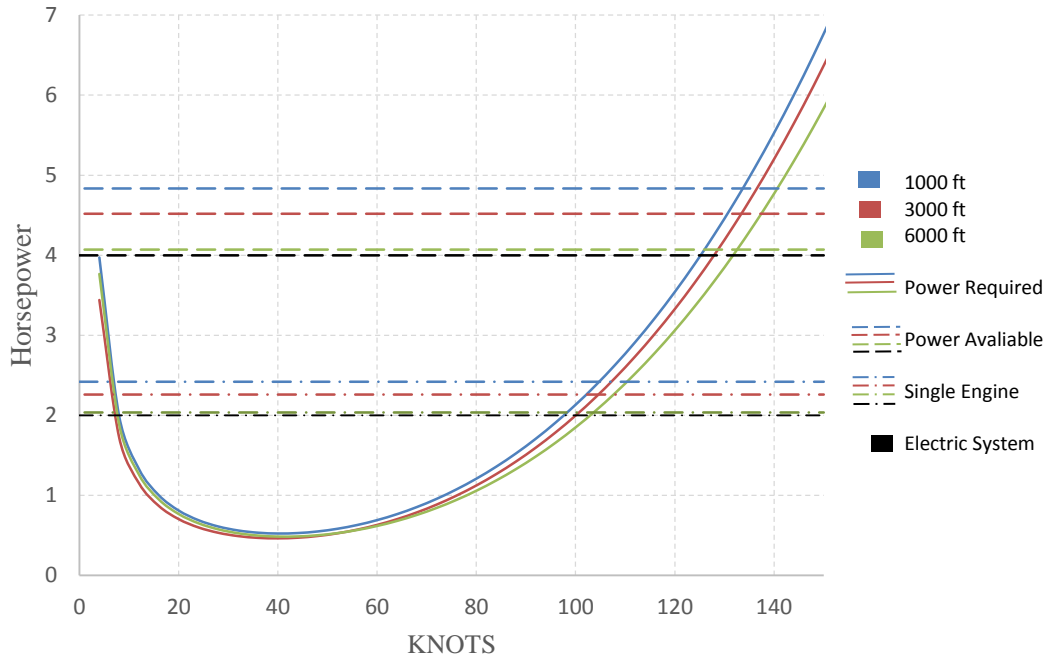


Figure 41: Power Required GAS AT SL

In order to determine the most viable gasoline propulsion system for MARIA, research was performed to gather the technical characteristics for 13 separate gasoline powered engines capable of producing at least 2.0 HP. The bulk of the work involved in the propulsion system selection was done by Ryan Gifford and Jake Hathaway. The rationale will be briefly discussed as well as the final selections made.

4.2.1 Reciprocating Engines

The power available shown above in Figure 41 is from the DLE 20 two stroke engine chosen. This is a commercially available 20cc engine with a relatively low cross-section and cost. It is capable of 2.5 HP and weighs approximately 2.5 lbs. The engine is shown in Figure 42.



Figure 42: DLE-20²⁶

In order to balance the torsional forces from rotation, the engines will be counter-rotating. A counter-rotating set will be purchased from the manufacturer. The performance predictions for this operational system are in Table 11. The propellers to be tested are 15x8, 16x6, and 16x8 Beechwood propellers. An endurance prediction for the reciprocating engines at 1000ft is presented in Figure 43. This is based off of manufacturer specifications, and will be reevaluated upon engine testing.

The engines will be installed with the muffler downwards into the leading edge of the wing, in order decrease cross-sectional area. It will also be covered by a composite cowling made in house with left-right molds. The plan for its installation is shown in Figure 44.

Table 11 Performance Predictions, Operational System.

Stall speed	36 knots
Maximum Speed	110 knots
Cruise Speed	55 knots
Endurance	8 hrs.
Service Ceiling	30,000 ft.

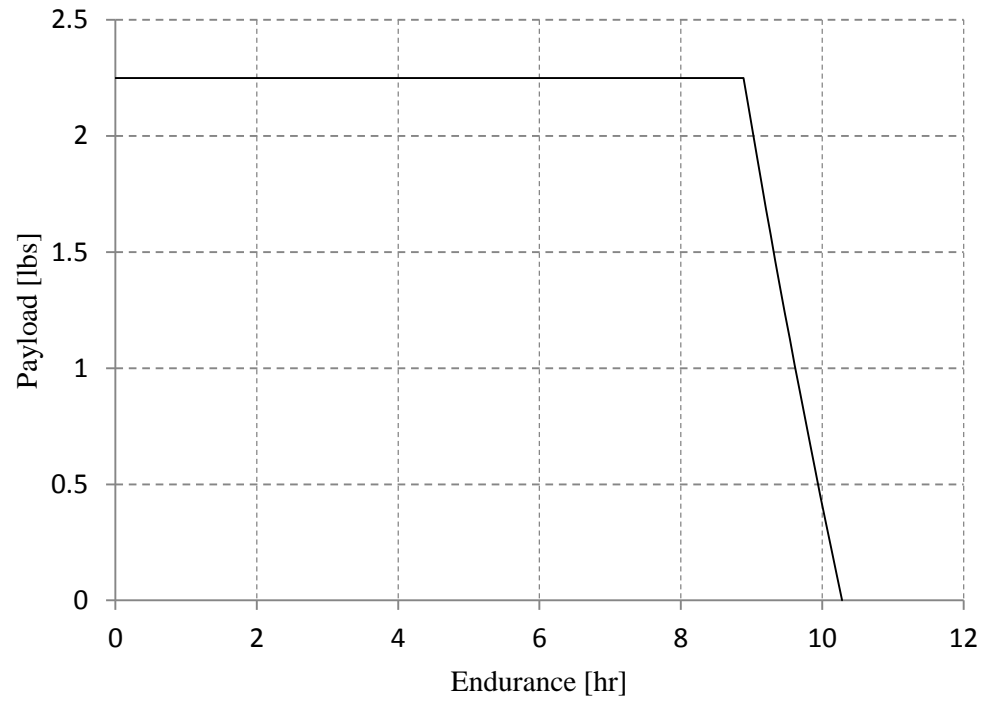


Figure 43: Payload versus endurance, 1000ft.

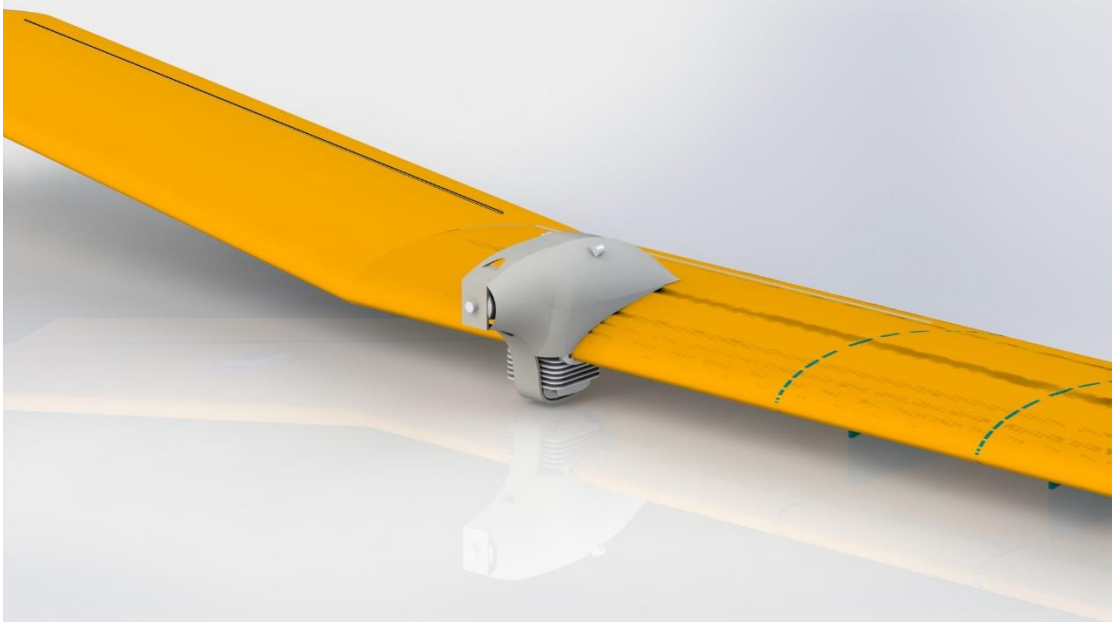


Figure 44: DLE-20 Engine as will be installed on the wing.

4.2.2 Electric Motors

The test aircraft's electric motors were chosen to mimic the performance of the reciprocating engines as closely as possible, designed to provide comparable thrust and rotational speed. The electric motors are Rimfire Outrunner Brushless motors from Great Planes. They are 50mm diameter motors with a kV of 450 rpm.

The endurance characteristics for the electric motors are shown for an altitude of 1000ft, with two batteries for each motor. Figure 45 shows the estimated endurance for the aircraft as if it was flown at the respective horsepower for the duration of the flight. From this, Figure 46 was generated to show the approximate endurance if the aircraft is flown at a near constant velocity.

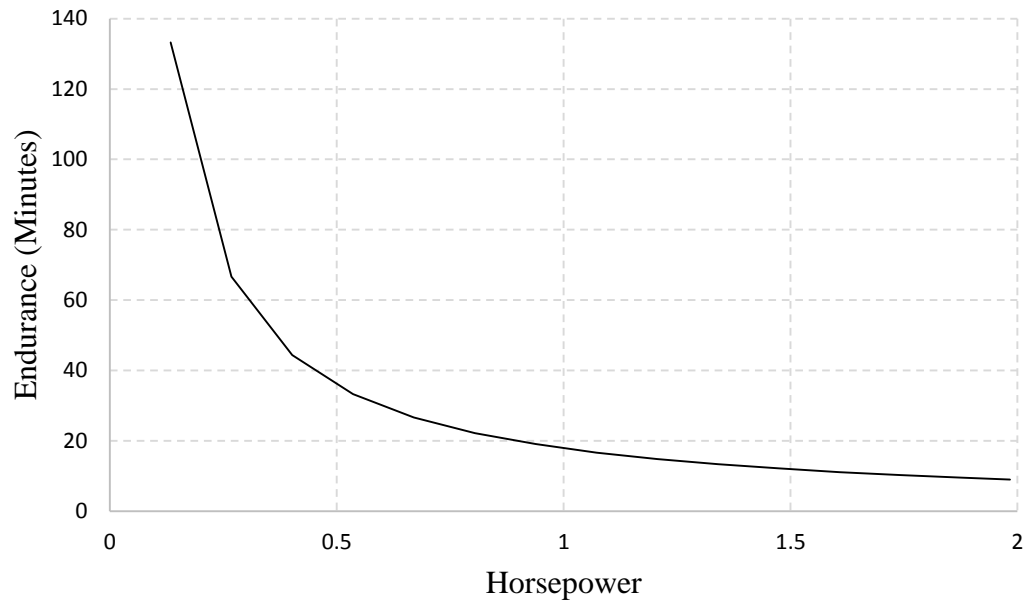


Figure 45 Endurance with respect to horsepower.

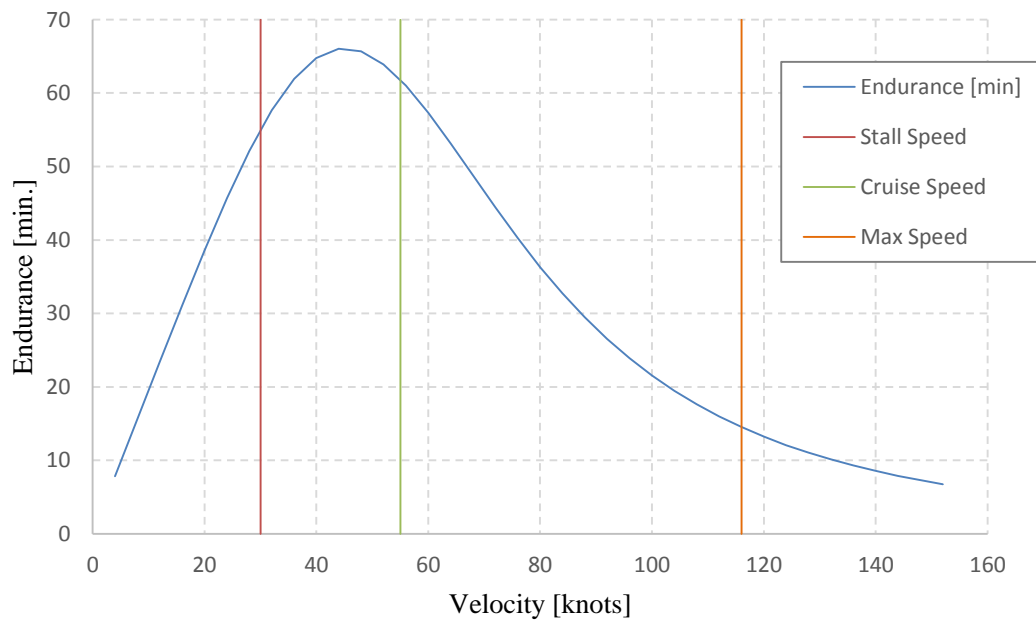


Figure 46: Endurance with respect to velocity.

The aircraft is capable of carrying four batteries for each motor, at maximum weight capacity.

This would double the endurance but still be about a quarter of the endurance provided by the

reciprocating engines. These motors will be installed using an aluminum motor mount bolted to a composite plate epoxied to the main spar. Simple cowlings were made from off-the-shelf wheel pants and fixed over the motors and mounts, Figure 47. These motors will also be counter-rotating. For electric motors this is an easy adjustment in the set-up and can be done by switching wires from the motor to speed controller. The propeller used for this test system is a 15x10. The propeller options are limited by the relatively few counter-rotating sets of propeller available.



Figure 47: Electric Motor Cowling

4.3 Structure

4.3.1 Loads

The airframe was designed to withstand gusts and hail as well as standard flight loads encountered during launch and landing. The airframe and launcher are required to fit into a van or truck. In order to meet this requirement, the outboard sections of the wings are removable. This creates an aircraft built from five parts: fuselage, horizontal tail, inboard, and two outboard wing sections. The major areas for concerns are fuselage tail section, inboard wing section, and wing joints shown in Figure 48. The inboard section provides the majority of lift and is more subject to hail damage. The fuselage empennage narrows in the aft section and is less able to withstand normal and torsional loads. The wing joints must be designed such that small connection points carry all the load from the outboard sections and are durable with repeated use.

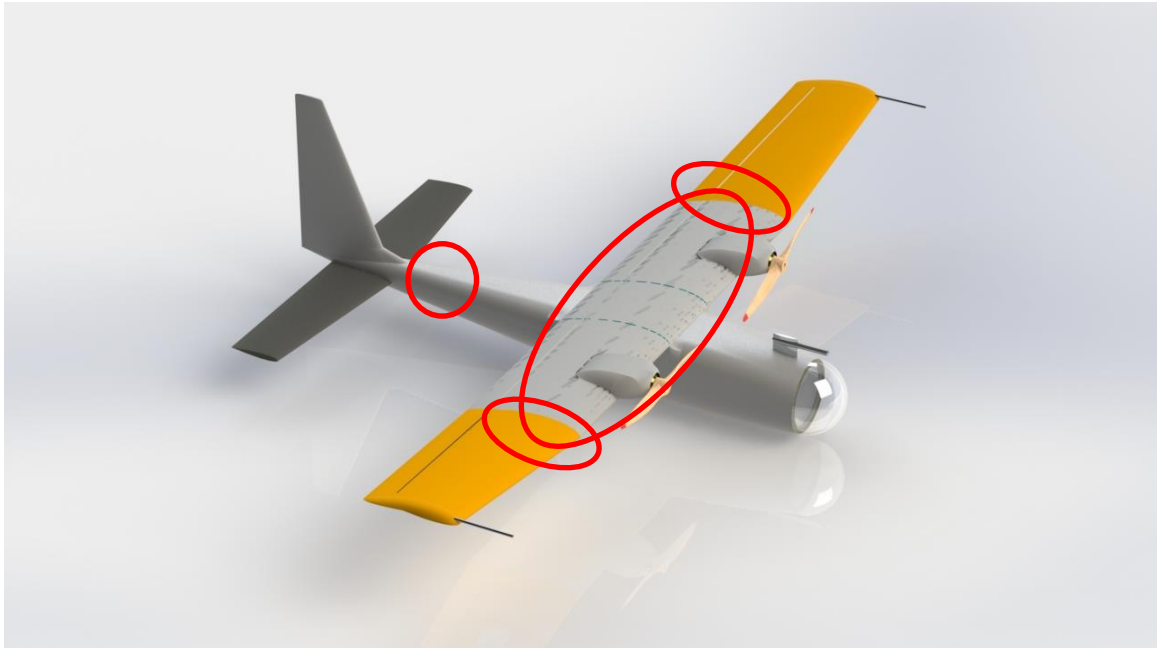


Figure 48: Areas for special structural attention

In the design parameter stage of this project, it was decided that MARIA should be able to survive an 80 mph gust. Analyzing flight loads for an 80mph sudden gust, the g loading is 5.5g at GTOW and 14.5g at empty weight. Since it is unlikely that the completely unloaded aircraft will experience an 80mph gust, a design structural limit of 10g was selected. A 10g load exceeds

any other expected flight loads, as shown by the V-n diagram in below in Figure 49. The maximum resultant aerodynamic loads with an 80mph gust produced by each aerodynamic surface are presented in Table 12.

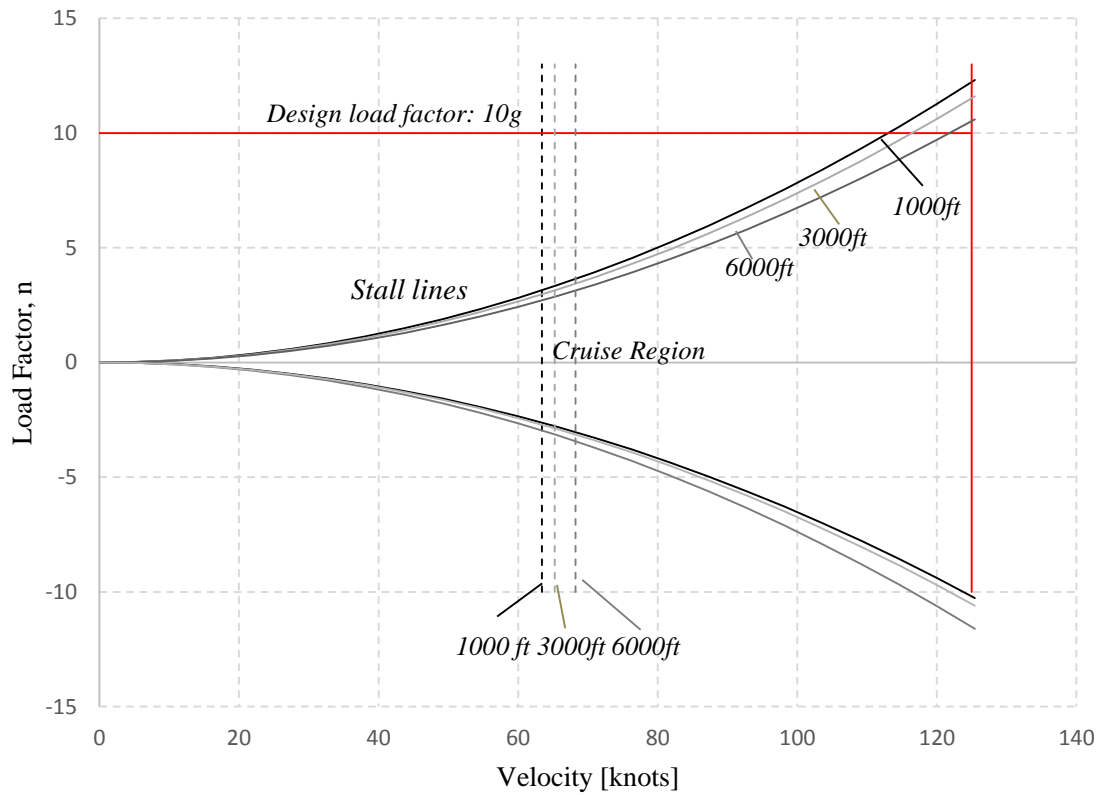


Figure 49: Flight envelope and V-n diagram

Table 12: Resultant gust loads

	Load[lb]	Moment [lb ft]	Torsion [lb ft]
Inboard Wing	248	217	5.01 yz plane
Outboard Wing	53.3	44.3 on wing connection join	7.14 yz plane
Horizontal Stab.	16.7	49.5 on empennage	8.25 xy plane
Vertical Stab	7.92	23.6 on empennage	55.4 xy plane

The airframe skin is not expected to withstand impact forces from hail except in the wing and horizontal stabilizer. Even these surfaces are designed only to survive impact from quarter sized hail.

4.3.2 Materials

A metal aircraft would simply not be feasible for an aircraft of this size. The weight of material would too large to encompass the design characteristics. Additionally, a build-up composite method would be drastically inefficient at the design loads; this method uses only internal structure to carry load. For the loads intended, the skin is capable of carrying a significant amount of torsional and shear load; a method that fails to take advantage of that would require extremely heavy internal structure. The best option for MARIA is the lay-up composite method for which OSU's manufacturing lab is designed. This composite method uses a semi-monocoque structure with the skin and internal structure sharing the loads. The wing generally carries most of the load in the main spar whereas the fuselage loads are mostly distributed in the skin.

The materials chosen are ones commercially available as a dry fabric. Both balsa and vinyl core will be used in the aircraft. For internal structure stock material, balsa will be used. It is directionally strong in shear and can be used advantageously to add shear strength to longerons, shear webs, ribs, and bulkheads. Vinyl core is not directionally dependent and adds stiffness and

shear strength to wing, fuselage, and tail skins. In the interest of cost, the airframe skin will consist primarily of fiberglass. Various components are strengthened with carbon fiber in areas where stiffness is needed or aramid fabric for impact forces. Table 13 compares the cost and advantages of the main materials used.

Table 13: Cost of materials and sample of advantages²⁸

	Fiberglass	Carbon Fiber	Aramid
Approximate Cost	\$2/oz.	\$35/oz.	\$14/oz.
Young's Modulus (Stiffness)	25 GPa	85 GPa	30 GPa
Ultimate Tensile Strength	1000 MPa	1000 MPa	1300 MPa

The various parameters of the fabric, weight, weave, and thickness, are chosen from structural analysis and manufacturing ease. For instance, some fabrics are more capable of being formed into complex mold lines and are less likely to fray during the lay-up process. The qualitative advantages and disadvantages of different material options often play a large role in the quality of the part.

4.3.3 Analysis

The aircraft is composed primarily of composites. Since composites are difficult to numerically analyze, the structural analysis consists of hand calculated estimates, limited FEA verification, and structural testing. The airframe skin is fiberglass with the wing skin reinforced with aramid fabric for hail protection. The skin carries a high percentage of the load, but some internal structure is required to meet the design g loading. Figure 50 shows the basic internal structure of the aircraft. A carbon fiber, fiberglass and balsa sandwich is used for the shear webs, ribs, and longerons. The analysis methods used are standard wing and fuselage idealization methods for torsion, shear, and bending. For shear estimation, the airfoil was idealized as three

cell section, shown in Figure 51. The three cells are made from the skin, main spar, and aft shear web.

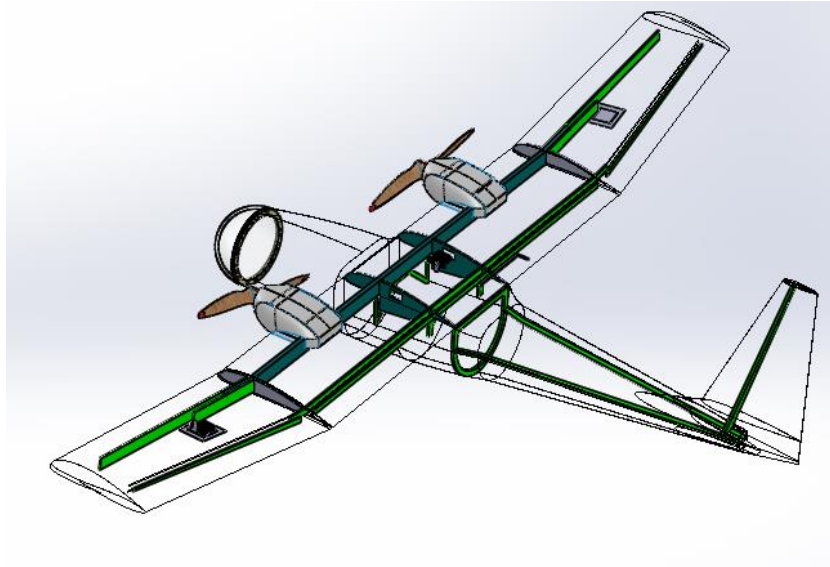


Figure 50: Internal structure

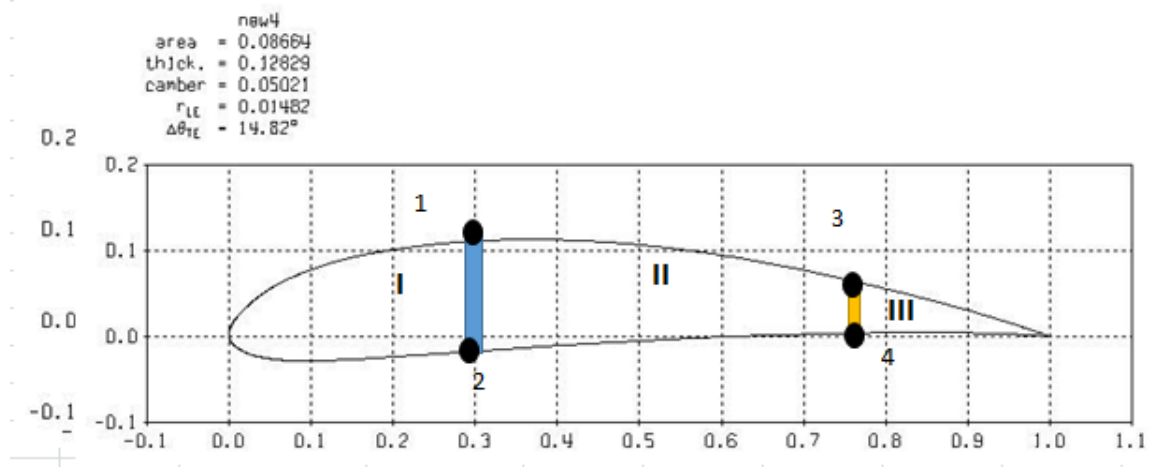


Figure 51: Shear flow idealization format, three cell section

A summary of the shear flow analysis results for the inboard wind is in Table 14. The resultant safety factor is approximately five. The thicknesses cited are not actual thicknesses but dimensions scaled by a reference modulus of rigidity.

Table 14: Shear flow inboard wing

Wall	Length [in]	Thickness*	δ	τ
12o	7.12	0.03058	232.83	946.15
12i	1.51	0.05753	26.25	-14.88
13	4.43	0.03058	144.87	974.15
24	4.42	0.03058	144.54	974.15
34i	0.67	0.04885	13.72	420.92
34o	5.99	0.03058	195.88	301.75
				5.34

The most critical part of the fuselage was also idealized for analysis. The idealized cross-section is shown in Figure 52. This is a symmetric cross-section; any lack of symmetry in the sketch is unintentional. This cross-section was analyzed for normal and torsional stress, a summary of which is in

Table 15. The analysis method uses standard closed cross-section shear flow methods to determine torsion and simple bending equation with variable cross-section.

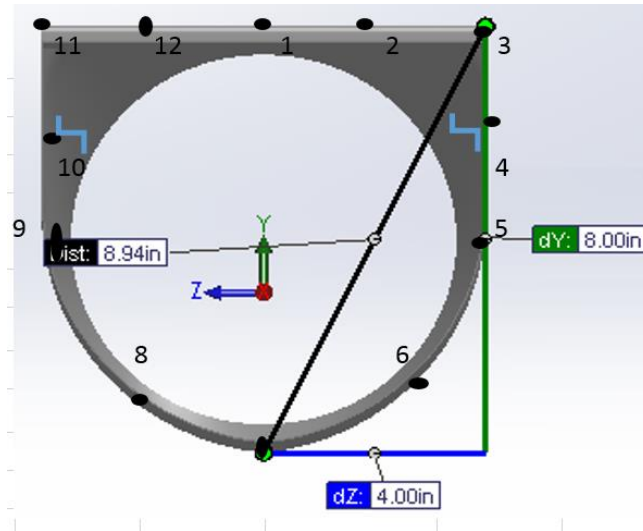


Figure 52: Fuselage cross-section idealization format

Table 15: Fuselage stress analysis by idealization

Boom #	A _B	A _B *y _b ²	σ _z (psi)	q _b (lb/in)	A _{ab} [in ²]	Aa _{ab} *q _b	q _s [lb/in]	τ (psi)
1	0.03	0.23	4699	-8.3	4	-33.2	-10.3	-686
2	0.03	0.23	4699	-17	4	-66.5	-18.6	-1240
3	0.03	0.23	4699	-25	4	-99.7	-26.9	-1790
4	0.13	0.076	1301	-35	4	-139	-36.9	-2460
5	0.039	0.059	-2096	-30	6.3	-189	-32.1	-2141
6	0.047	0.39	-4911	-16	6.3	-104	-18.5	-1231
7	0.047	1.29	-8892	8.2	6.3	51.5	6.22	414.6
8	0.047	0.394	-4911	22	6.3	137	19.9	1324
9	0.039	0.059	-2096	27	4	106	24.6	1641
10	0.13	0.076	1301	17	4	66.5	14.6	976.8
11	0.03	0.23	4699	8.3	4	33.3	6.34	423.0
12	0.03	0.23	4699	0.023	4	0.0912	-1.96	-130.8
		SF	9.29				SF	2.95

The full spreadsheet for the analysis of the inboard, fuselage, and the other components is in the Appendix.

Solidworks' FEA software was used to check general stress patterns and deformations. Material properties for the aircraft skins and stock materials were put into the model as composite materials. The results, however, are not considered quantitatively robust, because of the shortcomings in composite calculation. One major issue with the results was a result the closely interlocking parts and nonstandard shapes. Often, touching splines is a rib and skin caused an interference error prior to the analysis completion. Additionally, in some loading cases, the internal structure separated from the skin in ways contrary to logic and experience. A number of loading cases, however, ran successfully and presented reasonable results in conjunction with the spreadsheet analysis. Figure 53 below shows a predicted stress gradient as a result of a starboard side gust. The top picture is the outer mold line of the fuselage and the bottom picture is an exaggerated deformation from the loading.

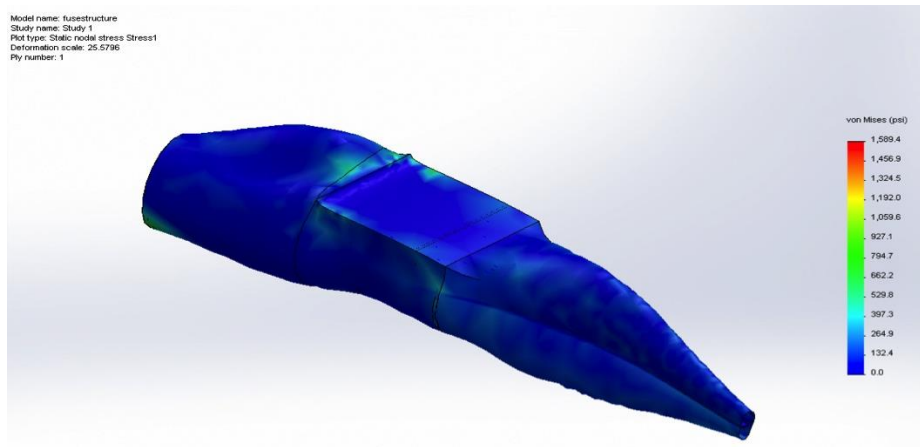
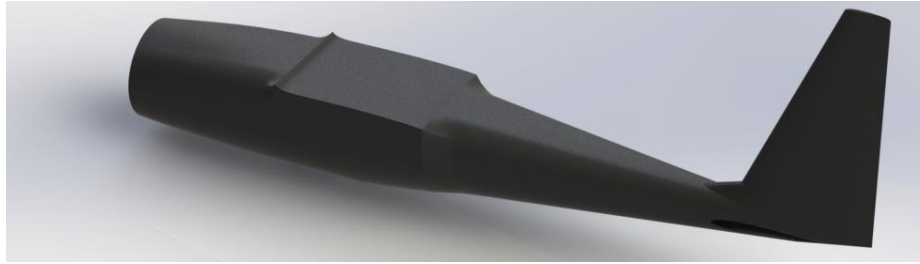


Figure 53: Fuselage stress analysis starboard-side load

Figure 54 shows a loading case for the inboard wing and the resultant strain plot with exaggerated deformation. The most inboard ribs are modeled as fixed and a distributed load of 15 lb.

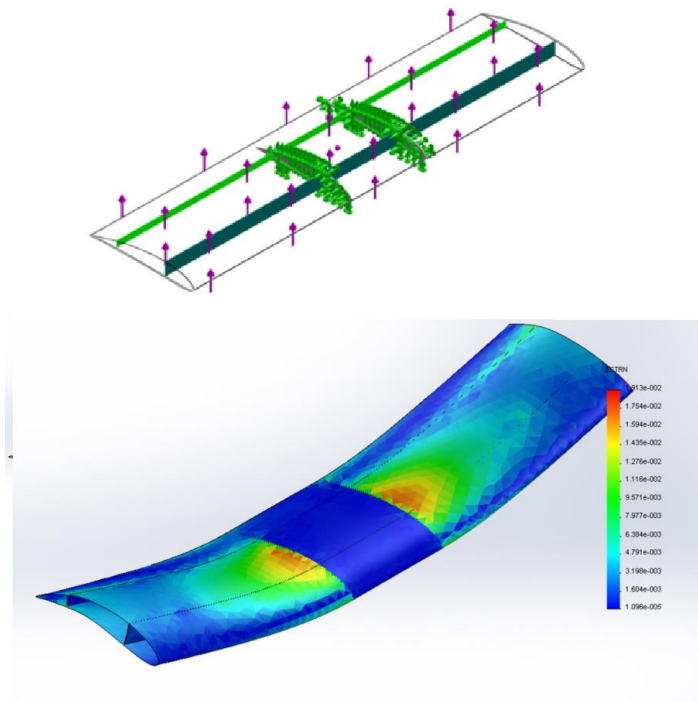


Figure 54: Inboard Wing, loading case and deformation/strain plot

A more extensive description of the SolidWorks FEA model in is the Appendix.

CHAPTER V

AIRFRAME BUILD

5.1 Manufacturing Process, MARIA I Build

The airframe construction consists of the general process for small UAS. An overview of this build process is presented here; for a more detailed description of the type of composite manufacturing implemented consult the thesis of Daniel Hunt.²⁷

Plugs were cut out with a CNC machine from the CAD of the five aircraft parts. Figure 55 shows the top of the inboard wing section being cut out by the CNC and Figure 56 shows the two halves of the fuselage plugs being joined.



Figure 55: Inboard wing section plug, top part



Figure 56: Fuselage plugs

The plugs were cut out of a low density machinable foam. The plugs were then primed and sealed for mold manufacturing. This consists of painting and sanding the plug until machining lines are gone and the foam is sealed. The plugs are then released and used to make molds. A total of nine molds are required to create the skins of the airframe. The molds consist of a thick epoxy layer and heavy fiberglass. Figure 57 shows a fuselage mold directly after its lay-up on the plug and an outboard wing section after it is separated from the plug.

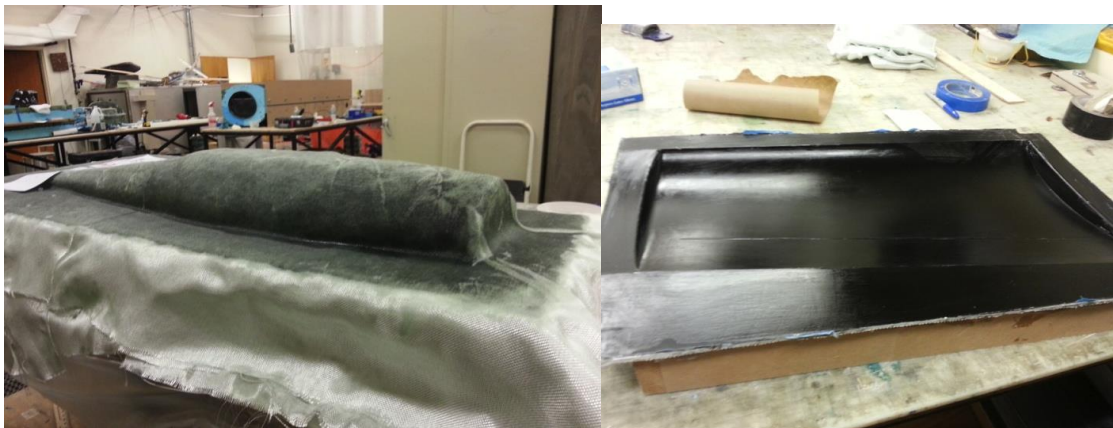


Figure 57: Fuselage mold and an outboard wing section mold.

Once all nine molds were constructed, composite skins were layed-up into the mold. The fabric thicknesses and direction are dependent on expected loads. Figure 58 shows the skin for the inboard wing section. It is made from fiberglass fabric, with vinyl core

and unidirectional carbon fiber as a spar cap. These cure under vacuum pressure in the mold. After all skins were completed the parts were joined with composite internal structure and the airframe goes together. The six control surfaces were cut out of the vertical, horizontal, outboard wing sections, and each side of the inboard wing section. Each control surface is built to pivot on an aramid hinge placed in the lay-up. The servos are inside the wing sections for flaps and ailerons, and are in the fuselage for the rudder and elevator. The servos are mounted to the top skin with actuators out of the wing skin. For flaps, the actuating wires are inside the fuselage; aileron control uses direct drive servo control.

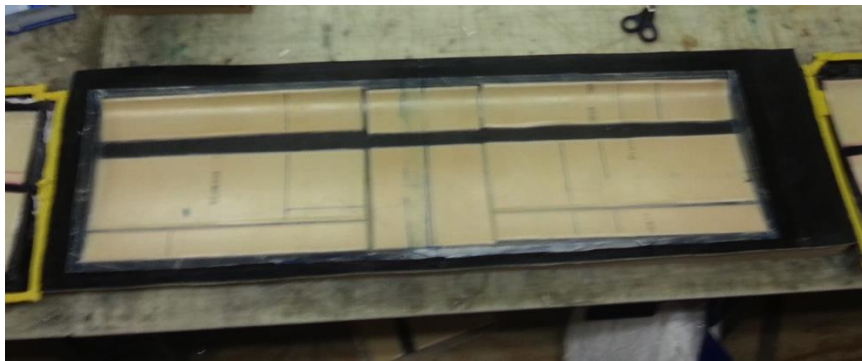


Figure 58: Inboard wing skin.

The final weight for the prototype aircraft structure (including servos) is 5.38 lb. The operational aircraft will require additional structure for the expected gust loads and hail impact, therefore will be slightly heavier. The prototype aircraft was built with a lighter structure to conserve cost and manufacturing time. The weight breakdown is below in Table 16 and the prototype is shown in Figure 59.

Table 16: Structure weight breakdown.

Aircraft Section	Weight [oz.]
Fuselage	29.6
Inboard Wing	25.1
Port Outboard Wing	11.5
Starboard Outboard Wing	11.6
Horizontal Tail	8.32
Total Weight	86.0

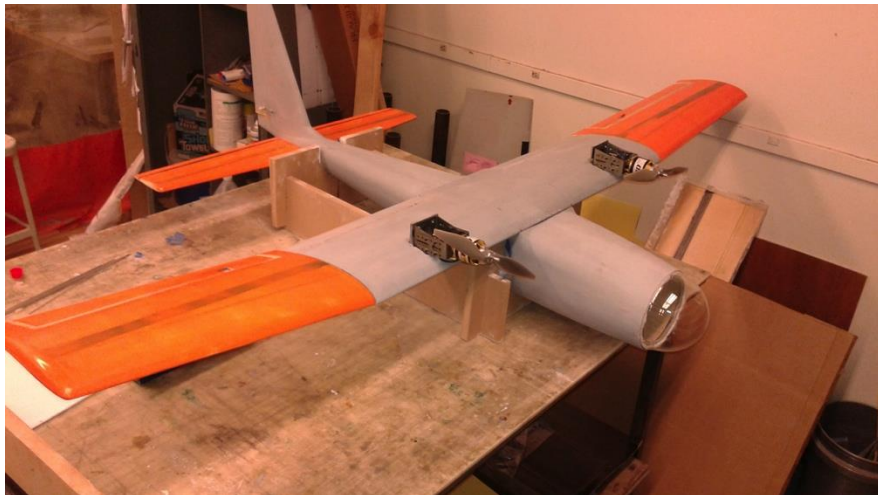


Figure 59: Assembled MARIA I airframe.

Since, the launcher system was not ready for the prototype tests, it was outfitted for landing gear. A simple tricycle configuration was chosen. It was sized under the landing gear guidelines in the Brandt aircraft design book.²⁹ Additional internal structure was installed in the fuselage to carry the loads from the gear. The installed landing gear is shown in Figure 60



Figure 60: Landing gear.

The added internal structure, landing gear and installed propulsion system brought the total airframe weight to 13.16 lb. The final aircraft is shown in Figure 61.



Figure 61: MARIA demonstrator.

5.2 MARIA II Build

The operational MARIA aircraft is built to withstand the full design loads. This airframe is built with more expensive and more arduous materials, carbon fiber and aramid fabric respectively. The inboard wing spar will be a c-channel instead of a shear web and spar cap in the

lay-up. Additionally, the outboard to inboard wing connection will use carbon fiber tubes. This wing joint connection for the operational system is more robust than the former extended outboard spar connection used in MARIA I. This connection uses two carbon fiber tubes that fit into one another to carry the load and fix movement in the xz plane the connection also has a secondary point of contact at the aft shear web to stop rotation. Figure 62 shows both wing connection designs. The picture on the right is of the MARIA II build with carbon fiber tubes that fit together. In both of these designs, the joint piece extends from the outboard section into the inboard wing. This keeps the maximum transportable aircraft width to a minimum.

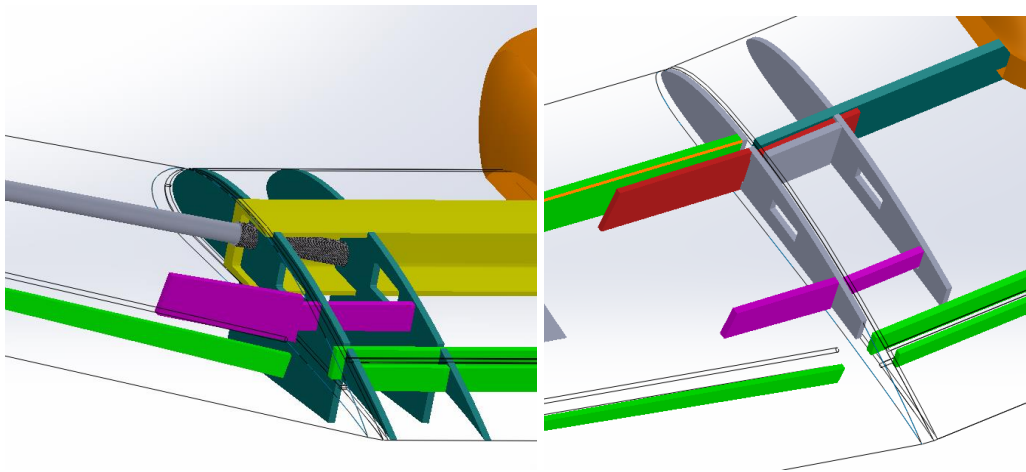


Figure 62: Outboard to inboard joint connection; MARIA II left, MARIA I right.

MARIA II will use the same molds as the first airframe, only changing the lay-up composition and some internal structure. This second build will also change in a myriad of small ways from the lessons learned by the first aircraft.

In order to save time and complication, the first iteration used a standard I-beam main spar instead of a more efficient C-channel. The C-channel provides a better bond between the web and flange of the spar, since it is formed in one continuous piece. The I-beam spar cap method uses uni-directional in the skin lay-up as the spar cap and a separate shear web for the spar web. This can result in an imperfect bond between the cap and web during wing joining.

For the operational MARIA, a C-channel will be used in the inboard section of the wing. The C-channel requires a separate mold and this was constructed using the same method as before, with a machined plug and a female mold. The mold is shown in Figure 63. The resultant C-channel after lay-up is shown in Figure 64; this will be trimmed and joined to the wing skins with the other internal structure.



Figure 63: C-channel mold, for inboard spar.



Figure 64: C-channel

The design wing skin includes Kevlar fabric to prevent holes from hail. This was not present in the test airframe because of its lower level of manufacturability. The operational MARIA wing skins and horizontal tail will include the Kevlar and are shown in Figure 65. The internal

structure is designed around the C-channel to distribute the load and support skin shape. Like the demonstrator MARIA, the two inner-most ribs extend into the fuselage to be epoxied onto fuselage structure and skin.



Figure 65: Internal Structure in the inboard wing section.

The wing joint connection is shown below, Figure 66. The carbon tube fits in holes in the two most outboard ribs of the inboard wing. They are at different heights to allow the interlocking carbon tube from the outboard section with dihedral. In order to achieve the best fit, the tube will be installed simultaneously with the corresponding outboard tube. The joined MARIA II inboard wing is shown in Figure 67.

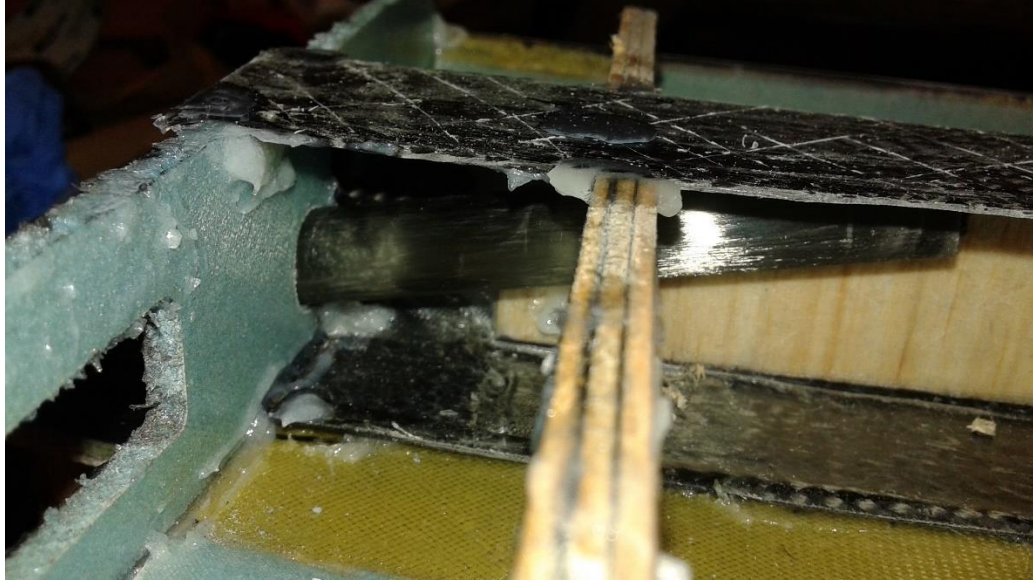


Figure 66: Outboard ribs with cutouts for carbon tube.



Figure 67: Inboard wing demonstration MARIA.

The weight is 27.2 oz, an eight percent increase from the demonstrator MARIA wing. This is expected because of the heavier internal structure. The C-channel in this wing is expected to be capable of sustaining loads approximately 30 percent greater.

CHAPTER VI

TESTING AND RESULTS

6.1 X-Plane Simulation

X-Plane v. 10 was used to evaluate MARIA's stability in high winds and gusts. X-Plane is a flight simulation program capable of accurate flight modeling for manned and unmanned aircraft. It has a robust weather modeling feature and can be used with the operational RC controller or with an autopilot using hardware-in-the-loop. Though not a replacement for actual flight testing, the X-Plane simulations serves to partially verify the aircraft design. Using X-Plane's Plane Maker, an aircraft model was created with the characteristics of the MARIA design, Figure 68. This included control surface sizing, weight and balance information, propulsion characteristics, etc. The detailed model characteristics are in the Appendix.

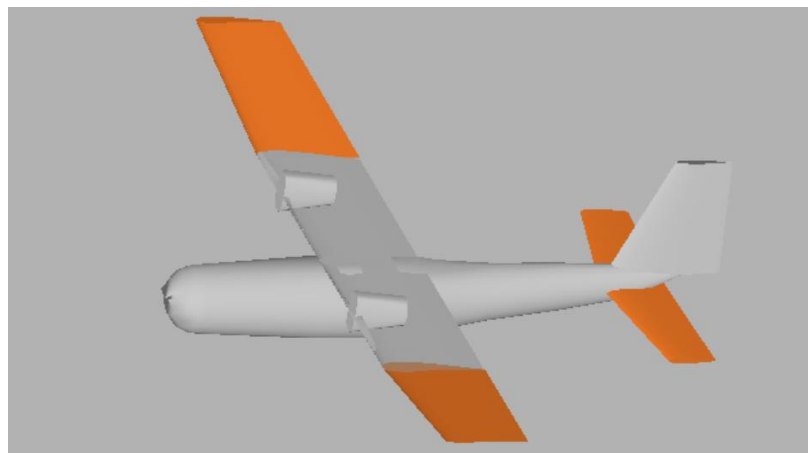


Figure 68: X-Plane model of MARIA aircraft.

In order to check the stability and dynamic response of the aircraft, it was flown in level flight and under basic response tests. The model was flown by Zach Barbeau, with a joystick, rudder pedals, and throttle lever hooked to a computer running X-Plane 10. The phugoid flight mode was excited by a quick nose-up perturbation. Its response is shown with pitch rate of the aircraft, Figure 69. The short period dynamic mode can be excited by X-Plane during flight. Its response is shown in Figure 70. The input from X-Plane occurs between the one and two second mark and the aircraft is damped within the second.

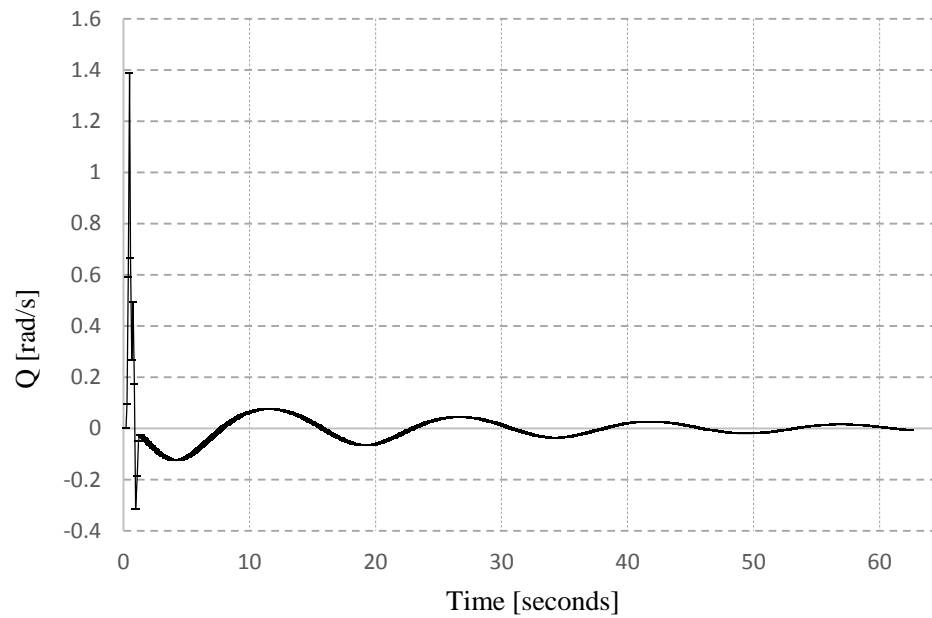


Figure 69: Aircraft phugoid response after perturbation.

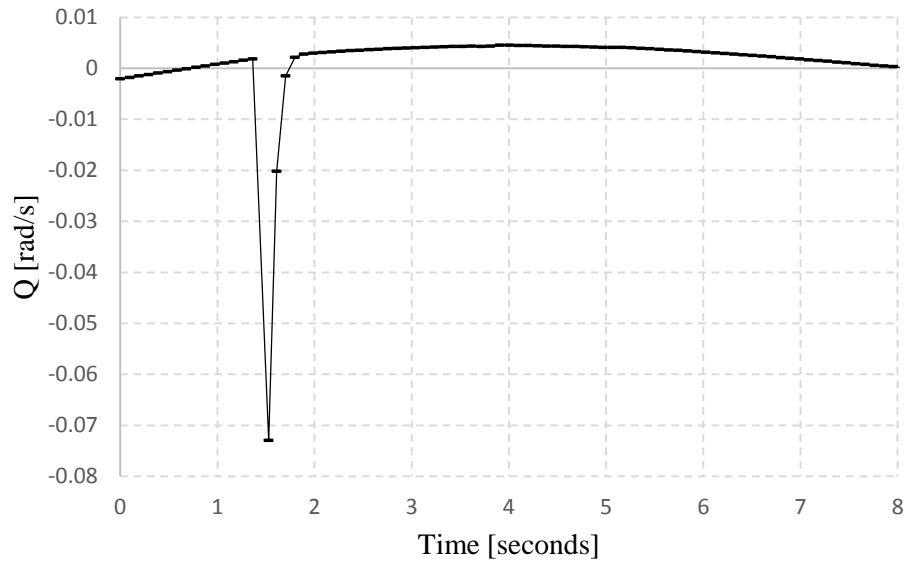
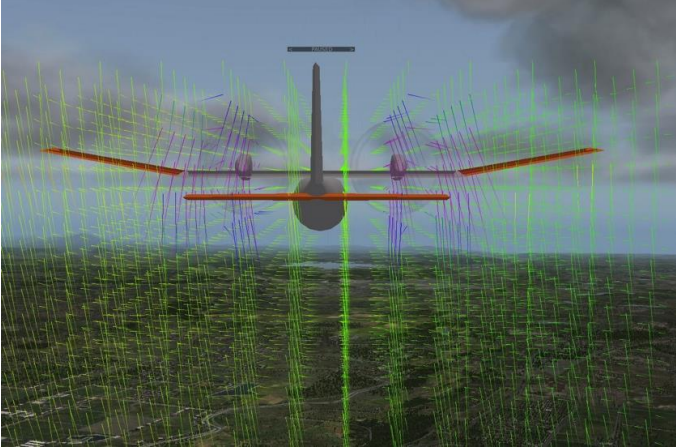
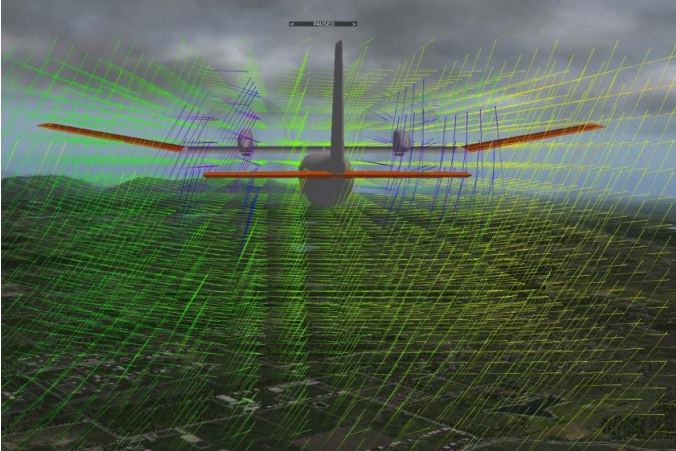
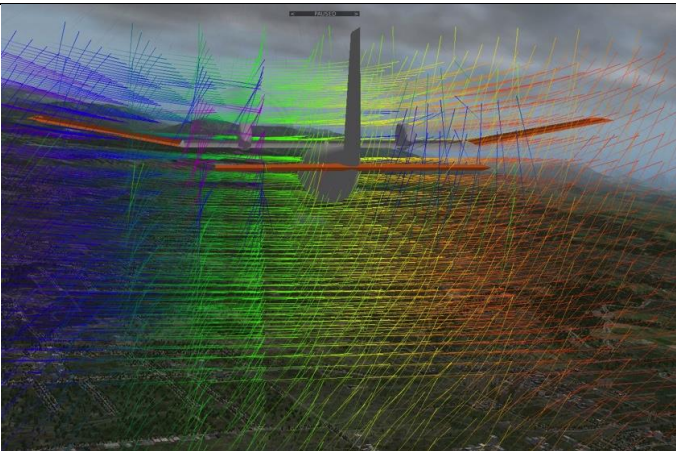


Figure 70: Short period response of MARIA aircraft

The model was also flown in various gust conditions while sustaining speeds close to its cruise speed of 55 kts. Table 17 shows a few of the screenshots of the model being flown in gust conditions of up to 50kt velocity sharp edge gusts. The colored lines in the picture represent the direction and strength of the airflow around the aircraft. The gradient of color corresponds to the velocity with red being the highest

Table 17: Gust response evaluation with X-Plane.

<p>10 kt gusts</p> <ul style="list-style-type: none"> • Remained level without assistance • Relatively easy to control 	
<p>30 kt gusts</p> <ul style="list-style-type: none"> • Required some input for level flight • Controllable 	
<p>50 kt gusts</p> <ul style="list-style-type: none"> • Often required input for level flight • Controllable 	

The parameters used in the model were as close to the expected flight conditions as possible. The results of these tests signify an aircraft stable and controllable in an unstable environment.

6.2 Ground Tests

6.2.1 Taxi Testing

Taxi tests were conducted to determine the behavior of the aircraft on the ground. After initial test, it was obvious that the nose gear needed to be steerable. A control horn was placed on the nose gear shaft and is connected to a servo to generate controlled rotation. The mechanism is photographed in Figure 71.



Figure 71: Nose gear steering mechanism.

After this adjustment, the aircraft taxied controllably and relatively well. It was piloted by OSU's capstone pilot Dan Beirly the extent of the runway and successfully executed turns and straight paths successfully, shown in Figure 72.



Figure 72: The demonstrator MARIA while taxiing.

The aircraft showed some sensitivity in yaw, but not enough to cause immediate concern. The likely cause of this sensitivity is an oversight of the impact of the wing mounted motors in the landing gear design.

The aircraft was at ready for an attempt at take-off, with the motors at full throttle. The aircraft tipped forward and to the side, when it hit a bump in the runway. With the motors producing a large amount of thrust, the landing gear proved too narrow. The vertical cg, with the lightly loaded test aircraft, is approximately three inches below the wing and about six inches below the thrust line. The angles required for tip-over impact to occur are represented in Figure

73

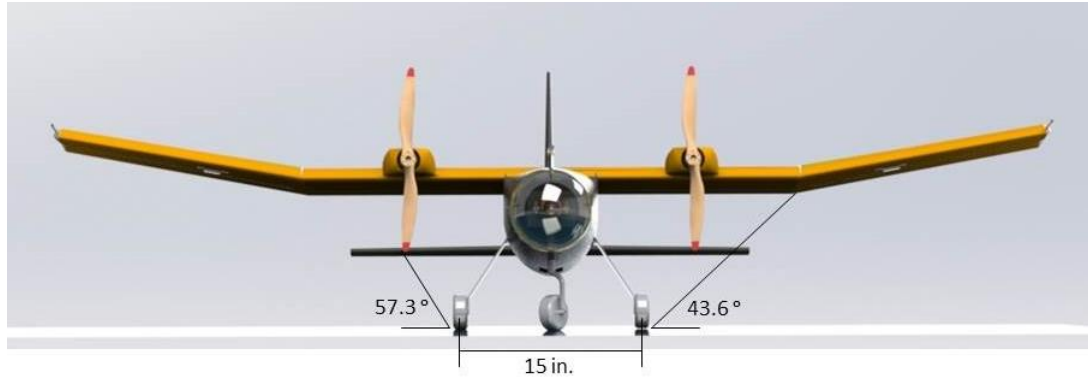


Figure 73: Landing gear installation dimensions

With the landing gear closer to the centerline than the motors, perturbations in ground roll are more likely to cause an upset. The landing gear should be widened and shortened for a successful take-off.

6.2.2 Motor Testing

Static thrust tests were conducted with the propellers: 14x7 and 15x10, and with both 5s and 6s batteries. A Vernier force sensor operated with LabVIEW gave static thrust. The sensor accuracy was verified by simply hanging an object of known weight from the sensor, Figure 74.



Figure 74: Sensor force accuracy check

The aircraft was fixed to the load cell using a strap looped around the empennage and over the tail. The load location on the tail is level with the load sensor to increase accuracy. The setup is shown in Figure 75.



Figure 75: MARIA I set up for static thrust tests

The results of the thrust tests are shown in Table 18. These are with only one motor running, thus the effective thrust for the aircraft would be approximately double.

Table 18: Load cell results

	5s Battery Packs	6s Battery Packs
14x7 Propeller	4.9 lb.	5.6 lb.
15x10 Propeller		7.8 lb.

6.3 Structural Testing

The inboard wing built to the full structural design was tested in bending. The wing was placed between two surfaces supported at each and the width of half the fuselage connection and weights were hung from the center of the wing. The placement schematic is illustrated in Figure 76. The upper case is the wing on the fuselage, loaded as in flight; the lower case is the test plan.

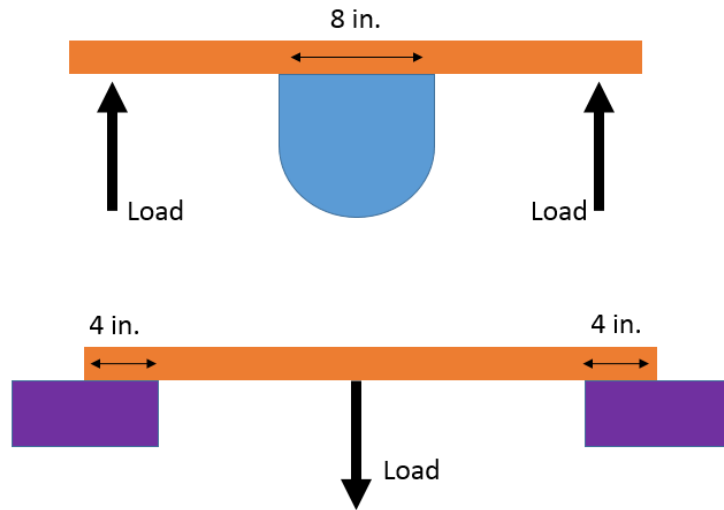


Figure 76: Testing setup for inboard wing.

Straps were tied around the wing to support a steel plate underneath. This plate was used to support the test weights. The straps were placed over inboard ribs in order that the wing would be loaded in bending rather than deform the airfoil from the straps, as is shown in Figure 77.

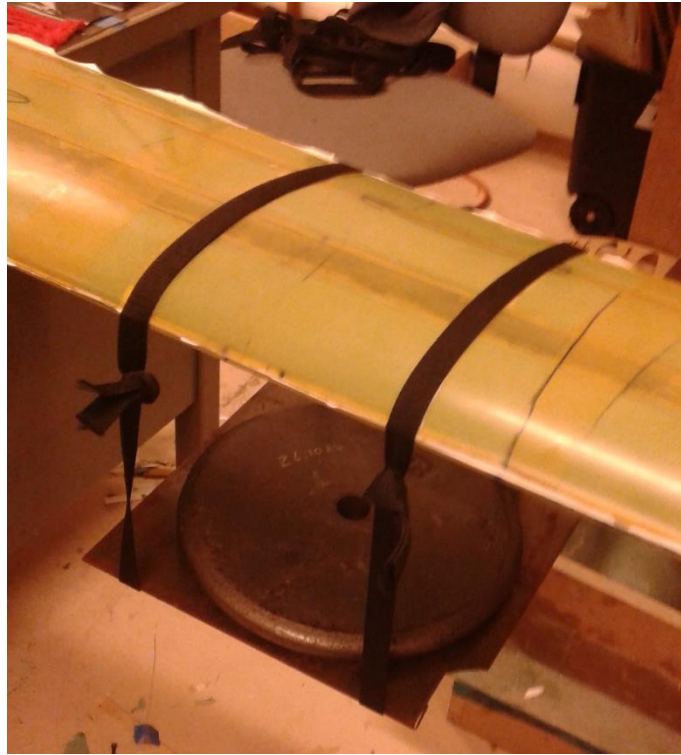


Figure 77: Inboard wing setup for loading.

The plate hung from the wing was slowly loaded with weights. The wing was first loaded with large weights from 20-35lbs. Figure 78 shows the wing under a load of 112lb. Some deflection is noticeable at this stage. It was then loaded in 5-10lb. increments up to a 200lb load shown in Figure 79. At this point some popping noises were heard and a small dent on the upper skin (compression side) appeared.



Figure 78: Inboard wing loaded with 112lb of weight.



Figure 79: Inboard wing loaded with 200lb of weight

After the wing was unloaded, the dent disappeared and the wing appeared to retain structural robustness. It was reloaded to 110 lb. (Figure 81) and no additional popping noises were heard.



Figure 80: Test after initial loading.

The wing is designed to sustain a load of 320 lb. (10g loading). The test load is 62.5% of the design load, with no apparent lasting damage. The wing was not tested to its breaking point because of test set-up limitations.

CHAPTER VII

CONCLUSION

Past and current weather research systems were investigated, with greater detail and effort on meteorological profiling UAS. The operational expectations and goals for a relevant severe storm were researched and finalized. The payload for optimizing data acquisition and the resulting aircraft requirements was designed. The initial aircraft design was executed using benchmarking, and sizing iterations with operational and performance goals. The aircraft for the system was designed in detail to the requirements using the methods discussed in this paper. This includes aerodynamic design, propulsive, and structural design. The aircraft design underwent verification in X-Plane and the aircraft was tested structurally and in ground tests.

A robust and effective research platform was designed and built. The design process was sound and the manufacturing methods are repeatable and produce quality structure. As with any process, there is room for improvement. The major error in this project was manpower organization. The workload for manufacturing was not effectively organized, creating a large time gap between initial manufacturing and the testing stage.

For future work, the airframe will be further tested and integrated into the system for which it was designed. The aircraft will undergo extensive flight testing in order to determine the actual flight envelope and stability characteristics as compared with the envelope predicted in the design and tested in X-Plane. Further structural tests will be undertaken to optimize the structural design of the air vehicle. Manufacturing methods and processes will be corrected for a team of workers and the structure configured for easy internal access. The meteorological sensors will be integrated into the aircraft and tested for operation use.

REFERENCES

- ¹National Weather Service Office of Climate, Weather and Water Services, "NWS Weather Fatality, Injury, and Damage Statistics," <http://www.nws.noaa.gov/om/hazstats.shtml>.
- ²Koch, S." Optimal Observing for Short-Range Prediction of Severe Convective Storms," 18th Conference on Integrated Observing and Assimilation Systems for the Atmosphere, Oceans, and Land Surface (IOAS-AOLS), Atlanta, GA, February 02 - 06, 2014
- ³Elston, J., Argrow, B., Houston, A., Frew, E., "Design and Validation of a System for Targeted Observations of Tornadoic Supercells Using Unmanned Aircraft", Institute for Electrical and Electronics Engineers, Intelligent Robots and Systems, Oct 18, 2010.
- ⁴Schematic diagram of a thunderstorm
- ⁵Brock, F., Crawford, K., "The Oklahoma Mesonet: A Technical Overview," American Meteorological Society, 1995.
- ⁶"NWS Radiosonde Observations-Factsheet," National Weather Service, http://www.erh.noaa.gov/gyx/weather_balloons.htm, 2001
- ⁷Ivey, M., Petty, R., Desilets, D., Verlinde, J., Ellingson, R., "Polar Research with Unmanned Aircraft and Tethered Ballons," U.S. Department of Energy Office of Science 2013
- ⁸"NRL's P-3 Aircraft Support Project to Study Tropical Cyclones," <http://www.nrl.navy.mil/media/news-releases>, 2008
- ⁹Grunbaum, M., "Weather-Studying Warthog: A Fixed-Up A-10 Will Fly Into Thunderstorms," Popular Mechanics, 2011
- ¹⁰Elston, J., Frew, E., "Unmanned Aircraft Guidance for Penetration for Pre-Tornadoic Storms," American Institute of Aeronautics and Astronautics, 2008
- ¹¹Elston, J., Roadman, J., Stachura, M., Argrow, B., "The Tempest Unmanned Aircraft System In Situ Observations of Tornadoic Supercells: Design and Vortex2 Flight Results," Journal of Field Robotics, 2011
- ¹²Houston, A., Argrow, B., "The Collaborative Colorado-Nebraska Unmanned Aircraft System Experiment," American Meteorological Society, 2012
- ¹³Chilson, P., Gleason, A., Zielke, B., "Smartsonde: A Small UAS Platform to Support Radar Research"
- ¹⁴Reuder, J., Brisset, P., Jonassen, M., "The Small Unmanned Meteorological Observer SUMO: A new tool for atmospheric boundary layer research," Meteorologische Zeitschrift, Vol.10 No. 2, pp 141-147, 2009

- ¹⁵Bange, J., Martin, S., Beyrich, F., “Profiling the Lower Troposphere Using the Research UAV M²AV T200 Carolo,” International Symposium on Tropospheric Profiling, The Netherlands, 2009
- ¹⁶“NOAA NOS NMSP Silver Fox & Manta UAS Evaluation Project,” February 2006
- ¹⁷Dias, N. L., Goncalves, J. E., Freire, L. S., Hasegawa, T., Malheiros, A. L., “Obtaining Potential Virtual Temperature Profiles, Entrainment Fluxes, and Spectra from Mini Unmanned Aerial Vehicle Data”, Boundary Layer Meteorology 145:93-111, 2012 .
- ¹⁸Markowski, Paul M., Richardson, Yvette P., “Tornadoogenesis: Our Current Understanding Forecasting Considerations, and Questions to Guide Future Research”, Atmospheric Research 93 3-10, 2009.
- ¹⁹Martin, S., Bange, J., Beyrich, F., “Meteorological Profiling of the Lower Troposphere Using the Research UAV M²AV Carolo”, Atmospheric Measurement Techniques, 4, 705-716, 2011.
- ²⁰Gary England, Meteorologist, October 2, 2013
- ²¹Bonin, T., Goines, D., Scott, A., Wainwright, C., Gibbs, J., Chilson, P., “Measurements of the Temperate Structure-Function Parameters with a Small Unmanned Aerial System Compared with Sodar,” February 2015
- ²²NWS Norman Online Storm Spotter Training, National Weather Service Weather Forecast Office
- ²³“Supercells,” National Oceanic and Atmospheric Administration, <http://www.spc.noaa.gov/misc/AbtDerechos/supercells.htm>
- ²⁴Gundlach, J., :Designing unmanned aircraft systems: a comprehensive approach- 1st ed.”, 1975
- ²⁵Drela, M., “XFOIL: An Analysis and Design System for Low Reynolds Number Airfoils”
- ²⁶Nelson, R., “Flight Stability and Automatic Control,” McGraw-Hill Company, 1998
- ²⁷Hunt, D. “Structural Design and Fabrication Techniques of Composite Unmanned Aerial Vehicles,” Oklahoma State University, 2012

APPENDICES

Airfoil Data

The coordinates of the blended airfoil used for MARIA's wing is shown below. It is blended with the GOE 701 & FX 63 airfoils in XFOIL, "new4."

1.000000	0.000000	0.436246	0.111330
0.995497	0.001627	0.372528	0.113055
0.982302	0.006169	0.341421	0.112801
0.960981	0.013018	0.310990	0.111808
0.932047	0.021704	0.281361	0.110094
0.895923	0.031839	0.252644	0.107694
0.853015	0.042917	0.224961	0.104661
0.804020	0.054655	0.198430	0.101056
0.749824	0.066833	0.173141	0.096908
0.691396	0.078892	0.149225	0.092088
0.629756	0.090072	0.126805	0.086497
0.565950	0.099554	0.106020	0.080191
0.501079	0.106742	0.087000	0.073319

0.069794	0.066060	0.192444	-0.023844
0.054484	0.058479	0.218972	-0.022091
0.041212	0.050356	0.246719	-0.020338
0.029840	0.041893	0.275559	-0.018539
0.020120	0.033631	0.305363	-0.016628
0.011840	0.025431	0.336013	-0.014573
0.005140	0.016808	0.367382	-0.012456
0.001080	0.008754	0.431736	-0.008473
-0.000119	0.002176	0.497275	-0.004988
0.000884	-0.002928	0.562809	-0.001736
0.003577	-0.007268	0.627179	0.000806
0.008212	-0.011597	0.689249	0.002501
0.015078	-0.015972	0.747962	0.003774
0.023962	-0.019877	0.802336	0.004583
0.035106	-0.023047	0.851497	0.004798
0.048557	-0.025407	0.894689	0.004523
0.063998	-0.027124	0.931237	0.003844
0.081253	-0.028061	0.960595	0.002741
0.100311	-0.028042	0.982198	0.001449
0.121066	-0.027567	0.995496	0.000404
0.143402	-0.026752	1.000000	0.000000
0.167223	-0.025487		

Stability Analysis

The spreadsheets used for stability computations are shown in Table 19, Table 20, Table 21, Table 22, Table 23, Table 24, Table 25, Table 26, and Table 27. The stability characteristics used for reference are in Table 28.

Table 19: Static Stability

Σ Moments Wing			Tail Contribution			Fuselage Contribution		
$\Delta := X_{cg_c} - X_{ac_c}$			$\xi_{ww} = \frac{2 \cdot CL_w}{\pi \cdot AR_w}$			$CL_{ot} := \frac{CL_{ot}}{1 + \frac{CL_{ot}}{\pi \cdot AR_t}}$		
$Cm_{cgw} := (CL_{ow} + CL_{\alpha w - \alpha w})(\Delta) + Cm_{acw}$			$\alpha_t := \alpha_w - i_w - \varepsilon + i_t$			$k_2 - k_1$		
			$CL_t := CL_{ot} - \alpha_t$			0.9 lf/d		
Cm_{0w}	-0.13972					wf	0.9375	Cm_{0f}
Δ	-0.02		$d\varepsilon/d\alpha$	0.34968	CL_{at}	if	0	$Cm_{\alpha f}$
$CL_{\alpha w}$	4.74188	per rad	ε_0	2.21589	deg	Δx	5	
$Cm_{\alpha w}$	-0.09484				Cm_{0t}	$deu/d\alpha$	0.65032	
					$Cm_{\alpha t}$			
Cm0	-0.00867	Cmα	-1.384775198	Trim α	-0.35864	XNP/c	0.52203	Static Margin
								0.29203

Table 20: Tail and Elevator Sizing

Resultant Tail Sizing		31			0.00767	-2	0.04734	-(
lt [ft]	2.4375	2.583333			0.00834	-1	0.02384	-(
St req. [ft2]	1.25	180	150		0.00905	0	0.00038	-0.
bt [in]	30	360	30		0.00992	1	-0.02292	-0.
ct [in]	6	72	5	5.5	0.01082	2	-0.04619	-0.
				4.5	0.01187	3	-0.0693	-0.
					0.01296	4	-0.09238	-0.
					0.01414	5	-0.11537	-0.
		2.5			0.0154	6	-0.13829	-0.
					0.01667	7	-0.16118	-0.
					0.01776	8	-0.18426	-(
					0.01904	9	-0.20715	-0.
Longitudinal Control								
$Cm_{\delta e}$	-0.019608				$CL_{\delta e} = \frac{St}{S} \eta CL_{at} \tau$			
δe	20							
$CL_{\delta e}$	0.005384203	per deg.						
Elev./St	0.2							
τ	0.43							
$(1+d\sigma/d\beta)\eta_v$								
Elevator Width	1.2							
	0.218181818							
	0.266666667							

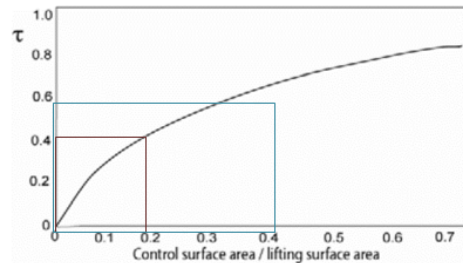


Table 21: Elevator Hinge Calculations

		Che					
Elevator Hinge Moment			δe 0	δe 5	δe -5	δe -10	δe -15
*Cha & Chde from benchmarking	α_w		0	5	-5	-10	-15
Cha	-0.13	-3	0.39	-1.96	2.74	5.09	7.44
Chde	-0.47	-2	0.26	-2.09	2.61	4.96	7.31
		-1	0.13	-2.22	2.48	4.83	7.18
Max Che	7.05	0	0	-2.35	2.35	4.7	7.05
		1	-0.13	-2.48	2.22	4.57	6.92
		2	-0.26	-2.61	2.09	4.44	6.79
		3	-0.39	-2.74	1.96	4.31	6.66
		4	-0.52	-2.87	1.83	4.18	6.53
		5	-0.65	-3	1.7	4.05	6.4
		6	-0.78	-3.13	1.57	3.92	6.27
		7	-0.91	-3.26	1.44	3.79	6.14
		8	-1.04	-3.39	1.31	3.66	6.01
		9	-1.17	-3.52	1.18	3.53	5.88

Table 22: Vertical tail and rudder sizing

Rudder Sizing					
Engine Locations	0.916666667	ft. from centerline			
Thrust Req.	2	lb			
N _{engineout}	1.833333333	lb*ft			
N _{aircraft}					$L_v = \bar{q} S_v C_{L_v}$
					$C_{L_v} = C_{L_{v_0}} + C_{L_{v\beta}} \beta + C_{L_{v\delta_R}} \delta_R$
					$C_n = C_{n_0} + C_{n_\beta} \beta + C_{n_{\delta_A}} \delta_A + C_{n_{\delta_R}} \delta_R$
Set Nv equal to Moment to derive necessary Lv					
Lv	0.752136752	lb			
δr	45	deg			
CL _{δr}	0.002754709	per deg			
Rudder/St	0.3			3.15	
τ	0.55			0.35	
				1.05	
Sv	0.651367025	ft ²			
bv	14	in			
cv	9		3.15	1.08	2.7
cvt	3			0.36	0.9
	0.583333333				
				1.08	
Vv	0.232142857				

Table 23: Dihedral calculations

Roll Stability			
<i>Wing Dihedral</i>			
Dihedral angle [deg]	10		
Portion of planform	0.47		
Velocity [ft/s]	95		
Sideward Vel. [ft/s]	200		
β	2.105263158	kn	0.0004
		kri	1.1
$\Delta\alpha$	9.894736842	Sfs	1.866666667
α	2	lf	4.666666667
		Swet	12.8625
Cl_{β}/Γ	-0.0001	xm/lf	0.267857143
Cl_{β_v}	-0.0078	lt2/Sfs	11.66666667
Cl_{β_r}	-0.1199	Cnbwf	-4.25699E-05
ΔCl_{β_z}	-0.00027		
Cl_{β}	-0.12017		

Table 24: Aileron Sizing

Roll Control			
$(\lambda-1)/(b/2)$	-0.051948052	y1 [in]	21
cr [in]	11	y2 [in]	42
a/a	0.05		
τ	0.18		
c y1	60.13636364	$C_{l_{\delta a}} = \frac{2C_{L_{\alpha_w}}\tau C_r}{Sb} \left[\frac{y^2}{2} + \left(\frac{\lambda-1}{b/2} \right) \frac{y^3}{3} \right] \bigg _{y_1}^{y_2}$	
c y2	-400.9090909		
$Cl_{\delta a}$	-0.1169		
Aileron Area [in2]	44.1		
Width [in]	2.1		
	0.388888889		
	0.318181818		

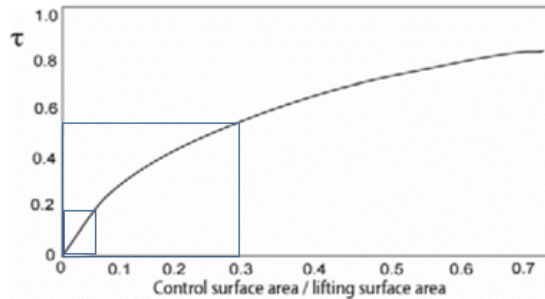


Table 25: Moment resultant of propulsion system

Velocity[ft/s]	90	ρ [slug/ft ³]	0.0023769		Inches Above Wing:	1.5		
Induced Drag C	0.035	Q	117.9239513					
CD		α_w	Mw [lb ft]	Mt	Mf	Mp	Mt	Cmc
0.01520817		-3	-13.90441615	22.25234	-1.76083177	0.740093	7.327183	0.007173
0.018673786		-2	-14.07520832	19.90562	-1.73715284	0.791178	4.884438	0.007668
0.023379369		-1	-14.24600049	17.55891	-1.71347391	0.860541	2.459972	0.00834
0.028327388		0	-14.41679266	15.21219	-1.68979498	0.933477	0.039079	0.009047
0.034443592		1	-14.58758483	12.86547	-1.66611605	1.023633	-2.36459	0.009921
0.040738653		2	-14.758377	10.51876	-1.64243712	1.116425	-4.76563	0.01082
0.048103628		3	-14.92916917	8.172041	-1.6187582	1.224989	-7.1509	0.011872
0.05572375		4	-15.09996133	5.825325	-1.59507927	1.337313	-9.5324	0.012961
0.064004294		5	-15.2707535	3.478609	-1.57140034	1.459372	-11.9042	0.014143
0.07277191		6	-15.44154567	1.131893	-1.54772141	1.588611	-14.2688	0.015396
0.081666715		7	-15.61233784	-1.21482	-1.52404248	1.719725	-16.6315	0.016667
0.089321125		8	-15.78313001	-3.56154	-1.50036355	1.832555	-19.0125	0.01776
0.098289138		9	-15.95392218	-5.90826	-1.47668463	1.964748	-21.3741	0.019041

Table 26: Moment resultant of fuselage

Station	Δx in	w_{fy} in	w_{fx} in	$w_{fy}^2 [\alpha_{ow} + i_f] \Delta x$	x_i/c	$\Delta \epsilon_{\mu}/\Delta \alpha$	$w_{fy}^2 [\Delta \epsilon_{\mu}/\Delta \alpha] \Delta x$
1	6	7.27	7.94	-1585.587	1.167	0.2	63.42348
2	6	8	9.28	-1920	0.667	0.3	115.2
3	6	8.13	10	-1982.907	0.167	0.75	297.4361
4	6	8.13	10	-1982.907	0.333	0.6	237.9488
5	6	7.9	10	-1872.3	0.333		0
6	6	6.41	8.86	-1232.643	0.167	0.013889	3.424008
7	6	6.47	5.51	-1255.827	0.667	0.155556	39.07017
8	6	4.38	4.3	-575.532	1.167	0.311111	35.81088
9	6	2.86	2.03	-245.388	1.667	0.5	24.5388
	54			-12653.091			816.8522
I_f/d_{max}	6	k2_k1	0.5				
C_{m0f}	-0.01638						

Table 27: Aerodynamic Characteristics and Stability Derivatives

Property	Unit	Description	Climb	Cruise	Approach
cbar	ft	mean average chord	0.875	0.875	0.875
b	ft	wingspan	7	7	7
M		mach number	0.0506	0.0888	0.071
CG	%cbar	center of gravity	0.23	0.22	0.2
alpha1	deg	angle of attack	10	2	10
W	lb/ft2	weight	35	35	20
Ixx	slugft2	moment of inertia about x			
CL1	dimensionless	total lift	1.542	0.84	1.542
CD1	dimensionless	total drag	0.26	0.0814	0.26
CTX1	lb	total x-axis thrust	10.34	1.28	0
Cm1	dimensionless	total pitching moment	-1.623	-1.623	-1.623
CmT1	dimensionless	total pitching moment due to thrust	-0.038	-0.022	-0.038
CDo	dimensionless	drag at zero alpha	0.06874	0.03171	0.06874
CDu	dimensionless	drag variation due to speed	0.3768	0.1339	0.1673
CDa	dimensionless	drag variation due to alpha			
CLo	dimensionless	lift at zero alpha	0.993	0.1132	0.993
CLu	dimensionless	lift variation due to speed	0.00257	0.00795	0.00507

CLalpha	dimensionless	lift variation due to alpha	0.102	0.102	0.102
Cmo	dimensionless	pitching moment at zero alpha	-0.2511	-0.2096	-0.2511
Cmu	dimensionless	pitching moment variation due to speed	0.000486947	0.00166	0.00096112
Cmalpha	dimensionless	pitching moment variation due to alpha	-0.0948	-0.0948	-0.0948
Cmadot	dimensionless	pitching moment variation due to alpha rate	-0.00258	0.00258	-0.00258
Cmq	dimensionless	pitching moment variation due to pitch rate	-0.3176	-0.3176	-0.3176
Property	Unit	Description	Climb	Cruise	Approach
CLDe	dimensionless	lift variation due to elevator deflection	0.0053842	0.005384	0.0053842
CmDe	dimensionless	pitching moment variation due to elevator deflection	-0.003069	-0.00307	-0.003069
Clbeta	dimensionless	rolling moment variation due to beta	-0.001175	-0.00118	-0.001175
Clp	dimensionless	rolling moment variation due to roll rate	-0.01615	-0.01615	-0.01615
Clr	dimensionless	rolling moment variation due to yaw rate	0.3852473	0.209675	0.3851751
CYbeta	dimensionless	sideforce variation due to beta	0.0095238	0.012245	0.0122449
CYp	dimensionless	sideforce variation due to roll rate	0.0403913	0.022003	0.0403913

CYr	dimensionless	sideforce variation due to yaw rate	0.0006504	0.00065	0.0006504
Cnbeta	dimensionless	yawing moment due to beta	0.0231717	0.023172	0.0231717
Cnp	dimensionless	yawing moment due to roll rate	-0.19275	-0.105	-0.19275
Cnr	dimensionless	yawing moment due to yaw rate	-0.014509	-0.01451	-0.0145089
ClDa	dimensionless	rolling moment due to aileron deflection	-0.1169	-0.1169	-0.1169
CYDr	dimensionless	sideforce due to rudder deflection	0.0052381	0.005238	0.0052381
CnDa	dimensionless	yawing moment due to aileron deflection	-0.039468	-0.0045	-0.0394678
CnDr	dimensionless	yawing moment due to rudder deflection	-0.012768	-0.01277	-0.0127679

Table 28: Benchmarked Stability Characteristics

Aircraft	State	alpha	CD	CDu	CDdelta	CTXu	CLu	CLdelta	CLdot	CLq	ives			Lateral-Directional Stability Derivatives												
											Cmo	Cmalpha	Cmadot	Cmq	Clbelta	Clb	Clr	Clbelta	Clb	Clr	Clbelta	Clb	Clr	Clbelta	Clb	Clr
Cessna 182	Climb	5.4	0.027	0	0.38	-0.171	0.307	0	4.41	1.7	3.9	0.04	0	-0.65	-5.57	-15.2	-0.0895	-0.487	0.9897	-0.404	-0.145	0.267	0.0907	0	-0.0649	-0.189
	Cruise	0	0.027	0	0.121	-0.096	0.307	0	4.41	1.7	3.9	0.04	0	-0.613	-7.27	-12.4	-0.0923	-0.484	0.0798	-0.393	-0.075	0.214	0.0597	0	-0.0278	-0.0937
	Approach	4	0.0605	0	0.547	-0.396	0.807	0	4.41	1.7	3.9	0.09	0	-0.611	-5.4	-11.4	-0.0969	-0.494	0.2039	-0.303	-0.213	0.201	0.0701	0	-0.096	-0.161
	Climb	5	0.029	0	0.362	-0.162	0.288	0	4.58	4.5	8.8	0.07	0	-0.339	-14.8	-29.2	-0.0923	-0.552	0.1746	-0.61	-0.203	0.356	0.952	0	-0.0615	-0.1561
Cessna 310	Cruise	0	0.029	0	0.16	-0.093	0.288	0	4.58	5.3	9.7	0.07	0	-0.197	-12.7	-26.3	-0.1096	-0.551	0.0729	-0.698	-0.141	0.355	0.444	0	-0.0257	-0.1495
	Approach	6.6	0.0974	0	0.65	-0.513	0.64	0	4.58	4.1	8.4	0.1	0	-0.619	-11.4	-25.1	-0.0965	-0.566	0.2433	-0.577	-0.287	0.355	0.863	0	-0.1021	-0.1947
	SIAl- Approach	8	0.09	0	1.14	-0.45	0.65	0.071	5	3	9	-0.07	0	-0.6	-7	-15.7	-0.14	-0.35	0.56	-0.94	-0.01	0.59	0.16	0	-0.03	-0.31
	Marchetti Cruise 1	0	0.0205	0.05	0.12	-0.05	0.149	0.084	5.5	4.2	10	-0.08	0	-0.24	-9.6	-19.7	-0.11	-0.39	0.28	-1	-0.14	0.61	0.17	0	0.09	-0.26
S-211	Cruise 2	0.9	0.0205	0.05	0.17	-0.055	0.149	0.132	5.5	4.2	10	-0.08	0	-0.24	-9.6	-19.7	-0.11	-0.39	0.31	-1	-0.12	0.62	0.17	0	0.08	-0.26
	Climb	0.7	0.02	0	0.13	-0.05	0.19	0	4.81	1.8	3.7	0.025	0	-0.668	-6.64	-14.3	-0.0951	-0.44	0.059	-0.361	-0.0635	0.314	0.052	0	-0.0154	-0.1433
	Cessna T Cruise	2	0.02	0	0.25	-0.07	0.2	0	5.15	2	4.1	0.025	0	-0.67	-6.95	-14.9	-0.0944	-0.442	0.0926	-0.346	-0.0827	0.3	0.106	0	-0.0243	-0.139
	37A Approach	4.2	0.0689	0	0.682	-0.4	0.81	0	4.64	1.8	3.7	0.1	0	-0.631	-6.84	-14	-0.0922	-0.458	0.254	-0.303	-0.1908	0.263	0.095	0	-0.0788	-0.153
Beech 99	Approach	3.5	0.0969	0	0.933	-0.324	0.76	0.027	6.24	2.7	8.1	0.1	0	-2.08	-9.1	-34	-0.13	-0.5	0.06	-0.59	-0.21	0.39	0.12	0	-0.005	-0.204
	Cruise (low)	0	0.027	0	0.131	-0.0596	0.201	0.02	5.48	2.5	8.1	0.05	0	-1.89	-9.1	-34	-0.13	-0.5	0.14	-0.59	-0.19	0.39	0.08	0	0.019	-0.197
	Cruise (high)	11	0.027	0	0.131	-0.0596	0.201	0.02	5.48	2.5	8.1	0.05	0	-1.89	-9.1	-34	-0.13	-0.5	0.14	-0.59	-0.19	0.39	0.08	0	0.019	-0.197
	Climb	5	0.0408	0	0.527	-0.255	0.43	0	5.38	3.3	8	0.06	0	-1.06	-10.3	-24.7	-0.108	-0.57	0.2176	-0.886	-0.315	0.448	0.848	0	-0.0924	-0.208
Cessna 620	Cruise	0	0.0322	0	0.269	-0.126	0.48	0	5.95	2.7	7.5	0.06	0	-1.18	-8.17	-22.4	-0.1381	-0.566	0.166	-0.883	-0.227	0.448	0.1739	0	-0.0501	-0.2
	Approach	6	0.0628	0	0.475	-0.342	0.48	0	5.38	2.7	7.6	0.09	0	-1	-8.68	-22.8	-0.1172	-0.576	0.2307	-0.907	-0.343	0.447	0.871	0	-0.1026	-0.224
	Approach	5	0.0431	0	1.06	-0.6	1.2	0.04	5.04	1.6	4.1	0.047	-0.01	-0.66	-5	-13.5	-0.173	-0.39	0.45	-0.73	0	0.4	0.15	0	-0.13	-0.26
	Cruise (max wht)	2.7	0.0216	0.04	0.3	-0.07	0.13	0.4	5.84	2.2	4.7	0.05	0.05	-0.64	-6.7	-15.5	-0.11	-0.45	0.16	-0.73	0	0.4	0.127	0	-0.008	-0.2
Learjet 24	Cruise (low wht)	1.5	0.0216	0.04	0.22	-0.07	0.13	0.28	5.84	2.2	4.7	0.05	0.07	-0.64	-6.7	-15.5	-0.1	-0.45	0.14	-0.73	0	0.4	0.124	0	-0.022	-0.2
	Cruise (high wht)	10	0.189	0	0.455	-0.5	0.24	0	3.44	0.66	2.3	0.03	0	-0.644	-1.64	-5.84	-0.175	-0.285	0.265	-1.18	0	0	0.507	0	-0.144	-0.753
	Approach	2	0.048	-0.06	0.384	-0.13	0.22	-0.2	2.005	0.82	1.9	-0.028	0	-1.308	-2.05	-4.83	-0.093	-0.272	0.754	-1.045	0	0	0.242	0	-0.093	-0.649
	Cruise	11.7	0.0269	0	0.595	-0.45	0.43	0	2.8	0.63	1.33	0.02	0	-0.098	-0.95	-2	-0.156	-0.272	0.205	-0.695	0	0	0.199	0	0.013	-0.32
McDonnell F-4	Cruise (Mk1)	2.6	0.0205	0.027	0.3	-0.064	0.1	0.27	3.75	0.86	1.8	0.025	-0.12	-0.4	-1.3	-2.7	-0.08	-0.24	0.07	-0.68	0	0	0.125	0	-0.036	-0.27
	Cruise (Mk1)	3.3	0.0439	-0.054	0.4	-0.1	0.01	-0.18	2.8	0.17	1.3	-0.025	0.054	-0.78	-0.25	-2	-0.025	-0.2	0.04	-0.7	0	0	0.09	0	0	-0.26
	Approach	8.5	0.0751	0	1.13	-0.5523	0.92	-0.22	5.67	6.7	5.65	0	0.071	-1.45	-3.3	-21.4	-0.281	-0.502	0.95	-1.08	0	0	0.184	0	-0.222	-0.36
	Cruise (low)	2.5	0.0164	0	0.2	-0.055	0.21	0.13	4.4	7	6.6	0	0.013	-1	-4	-20.5	-0.16	-0.34	0.13	-0.9	0	0	0.16	0	-0.026	-0.28
Boeing 747-200	Cruise (high)	2.4	0.0305	0.22	0.5	-0.95	0.29	-0.23	5.5	8	7.8	0	-0.09	-1.6	-9	-25.5	-0.095	-0.32	0.2	-0.9	0	0	0.21	0	0.02	-0.33

Structural Analysis

The spreadsheet calculations for the aircraft structural loads are represented in Table 29, Table 30, and Table 31. The wing structure calculations are shown in Table 32, Table 33, and Table 34. Figure 81 gives the subroutine for torsional shear used with the spreadsheet calculations and spar bending calculations is in Table 35. The calculations for the fuselage torsional and bending loads are in Table 36.

Table 29: Load Estimations

	TO	Empty			TO	Cruise			Bank	Pull-out
Weight[lb]	35	18		CL	1.5	0.52		Radius [ft]	100	60
CG [in. aft]	16.98	17.42		Lift [lb]	36.38	35.51		tan(Θ)	1.436025	
TO Angle	14	deg		Tail [lb]	5.57	-0.21		Θ	0.962513	
S[ft ²]	6.125			G loading	1.48	1.29		G loading	1.749905	1.828157
St[ft ²]	1.041667									

Table 30: Gust load calculations

Gusts	TO	Empty	
u_{gust} [mph]	80		$n = 1 + \frac{\frac{1}{2}\rho V(\partial C_L / \partial \alpha)u}{w}$
Cl_α [per rad]	4.55153		
w	5.71	2.94	
G loading	5.28	14.78	

Table 31: Aerodynamic surface moments

Moments Via Tail			
Horizontal:		Vertical:	
Area [in2]	150	Area [in2]	72
Max Lift Coeff.	1	Max Lift Coeff.	1.3
P [lb]	16.49935	P [lb]	7.9196875
Moment [lb ft]	49.5	Moment [lb ft]	23.76
	8.249675		55.437813
Moment Via Wing		Moment Via Engine	
Area [in2]	420	Thrust [lb]	8
c [in]	10	Arm [in]	2
Max Mom Coeff.	0.13	Moment [lb ft]	1.3333333
Moment [lb ft]	5.004803		
Outboard			
	11.68745419	44.3875	
	53.265		

Table 32: Wing structure idealization

Wing Structure Estimations						
	Thickness[in.]	Weight [oz/sq.yd]	G [psi]	τ max [psi]	Airfoil:	
Fiberglass	0.005	3	1595000	13000	RootCord	11 in
Balsa Skin	0.125		23500		TipCord	11 in
Balsa Spar	0.125	0.049	23500	1300	Max. Th.	13 %
Carbon Fiber	0.007	3.5	4786000	15900	@ x=	0.3 %
Uni-CarbonFiber	0.006	4.3	725200	13000	C_L	0.045
Kevlar	0.004	1.7	10200000	7250	Chord	11 in
Skin	0.03058	4.7	0.014824	5199.477	G Loading	5
Front Spar	0.05753	13.147	0.0220413	14602.82	Weight	560 oz.
Aft. Spar	0.04885	10.049	0.01984099		Span	34 in
	0.038764075		0.399			
					Torsional Load	380.2882
	Gref:	1595000				

Table 33: Structure material characteristics

	Th (wrt G)	Weight [oz/sq.yd]	Density psi	Th
Skin	0.03058	4.7	0.014824	0.009
Front Spar	0.05753	13.147	0.0220413	0.399
Aft. Spar	0.04885	10.049	0.01984099	0.144

Table 34: Wing structure torsion results

	d Θ /dz	q1	q2	q3				Weight	Fabric Only	W/Epoxy
Cell I	-12536700	259.08	-26.25	0	0	q1 [lb/in]	28.93324	Skin [oz]	3.344833333	6.689667
Cell II	-16683700	-26.25	329.38	-13.72	0	q2 [lb/in]	29.78955	Front Spar [oz]	0.64335088	1.286702
Cell III	-2871000	0	-13.72	209.6	0	q3 [lb/in]	9.227603	Aft. Spar [oz]	0.218193565	0.436387
Torsion	0	1.8	10.46	1.8	380.28815	d Θ /dz	0.000535	Spar Cap [oz]	0.836111111	1.672222
								Total [oz]		10.08498
	-12536700	268.73999	-35.91	0	0					
	0	-393.54617	386.328644	-13.22	0				0.399	
	0	0	-65.411156	211.1674	0					
	0	0	0	41.21202	380.28815					

```

Sub torsion()
'to solve for shear resulting from torsion

Dim torsion As Single
Dim M(5, 4) As Single
Dim i As Integer
Dim j As Integer
Dim k As Integer
Dim n As Integer
Dim temp(5) As Single
Dim mult As Double

For j = 1 To 4
    For i = 1 To 5
        M(i, j) = Sheet2.Cells(27 + j, 1 + i)
    Next i
Next j

i = 1
For i = 1 To 3
    n = 4 - i
    For k = 1 To n
        mult = M(i, i + k) / M(i, i)
        For j = i To 5
            temp(j) = M(j, i) * mult
            M(j, i + k) = M(j, i + k) - temp(j)
        Next j
    Next k
Next i

For j = 1 To 4
    For i = 1 To 5
        Sheet2.Cells(35 + j, 1 + i) = M(i, j)
    Next i
Next j

End Sub

```

Figure 81: Torsion calculation subroutine, wing

Table 35: Spar bending calculations

Sy [lb]	35			Thickness[in]	Weight [oz/sq.yd]	G [psi]	Ult. Compression [psi]
l [ft]	1.75		Uni-CarbonFiber	0.006	4.3	725200	36000
Mx [lbft]	584.76						
	# Layers	Width [in]	Spar Cap Areas [in ²]			Carbon Rods Properties	
Upper	3	1	0.018	0.018		Tensile Strength	320 ksi / 3.10 GPa
Lower	3	1	0.018			Tensile Modulus	19.5 msi / 134 GPa
						Compressive Strength	270 ksi / 1.90 GPa
						Compressive Modulus	19.0 msi / 131 GPa
h(inboard)	1.287 in			$\delta y_1 / \delta z$		0	
y(above center)	0 in			$\delta y_2 / \delta z$		0	
Ixx [in ⁴]	0.401623						
σ_z [psi]	11243.17		Outboard Rod				
P1 [lb]	202.377		σ_z [psi]	149983.5755	Do[in]	0.394	
P2 [lb]	202.377		P1[lb]	53.265	Di[in]	0.315	
Sy [lb]	-35		c	0.197			
q12 [lb/in]	-109.269		I[in ⁴]	0.000699624			
			I[in]	10			
SF	3.202						
				224.9753633			

Table 36: Fuselage torsion and bending calculations

Fuse Structure Estimations			Gref [psi]										
	Thickness[in.]	Weight [oz/sq.yd]	G [psi]										
Fiberglass	0.005	3	1595000										
Carbon Fi	0.007	3.5	4786000							q s,0	-1.98405	lb/in	
Kevlar	0.004	1.7	1E+07										
										Stringer			
										Area:	0.1	in ^2	
Skin	0.015	9	1595000							σ_1/σ_2 :	1		
Skin adj.	0.015									Yb [in]	2.76634		
										Ixx [in4]	3.49627		
Surface A	106.94	in ²	98.19										
										Mx [lb ft]	495		
	Fabric	Total								Sy [lb]	350	at	
Weight	2.227916667	4.455833											
	2.045625	4.09125											
Boom #	x loc.	y _i loc.	A _B	A _B *y _b ²	σ_z (psi)	q _b (lb/in	A _{ab} [in ²]	Aa _{ab} *q _b	q _s [lb/in]	τ (psi)			
1	0	0	0.03	0.23	4699.31	-8.307	4	-33.2274	-10.2909	-686.06			
2	2	0	0.03	0.23	4699.31	-16.61	4	-66.4548	-18.5978	-1239.851			
3	4	0	0.03	0.23	4699.31	-24.92	4	-99.6822	-26.9046	-1793.641			
4	4	2	0.13	0.076	1301.4	-34.89	4	-139.557	-36.8732	-2458.216			
5	4	4	0.03856	0.059	-2096.51	-30.13	6.2832	-189.284	-32.1096	-2140.641			
6	1.414213562	5.656854	0.04712	0.394	-4911.67	-16.49	6.2832	-103.594	-18.4716	-1231.438			
7	0	8	0.04712	1.291	-8892.32	8.2034	6.2832	51.5438	6.21939	414.626			
8	1.414213562	5.656854	0.04712	0.394	-4911.67	21.841	6.2832	137.234	19.8574	1323.83			
9	4	4	0.03856	0.059	-2096.51	26.605	4	106.42	24.6211	1641.404			
10	4	2	0.13	0.076	1301.4	16.636	4	66.546	14.6524	976.829			
11	4	0	0.03	0.23	4699.31	8.3296	4	33.3186	6.34559	423.039			
12	2	0	0.03	0.23	4699.31	0.0228	4	0.09116	-1.96126	-130.751			
				SF	9.28891			SF	2.9492933				

Drag Analysis

The drag build up calculations are

Table 37: Drag Build-Up

p [slug/ft^3]	0.0023769 M	0.16874
μ[slug/ft.s]	3.7373E-07 W [lb]	35
*Sea level for max. drag		
Parasite drag		
Component	Drag Coeff.	Skin Friction
Skin Friction	0.00879672	Fuse
TAMDAR	0.0051	Horizontal
Flap	0.01725	Dome
L&P	0.00311467	Wing
Engines	0.003	Vertical
Cd0	0.0372614	Engines
		Wing, Tail, Strut, and Pylon:
Induced Drag Cd	0.1	
Total	0.1373	0.2073
Drag	5.89058808 lbs	
Thrust:		
Climb	14.949 lb	
Cruise	5.891 lb	
Approach	0 lb	

Solidworks FEA

The characteristics for the FEA study of the inboard wing are represented in Figure 82, Table 38, and Table 39. The characteristics for the FEA study of the fuselage are in Figure 83, Table 40, and Table 41

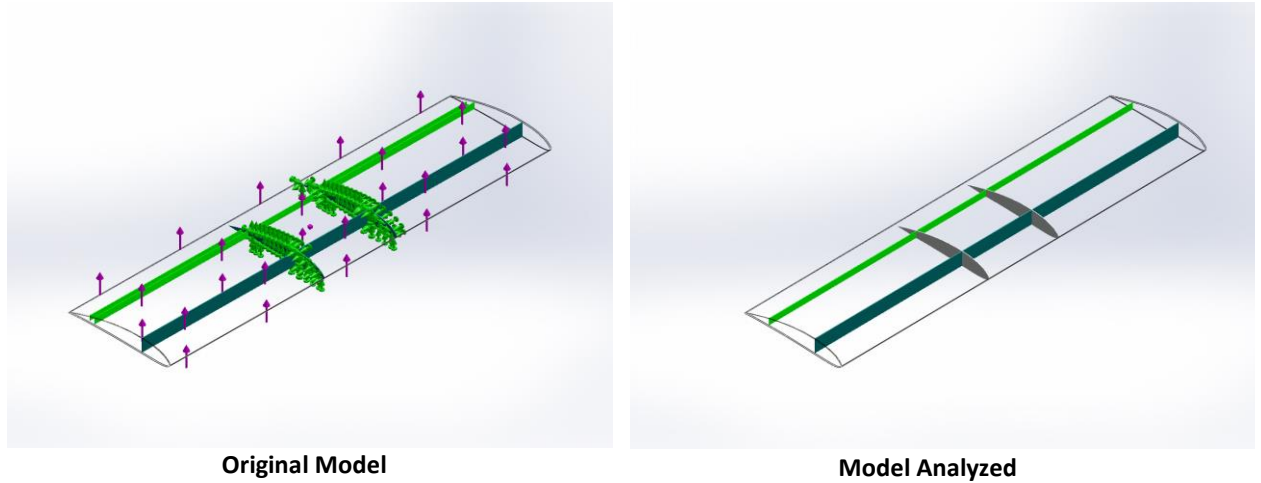


Figure 82: Inboard wing model for Solidworks FEA

Table 38: Inboard wing Solidworks FEA settings

Study name	Study 2
Analysis type	Static
Mesh type	Mixed Mesh
Thermal Effect:	On
Thermal option	Include temperature loads
Zero strain temperature	298 Kelvin
Include fluid pressure effects from SolidWorks Flow Simulation	Off
Solver type	FFEPlus
Inplane Effect:	Off
Soft Spring:	Off
Inertial Relief:	Off
Incompatible bonding options	Automatic
Large displacement	Off
Compute free body forces	On
Friction	Off
Use Adaptive Method:	Off
Result folder	SolidWorks document (C:\CAD\CAD)

Table 39: Tabulated resultant forces for FEA analysis, Inboard wing

Components	X	Y	Z	Resultant
Reaction force(lbf)	-7.0619	-41.7955	-16.0156	45.3126
Reaction Moment(lbf·in)	0	0	0	8.85075e-033

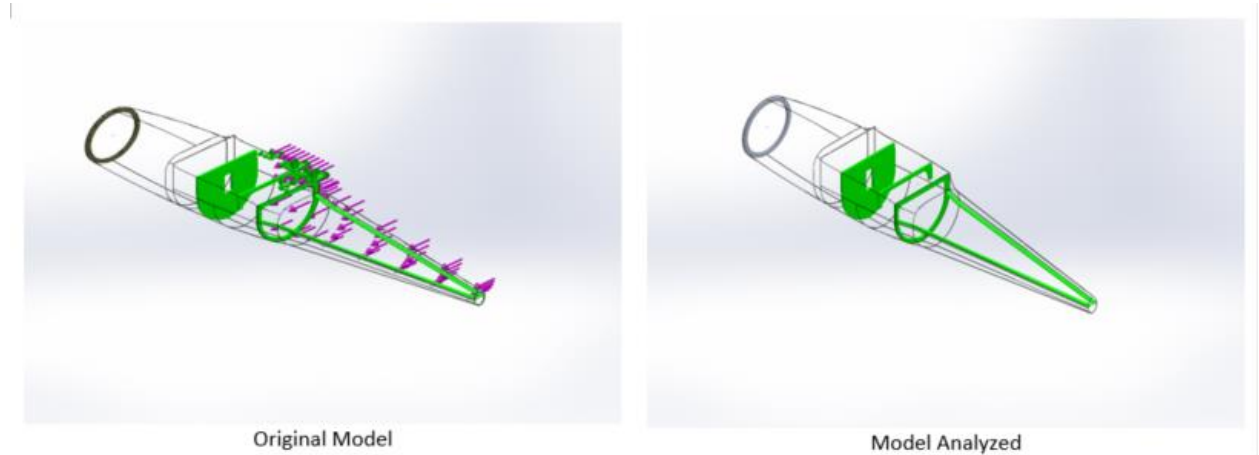


Figure 83: Fuselage model for Solidworks FEA

Table 40: Fuselage Solidworks FEA settings

Study name	Study 1
Analysis type	Static
Mesh type	Mixed Mesh
Thermal Effect:	On
Thermal option	Include temperature loads
Zero strain temperature	77 Fahrenheit
Include fluid pressure effects from SolidWorks Flow Simulation	Off
Solver type	FFEPlus
Inplane Effect:	Off
Soft Spring:	Off
Inertial Relief:	Off
Incompatible bonding options	Automatic
Large displacement	Off
Compute free body forces	On
Friction	Off
Use Adaptive Method:	Off
Result folder	SolidWorks document (C:\CAD\CAD)

Table 41: Tabulated resultant forces for FEA analysis, fuselage

Components	X	Y	Z	Resultant
Reaction force(lbf)	-1.83421	-2.25541	-0.322931	2.92498
Reaction Moment(lbf-in)	-11.5102	-26.325	-1.04498	28.7503

X-Plane Model Characteristics

The following figures describe the X-Plane model built in X-Plane Plane Maker to mimic MARIA's performance.

The screenshot displays the 'Engines' configuration window in X-Plane, showing various engine specifications for a propeller engine. The window is divided into several sections:

- GENERAL ENGINE SPECS:**
 - critical altitude: 30000 (max altitude at which full power available at zero speed)
 - ☒ FADEC automatically keeps engines from exceeding max allowable power or thrust
 - throttle available at max lever, one engine failed: 0.90 (throttle)
 - throttle available at max lever, all engines running: 0.90 (throttle)
 - hi idle fuel adjustment ratio to default: 0.80 (fuel ratio)
 - lo idle fuel adjustment ratio to default: 0.80 (fuel ratio)
 - go to 50% afterburner above this throttle lever position: 0.00
 - go to BETA PITCH below this throttle lever position: 0.00 ☐ beta available
 - go to REVERSE below this throttle lever position: 0.00 ☐ reverse available
 - throttle available at max reverse lever position: 0.00 (throttle)
 - ☐ auto-set RPM and throttle based on power lever
- PROP ENGINE SPECS:**
 - maximum power: 0000250 (hp)
 - feathered pitch of prop, blue knob pulled aft: 0.00 (deg)
 - redline: 09000 (engine RPM)
 - RAM-inlet pressure recovery: 0.01 (fraction)
 - coarse pitch of prop, governor in alpha mode: 0.00 (deg)
 - top of green arc: 07500 (engine RPM)
 - fine pitch of prop, governor in alpha mode: 0.00 (deg)
 - bottom of green arc: 01000 (engine RPM)
 - beta pitch of prop, black knob at idle: 0.00 (deg)
 - minimum prop governor RPM: 00000 (engine RPM)
 - reverse pitch of prop, black knob full aft: 0.00 (deg)
 - idle: 01700 (engine RPM)
 - prop mass ratio to solid aluminum: 0.10
 - tip weights on ROTORS, pounds, each: 000
 - tip mach at 50% power (for constant-mach props): 0.00
 - tip mach at 100% power (for constant-mach props): 0.00
- JET ENGINE SPECS:**
 - maximum allowable thrust: 0000000 (lb)
 - compressor area: 00000 (square feet)
 - fan RPM at 100% N1: 000000 (rpm)
 - afterburner thrust inc: 0000000 (lb)
- ROCKET ENGINE SPECS at sea level, optimum altitude, and vacuum:**
 - thrust: 0000000.00 (lb)
 - optimum altitude: 000000 (feet)
 - nozzle exit area: 00000 (square feet)
 - SFC: 0997 (/hr)

Figure 84: XPLANE Engine Specs

Engines

Description Location Transmission Spoolup/Boost SFC/Sound Prop Geo Jet Curves

GENERAL ENGINE SPECS

engn 2 carb recip carb recip

prop 2 fixed fixed

number blades 0 2 CCW 0 2 CW

ENGINE clutched
PROP clutched
PROP ducted

long arm - 0 0 0.2 7 (ft)

lat arm 0 0 1.0 0 (ft)

vert arm 0 0 1.1 0 (ft)

vert cant 0 0 0.0 (deg)

side cant 0 0 0.0 (deg)

prop radius (ft) 0 0 0.6 6 vectors

root and tip chord 0 1.0 0 0.5 (inches)

fine and coarse pitch 0 0.0 0 0.0 (deg)

design propeller RPM 0 4,0 0 0 (RPM)

design airspeed thru prop disc 0 8 0 (kt)

engine 0 1.0 0 0 gear ratio

Figure 85: XPLANE Engine Specs

Engines

Description Location Transmission Spoolup/Boost SFC/Sound Prop Geo Jet Curves

transmission losses 0.0 0 6 (part)

number of transmissions 2 (#)

engine #1 drives transmission # 1 this engine free-wheels

prop #1 is driven by transmission # 1

engine #2 drives transmission # 2 this engine free-wheels

prop #2 is driven by transmission # 2

Figure 86: XPLANE Engine power transmission

Engines

Description

Location

Transmission

Spoolup/Boost

SFC/Sound

Prop Geo

Jet Curves

RECIPROCATING OR TURBOPROP SPECIFIC FUEL CONSUMPTION

lo altitude for prop engines

0 0 0 0 0 (ft)

lo altitude half power SFC

0 0 4 4 0 (/hr)

lo altitude max power SFC

0 0 7 4 0 (/hr)

hi altitude for prop engines

1 0 0 0 0 (ft)

hi altitude half power SFC

0 0 4 4 0 (/hr)

hi altitude max power SFC

0 0 4 4 0 (/hr)

idle FF

0.1 0 (ratio to max)

JET ENGINE SPECIFIC FUEL CONSUMPTION

lo altitude for jet engines

0 0 0 0 0 (ft)

lo altitude half thrust SFC

0 0 5 5 0 (/hr)

lo altitude max thrust SFC

0 0 5 5 0 (/hr)

hi altitude for jet engines

0 0 0 0 0 (ft)

hi altitude half thrust SFC

0 0 5 5 0 (/hr)

hi altitude max thrust SFC

0 0 5 5 0 (/hr)

idle FF

0.1 0 (ratio to max)

SOLAR-POWER

solar cell wing coverage

0.0 0 (fraction of total)

solar cell efficiency

0.0 0 (fraction of perfect)

speed that wind sound was recorded at

2 0 0 (KIAS, used for setting the sounds in X-Plane)

rpm that the propeller sound was recorded at

0 2 5 0 0 (rpm, used for setting the sounds in X-Plane)

rpm that the recip-engine sound was recorded at

0 2 5 0 0 (rpm, used for setting the sounds in X-Plane)

N1 that the jet or turboprop engine sound was recorded at

1 0 0 0 0 (N1, used for setting the sounds in X-Plane)

engine number to set

1 #

exhaust offset long arm

0 0 0 0 0 (ft, relative to the engine location)

exhaust offset lat arm

0 0 0 0 0 (ft, relative to the engine location)

exhaust offset vert arm

0 0 0 0 0 (ft, relative to the engine location)

exhaust dirtiness

1.0 0 (ratio to default)

Figure 87: XPLANE Engine SFC information

The screenshot shows the 'Engines' window with the 'Prop Geo' tab selected. The window displays 12 engines in a grid. The parameters are as follows:

	1	2	3	4	5	6	7	8	9	10	11	12
L.E. offset	0.020	0.000	0.000	0.000	0.000	0.000	0.000	0.000	0.000	0.000	0.000	0.000
T.E. offset	0.000	0.000	0.000	0.000	0.000	0.000	0.000	0.000	0.000	0.000	0.000	0.000
incidence	8.415	7.293	6.289	5.437	4.734	4.161	3.692	3.307	2.988	2.721		
chord	0.097	0.093	0.088	0.083	0.078	0.073	0.068	0.063	0.058	0.053		
Mach	0.325	0.326	0.327	0.329	0.331	0.334	0.337	0.341	0.345	0.349		
aoa	-0.467	-1.356	-2.126	-2.747	-3.222	-3.570	-3.817	-3.985	-4.093	-4.153		

On the right side, there are four engine test speed indicators:

- test speed through disc: 200 (kt)
- test speed of prop: 2000 (rpm)
- test alt of airplane: 20000 (ft)
- test alt of engine: 20000 (ft)

Figure 88: XPLANE propeller geometry

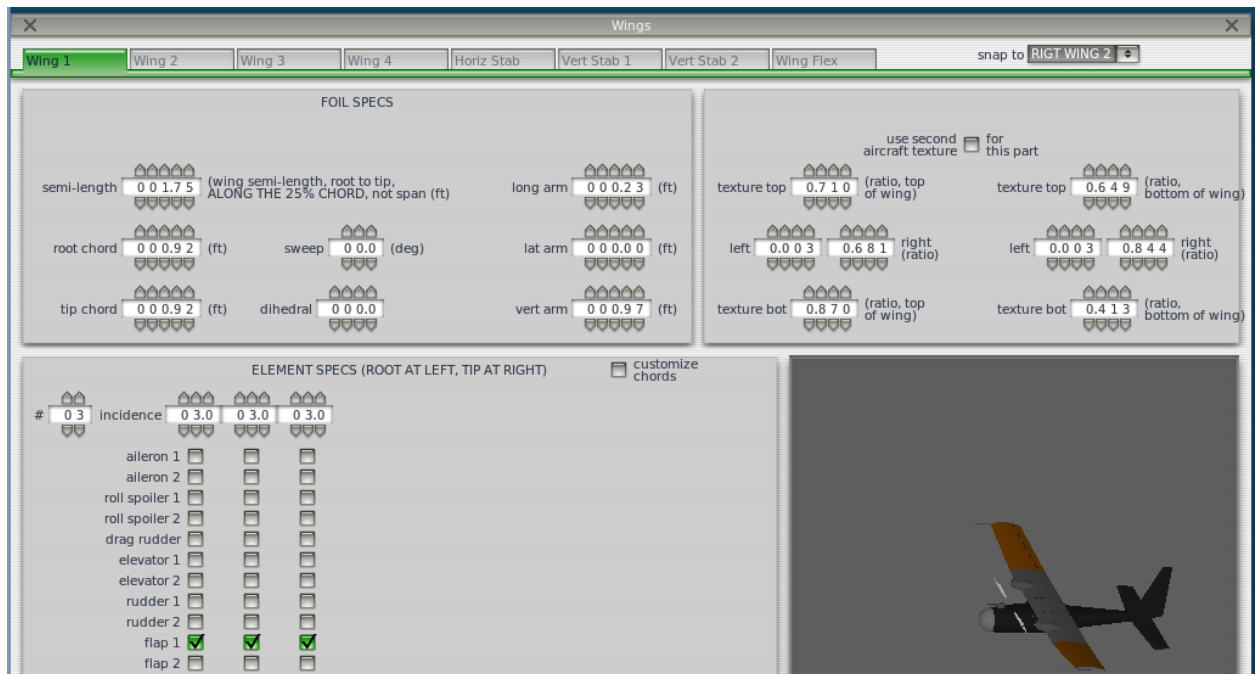


Figure 89: XPLANE wing specifications

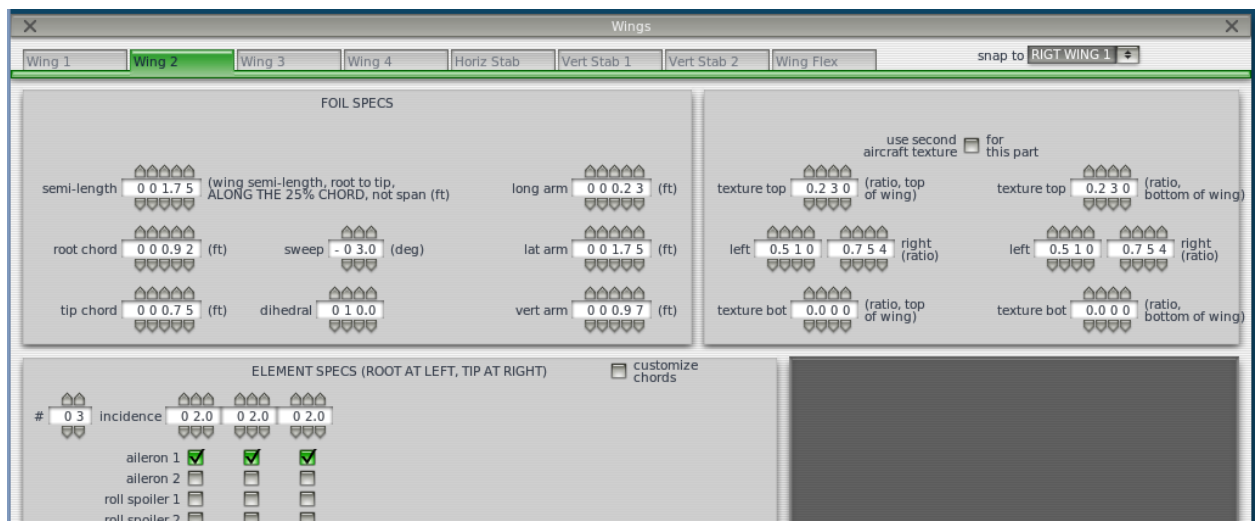


Figure 90: XPLANE outboard wing specifications

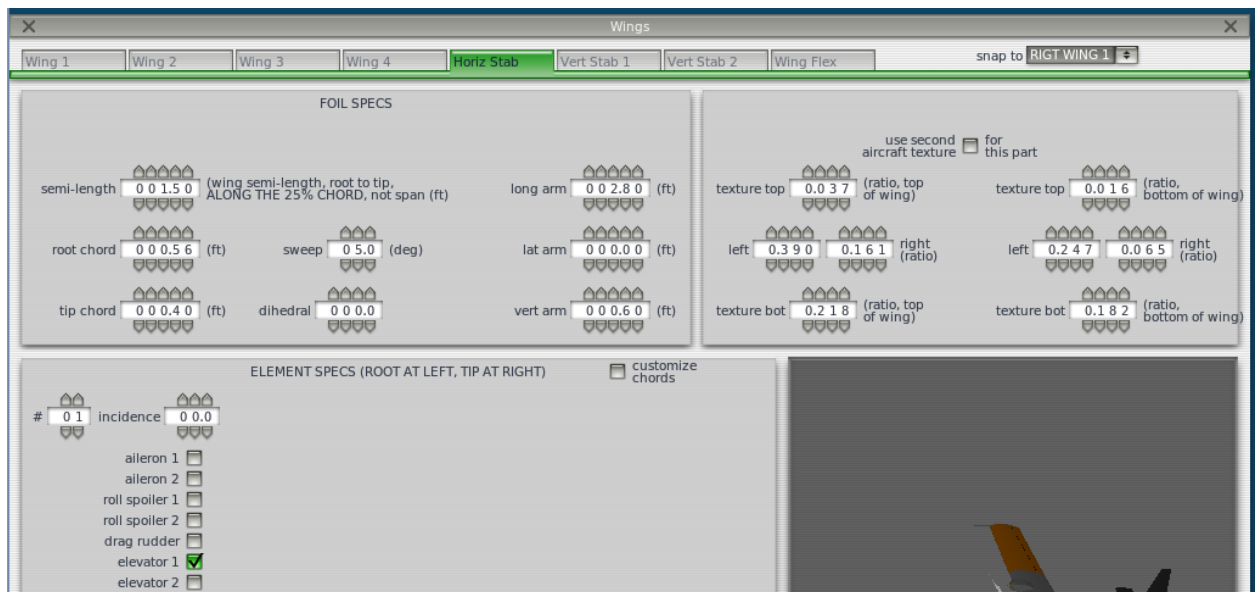


Figure 91: XPLANE horizontal tail specifications

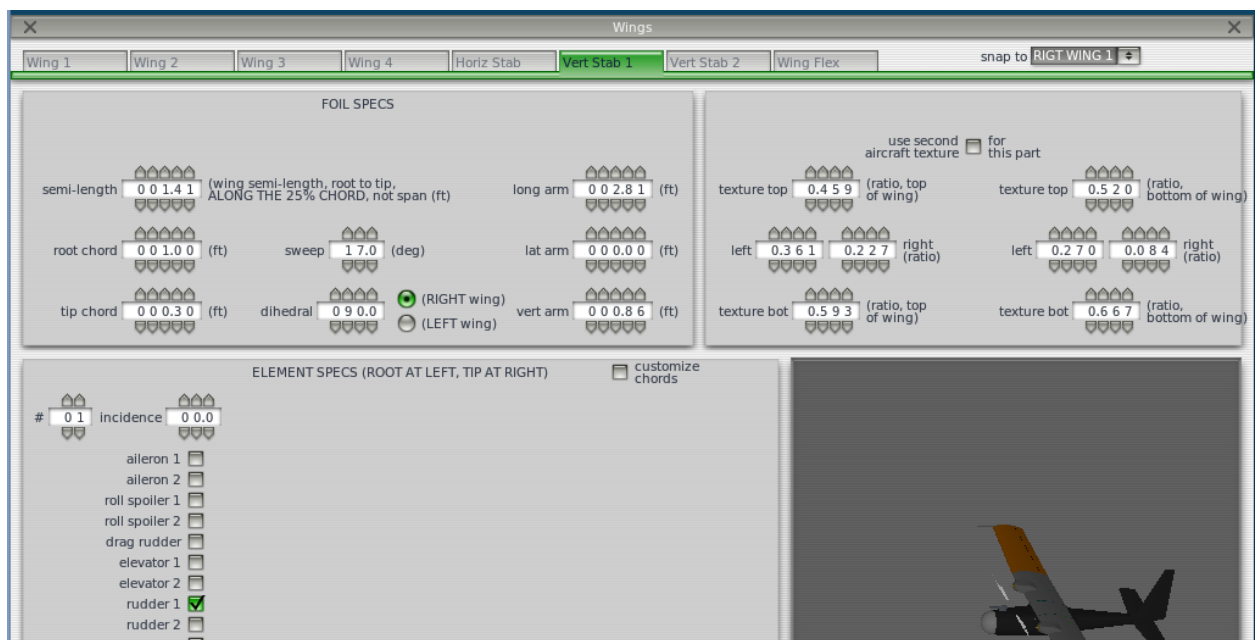


Figure 92: XPLANE vertical tail specifications

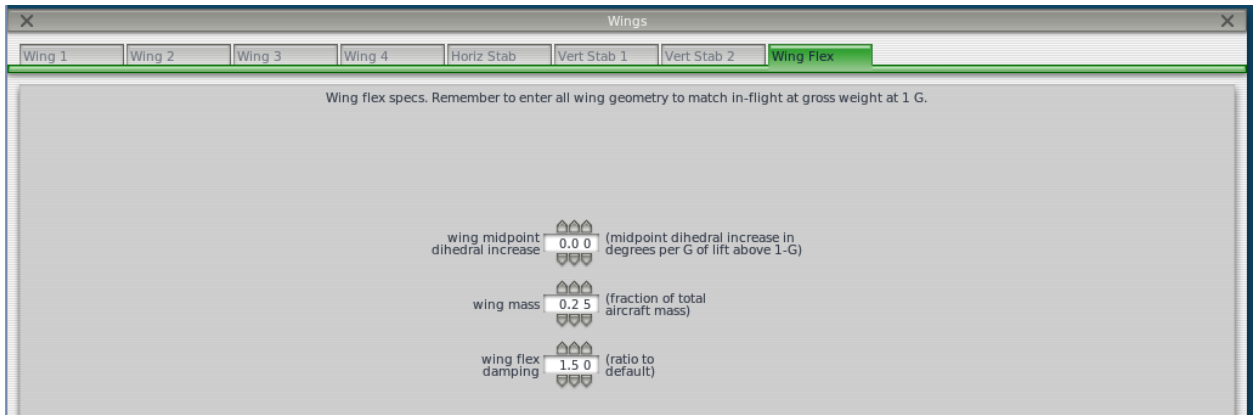


Figure 93: XPLANE wing flex parameter

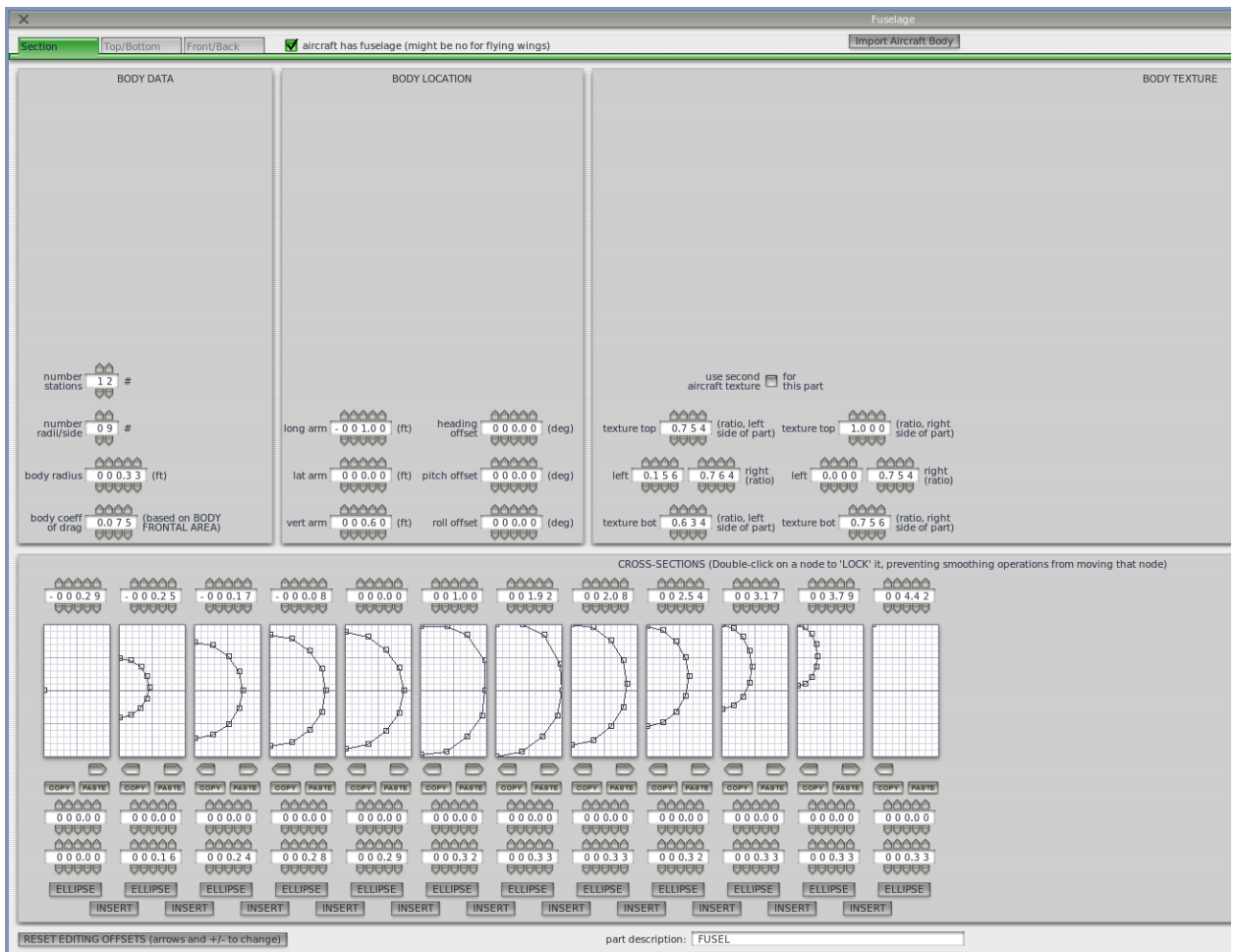


Figure 94: XPLANE fuselage details

×

Engine Nacelles

NACELLE 1

NACELLE 2

Section

Top/Bottom

Front/Back

☒ aircraft has a nacelle over this engine

Import Aircraft Body

BODY DATA

number stations

0 5 #

number radii/side

0 8 #

copy geo from part #

8

body radius

0 0 0.5 0 (ft)

body coeff of drag

0.0 7 5 (based on BODY FRONTAL AREA)

BODY LOCATION

heading offset

0 0 0.0 0 (deg)

pitch offset

0 0 0.0 0 (deg)

roll offset

0 0 0.0 0 (deg)

BODY TEXTURE

use second ☐ for this part

texture top

0.5 5 1 (ratio, left side of part)

0.5 4 4 (ratio, right side of part)

left

0.1 0 8

0.2 2 5 (ratio)

right

0.2 4 1

0.3 6 0 (ratio)

texture bot

0.4 7 0 (ratio, left side of part)

0.4 5 9 (ratio, right side of part)

CROSS-SECTIONS (Double-click on a node to 'LOCK' it, preventing smoothing operations from moving that node)

0 0 0.0 0

0 0 0.0 0

0 0 0.0 0

0 0 0.4 6

0 0 0.4 6

0 0 0.0 0

0 0 0.0 0

0 0 0.0 0

0 0 0.0 0

0 0 0.0 0

0 0 0.0 1

0 0 0.1 7

0 0 0.1 7

0 0 0.1 3

0 0 0.0 0

ELLIPSE

ELLIPSE

ELLIPSE

ELLIPSE

ELLIPSE

INSERT

INSERT

INSERT

INSERT

RESET EDITING OFFSETS (arrows and +/- to change)

part description: serpra e

Figure 95: Engine nacelle characteristics

Control Geometry

Controls

Phase-Out

Trim & Speed

Speedbrakes

Control Forces

CONTROL SIZES

aileron 1

chord ratio

0.3 0

0.3 9

1 0.0

1 0.0

control surface down then up

aileron 2

chord ratio

0.0 0

0.0 0

1 5.0

0 5.0

control surface down then up

elevator 1

chord ratio

0.1 8

0.2 2

1 5.0

1 5.0

control surface down then up

elevator 2

chord ratio

0.0 0

0.0 0

0 0.0

0 0.0

control surface down then up

rudder 1

chord ratio

0.2 6

0.5 0

2 5.0

2 5.0

control surface left then right

rudder 2

chord ratio

0.0 0

0.0 0

0 0.0

0 0.0

control surface left then right

roll spoiler 1

chord ratio

0.0 0

0.0 0

0 0.0

roll spoiler up

roll input to engage

0.0 0

(ratio)

roll spoiler 2

chord ratio

0.0 0

0.0 0

0 0.0

roll spoiler up

roll input to engage

0.0 0

(ratio)

drag rudder

chord ratio

0.0 0

0.0 0

0 0.0

drag rudder def

speedbrake 1

chord ratio

0.0 0

0.0 0

0 0.0

speedbrake FLIGHT def

0.0 0

speedbrake GROUND def

speedbrake 2

chord ratio

0.0 0

0.0 0

0 0.0

speedbrake FLIGHT def

0.0 0

speedbrake GROUND def

control surface type

smooth with gaps

FLAP SPECS

slat type

krueger flap

increase in stall angle from L.E.D. deployment

0 0

(deg)

slat type

krueger flap

increase in stall angle from L.E.D. deployment

0 0

(deg)

flap 1

plain flap

flap root chord ratio

0.2 0

flap tip chord ratio

0.2 0

flap 2

plain flap

flap root chord ratio

0.0 0

flap tip chord ratio

0.0 0

flap Cl

0.4 7 4

flap Cd

0.0 8 0

flap Cm

- 0.1 4 3

flap Cl

0.0 0 0

flap Cd

0.0 0 0

flap Cm

0.0 0 0

flaps are infinitely-adjustable between detents

flap def time

0 5.0

(sec)

flap detents

3

flap 1

0 0

0 0

0 0

0 0

flap 2

0 0

0 0

0 0

0 0

slat 1

0.0

0.0

0.0

0.0

slat 2

0.0

0.0

0.0

0.0

Plain flaps are the simplest type of flap. It is simply a control surface that pivots down, producing some extra lift and bit of drag.

Figure 96: XPLANE control geometry specifications

Weight & Balance

TABS: WEIGHT & BAL | TANKS | CG SET | CG CHECK

CENTER OF GRAVITY

long CG: (forward, default, aft limit)

vert CG: (ft)

WEIGHTS

empty weight: (lb)

fuel load: (lb)

JATO weight: (lb), from 'Special Controls' screen

jettisonable load: (lb)

maximum weight: (lb)

weight-shift weight: (lb)

displaced weight: (lb), for blimps and dirigibles

SLUNG LOAD / WATER / RETARDANT / OTHER AIRCRAFT LOCATION

RADII OF GYRATION

☐ use your own radii of gyration

WEIGHT-SHIFT

☐ jett load is SLUNG

☐ jett load is WATER

☐ jett load is FIRE-RET

☐ jett load is OTHER AIRCRAFT

Figure 97: XPLANE weight and balance information

Weight & Balance

TABS: WEIGHT & BAL | TANKS | CG SET | CG CHECK

long tank CG location: (ft)

lat tank CG location: (ft)

vert tank CG location: (ft)

fuel pump pressure: (psi)

tank #1ratio:

tank #2ratio:

tank #3ratio:

Figure 98: XPLANE fuel weight and balance

Foils

TABS: Props | Wings | Misc Wings | Misc Wings | Misc Wings | Misc Wings | Pylons 1 | Pylons 2

Prop 1

lo Re: ☐ Clark-Y (good propeller).afl

hi Re: ☐ Clark-Y (good propeller).afl

Prop 2

lo Re: ☐ Clark-Y (good propeller).afl

hi Re: ☐ Clark-Y (good propeller).afl

Figure 99: XPLANE propeller airfoils

X

Foils

X

Props

Wings

Misc Wings

Misc Wings

Misc Wings

Misc Wings

Pylons 1

Pylons 2

lo Re

☐

new42.af

hi Re

☐

new42.af

WING 1

new42.af

new42.af

variable-sweep

☐

variable-dihedral

☐

variable-incidence

☐

retractable

☐

lo Re

☐

new42.af

hi Re

☐

new42.af

WING 2

new42.af

new42.af

variable-sweep

☐

variable-dihedral

☐

variable-incidence

☐

retractable

☐

WING 3

WING 4

lo Re

☐

NACA 0012 (symmetrical).af

hi Re

☐

NACA 0012 (symmetrical).af

HSTAB

NACA 0012 (symmetrical).af

NACA 0012 (symmetrical).af

variable-sweep

☐

variable-dihedral

☐

variable-incidence

☐

retractable

☐

lo Re

☐

NACA 0012 (symmetrical).af

hi Re

☐

NACA 0012 (symmetrical).af

VSTAB 1

NACA 0012 (symmetrical).af

NACA 0012 (symmetrical).af

variable-sweep

☐

variable-dihedral

☐

variable-incidence

☐

retractable

☐

Figure 100: XPLANE wing and tail airfoils

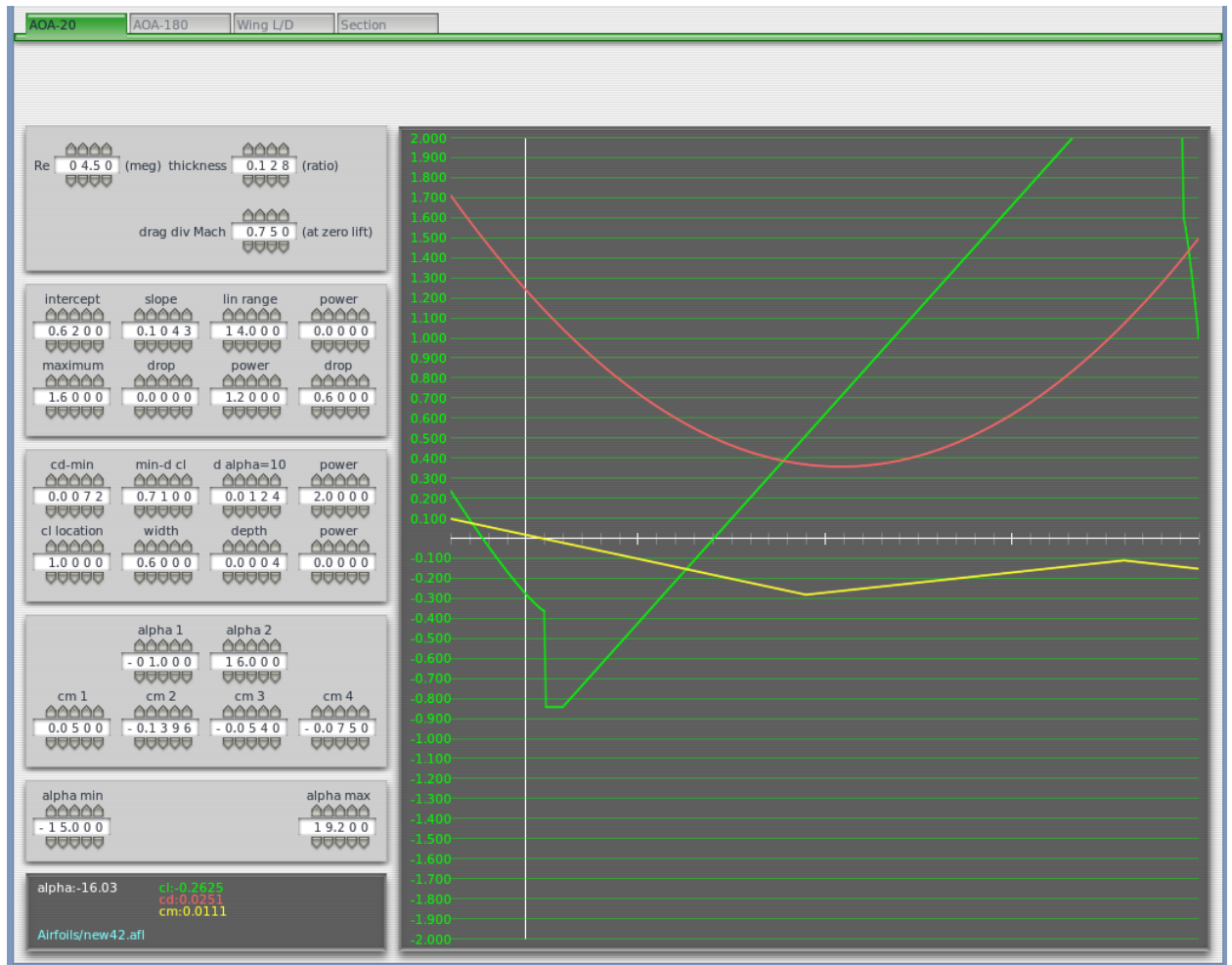


Figure 101: XPLANE Airfoil Maker, airfoil design

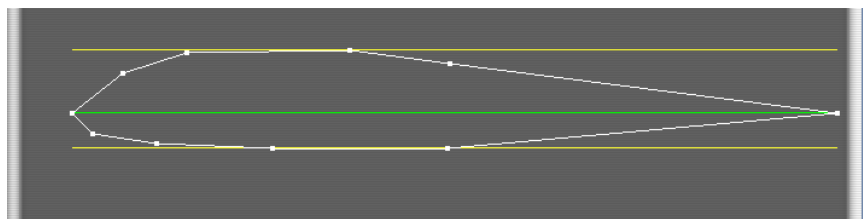


Figure 102: XPLANE Airfoil Maker, airfoil rough shape

VITA

ALYSSA SHEARON AVERY

Candidate for the Degree of

Master of Science

Thesis: DESIGN AND DEVELOPMENT OF A STORM RESEARCH UAS

Major Field: Mechanical and Aerospace Engineering

Biographical:

Education:

Completed the requirements for the Master of Science in Mechanical and Aerospace Engineering at Oklahoma State University, Stillwater, Oklahoma in May, 2015.

Completed the requirements for the Bachelor of Science in Mechanical and Aerospace Engineering at Oklahoma State University, Stillwater, Oklahoma in May, 2013.

Experience:

Professional Memberships: